8-2011

EFFECT OF ACCELERATED AGING ON MECHANICAL PROPERTIES AND STRUCTURE OF NANO-SCALE COMPOSITE SYSTEMS

David Economy
Clemson University, deconom@clemson.edu

EFFECT OF ACCELERATED AGING ON MECHANICAL PROPERTIES AND STRUCTURE OF NANO-SCALE COMPOSITE SYSTEMS

A Thesis
Presented to
the Graduate School of
Clemson University

In Partial Fulfillment
of the Requirements for the Degree
Master of Science
Materials Science and Engineering

By
David Ross Economy
August 2011

Accepted by:
Dr. M. Kennedy, Committee Chair
Dr. J. Ballato
Dr. J. Luo

ABSTRACT

Nano-scale composites are being investigated by academic, industrial, and national laboratories for potential applications such as wear resistant coatings and high strength foils. These structures are of interest due to their as-fabricated mechanical properties, such as high strength for nanolaminates. However, there have only been limited studies of the long-term mechanical stability. A greater understanding of how these systems might respond to sustained use is needed before these systems transition from research laboratories into widespread application. It is the objective of this thesis to clarify the link between accelerated aging using elevated temperatures over time and mechanical properties of two distinct types of nano-scale composite systems: metallic nanolaminates and polyimide matrix nanocomposites.

Metallic nanolaminates are composites with alternating laminar metallic films whose individual layer thicknesses range from 2 nm to 100 nm. As the individual layer thicknesses decrease, the hardness of the nanolaminate system exceeds predictions from both conventional composite theories as well as the traditional Hall-Petch relation. This study examined how these nanolaminates responded to accelerated aging (elevated temperatures in three different atmospheres) by characterizing the mechanical response. Two different systems were studied, Cu/Nb, a FCC/BCC system studied by other groups, and Ti/W, a HCP/BCC system that has not been previously studied. Nanolaminate systems produced for this study had a total thickness of 1000 nm with individual layer thicknesses of 20 nm or 100 nm. After deposition, the film systems were heated to 400°C for 30 minutes under lab air, high purity argon, or a 98%Ar/2%O_2 blend. Accelerated aging of the Cu/Nb layers

caused significant softening in the 20nm layer thickness samples (5.5 to 1.3 GPa for 20 nm Cu/Nb aged in Ar). Contrastingly, softening was not observed in 100 nm layer thickness samples (4.3 to 4.8 GPa for 100 nm Cu/Nb aged in Ar). This same trend was also followed by the other Cu/Nb samples and all the Ti/W systems regardless of aging atmosphere. Comparison with other studies show that residual stress may influence the severity of the film aging. It was concluded that for both systems oxidation is not the main concern for softening induced by accelerated aging.

The second type of nano-scaled composite system examined was polyimide matrix nanocomposites. NASA is exploring these systems for high-temperature aerospace applications, such as the matrix material for jet engine casings. This work looks at the mechanical aging of polyimide PMR-15, which is currently in use, and RTM-370, a possible replacement to PMR-15. In addition, this study looks at how the aging behavior is affected by the inclusion of three distinct nanoparticle filler materials: carbon nanofiber, synthetic clay, and organically modified natural clay. The elastic modulus of the polyimide nanocomposites were measured before and after accelerated aging. It was seen that the PMR-15 samples were susceptible to surface oxidation and stiffening due to the molding procedure (5.7 to 6.7 GPa for the edge region of neat PMR-15). Similar results were not found for the RTM-370 samples, as stiffness remained consistent regardless of indentation location. Nanoparticle addition to the polyimides yielded varying results. It is hypothesized that this disparity is due to the difference in particle surface area between nanoparticle fillers. Although the incorporation of nanoparticles was done in order to boost oxidation resistance in these systems, this was not observed in this study.

DEDICATION

For all those who dedicate their lives to learning.

"Learning never exhausts the mind"

-Leonardo da Vinci

ACKNOWLEDGMENTS

First and foremost, I must give thanks to God above all others. For without the Lord, what is there? Forever unchanging and always inspiring, I cannot begin to describe the debt I owe to Him. God is a constant source of direction, strength, and above all, patience.

Secondly, I would like to thank my wife Jess. You have had more patience for me than anyone I have ever met. The daily devotion that you show me is staggering, and for that I am truly thankful for you.

I cannot begin to thank my parents; my mother and father have and continue to support me in all my efforts. I could not begin to ask for more from them. I love you both and I could not have made it this far without the two of you. Also, I would like to thank my brother, Michael. During my time at Clemson, you have always been there to listen to my ideas as well as my complaints.

My advisor, Dr. M. Kennedy, has been a constant source of both encouragement and challenges. Thank you for your support, guidance, and above all, patience. I am appreciative of my graduate committee members, Dr. J. Ballato and Dr. J. Luo, for the gift of their time and suggestions. Thanks go to my research group members, J. Reid, N. Mitchell, and G. Chen, who have all provided advice and pointed out my shortcomings. In addition to the graduate students in my research group, I would like to give special thanks to three undergraduate students whose research projects focused on sputtering spurred on my understanding. They are J. Haley, R. Need, and P. Windsor and were more help than they knew.

Thanks also go to Dr. S. Miller at NASA Glenn Research Center who helped me with all of the nanocomposites work. Your knowledge and insight are greatly appreciated. In addition, I would like to thank Dr. J. Hudson, Dr. T. Darroudi, and the rest of the staff at Clemson's EM facility for their advice and help with the electron microscopy work. Also I must thank, Dr. J. Harriss for consultation and profilometry training, as well as Mr. L. Kuhn of Hysitron™ Inc. for his discussions about nanoindentation,

Lastly, I would like to thank the National Aeronautics and Space Administration for the financial support under award number NNX10AM76H.

TABLE OF CONTENTS

Page

TABLE OF CONTENTS (Continued)

Page

TABLE OF CONTENTS (Continued)

Page

TABLE OF CONTENTS (Continued)

Page

TABLE OF CONTENTS (Continued)

Page

LIST OF FIGURES

Figure Page

LIST OF FIGURES (Continued)

Figure Page

LIST OF FIGURES (Continued)

Figure Page

LIST OF TABLES

CHAPTER ONE

INTRODUCTION TO NANO-COMPOSITES

Composite systems are those that are made up of two or more materials that differ in physical or chemical properties[1.1]. Typically synthetic composites are created to elevate a set of materials properties, such as electrical conductivity or mechanical stiffness. Composite systems can occur naturally, such as tempered martensite, but are generally synthetic, such as fiber reinforced epoxy. Nanocomposites are a class of composites, which contain a component that has at least one dimension on the order of nanometers. Many nanocomposites are created to enhance various aspects of a system such as its strength[1.1], weight[1.2], or thermal stability[1.3,1.4] by incorporating nano-sized components.

Although many nanocomposites are created that are able to achieve the increase in properties when fabricated, the long-term effects are not always characterized or understood. Over the course of a material's usage life it may undergo changes due to duration of use, this is aging[1.5]. For the purposes of this thesis, accelerated aging, is utilizing the application of heat to elevate diffusion and reaction kinetics in order to observe aging under reduced time constraints.

In order to accurately predict how composites will function over long periods of time, it is important to model the aging experimentally and characterize changes in the material's properties and structure during the aging process. The two systems examined in this study are metallic nanolaminates and polyimide resin nanocomposites. Since each of these systems has different applications, they also will have different expected lifetimes and aging processes.

1.1. Background

Reducing a material's dimensions into the nano-scale such as particle size, grain size, or layer thickness may often impart behaviors, such as higher strength, purely due to restrictions imposed by the sizes involved[1.1-3,1.6,1.7]. The reduced size-scale in composites also results in shorter diffusion pathways. If diffusion impacts the strength of the system, as is the case for the cause of strengthening in nanolaminates, the strength could be impacted by aging[1.8]. Thus, understanding the implications of aging on the strength of such nanocomposite materials is necessary. The following sections will briefly introduce the two types of nanocomposites studied in this work and outline major aging factors.

1.1.1. Metallic Nanolaminates and Aging of These Systems

Nanolaminate systems are laminar multilayered structures with individual layer thicknesses of 100nm or less. An example of a Ti/W nanolaminate is shown in Figure 1.1. Each interface between layers restricts dislocation motion and the high number of these interfaces in nanolaminates result in higher hardness when compared to single component films. The mechanical properties of as-deposited nanolaminates have been examined in depth[1.1,1.9-11].

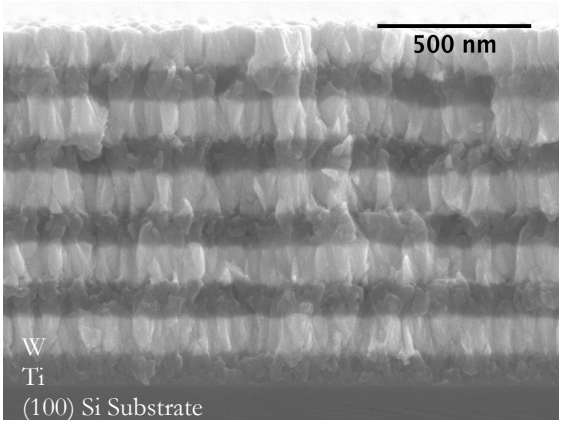

Figure 1.1: Cross-section of a 100nm Ti/W nanolaminate system. This image shows the layered geometry, and individual Ti & W layers, starting with the Ti layer first.

Recent work using FCC/FCC and FCC/BCC model systems has shown that these nanolaminates display unique properties due to surface and interfacial effects[1.1]. In bulk materials, interfaces compose only a small

fraction of the total volume. However, nanolaminates contain a very high density of dissimilar interfaces, thus interfacial effects play a much larger role in their properties.

Only a limited number of studies on microstructural evolution of nanolaminate systems during aging have been conducted[1.8,1.12-15]. Even fewer studies exist that examine the mechanical response of aged nanolaminate systems[1.8,1.12]. Reports in the literature have identified two distinct problems in high temperature mechanical durability of nanolaminate systems: oxidation[1.12] and stability of interfaces[1.8]. When nanolaminates of Mo/Pt were heated in air, substantial oxidation was observed, and it contributed to significant softening in all ranges of layer thicknesses tested[1.12]. However, when Cu/Nb nanolaminates were heated under vacuum after the films had been peeled from the substrates, softening was only observed in thinner layer thicknesses at higher temperatures[1.8]. It was suggested that this was due to the stability of the layered structure at larger thicknesses, which does not exist when the size scales are further reduced[1.8]. These two studies present two different mechanisms for mechanical durability during aging of metallic nanolaminates. Because of their distinct results they are not enough to gain a full understanding of the evolution of mechanical properties of metallic nanolaminates when subjected to high temperature environments[1.8,1.12].

1.1.2. Polyimide Nanocomposites and Aging of These Systems

Polyimide nanocomposites are matrix-filler type composites, which utilize a polyimide matrix and contain nanoparticles as the filler material. Many research groups have incorporated nano-scaled filler materials into polymer matrices to alter the physical properties, mechanical behavior, and fracture toughness of the resulting composites[1.6,1.7,1.16-21]. The end result depends both on the polymer matrix, which can range from soft thermoplastics to stiff thermoset polymers, as well as the filler material, which can range in

composition, shape, and scale. Articles have highlighted the importance of some filler properties on the nanocomposite mechanical response including filler size[1.18,1.19], surface area[1.6,1.7], surface interaction[1.16-18,1.21], and spacing of the particles[1.18-20].

Polymer nanocomposites have been investigated for structural applications in aircraft and space systems due to their relatively high mechanical properties and low density. However, many of the polyimides identified for use also show indications of thermo-oxidation, which can limit the polymer component reliability[1.22]. This oxidative aging results in a reduction in molecular weight due to chemical bond breakage, out-gassing of low molecular weight gaseous species and chain scission. Researchers have previously shown that PMR-15, a polyimide currently used for jet turbine applications, is susceptible to oxidation and forms a surface oxide layer when aged[1.22].

The aging of polyimide nanocomposites can be complex because the filler can serve a dual purpose-as both a strengthening agent and also an oxidation inhibitor[1.2-4]. These fillers (clay nanoparticles and carbon nanofibers) have been added to decrease impact of the oxidation on the mechanical properties. Fillers have been shown to change the mechanical response, but also the thermo-oxidation of the matrix material[1.2-4]. Two potential mechanisms of improvement described in this work include (1) increased strength of the oxidation layer leading to reduced microcracking, and (2) improved the dimensional stability of the resin, thereby reducing the material shrinkage and resultant cracking.

This work will look at how the aging of PMR-15 compares the aging of an emerging polyimide, RTM-370[1.23], and nanocomposites with an either as a matrix. RTM-370 is an attractive material due to decreased health hazards of its precursor materials and elimination

of solvents. It is the goal of this project to monitor thermal oxidative aging behavior of PMR-15 and RTM-370 polyimide.

The use of new nano-structured polymeric materials appears to be promising based on initial research findings. However, their real-world applications require that a greater understanding of their long-term mechanical and structural durability be established. The application of small scale testing methods such as nanoindentation can provide valuable steps toward understanding the local changes that underlie the overarching behaviors.

1.2. Research Intent

For most composite systems, enhanced properties of the entire component are desired. However, in order to understand how to obtain those properties, local measurement of comparable properties can be used to probe the underlying mechanisms. This study will use local testing methods for both composite systems being examined: nanolaminate metallic films and polyimide resin nanocomposites. The research outlined here seeks to do this using small-scale testing methods such as nanoindentation to explore the potential mechanisms for changes that occur during aging in nano-scaled composite systems.

(I) The effect of accelerated aging on structure and hardness of nanolaminate film systems

Nanolaminate film systems have been the subject of many recent research studies[1.12,1.24-27]. They are of interest due to their deviation from conventional composite behavior with respect to characteristic length[1.1,1.9-11]. By maintaining the same volume fraction of components it is possible to directly control the obtained hardness by varying individual layer thickness. However, some studies have highlighted a sensitivity to aging[1.8,1.12]. These studies though, are not in direct agreement[1.8,1.12], and it is desired to

examine the discrepancies, in order to form a unified understanding of the aging behavior of nanolaminate films.

(II) Nanocomposite filler influence on mechanical properties and surface degradation of polyimides used for NASA applications

The utilization of lightweight, high-strength polyimide matrix composites is of interest for NASA. They have the potential to replace metal components with fiber-reinforced composites for significant weight reduction. However, their high temperature aging behavior is not yet adequate for use[1.22]. Research has shown that the incorporation of nanoparticles can potentially increase the thermal oxidation stability of polyimide resins such as PMR-15[1.2-4]. The application of nanoindentation was used to locally investigate the effects of aging on polyimide matrix nanocomposites.

CHAPTER TWO

COMMON TECHNIQUES FOR CHARACTERIZING THE MECHANICAL PROPERTIES AND STRUCTURE OF NANO-SCALE COMPOSITE SYSTEMS

2.1. Introduction

The mechanical properties of composites depend on the following aspects: volume fraction of each component, filler arrangement, chemistry of the matrix and filler phases, as well as the interface between those phases[2.1]. The interaction of these components is not fully understood as discussed in Chapter One.

As previously described, this work focuses on two types of nano-scaled composites – layered as well as traditional matrix/filler composites. Bulk testing methods have been utilized elsewhere, such as tensile testing[2.2,2.3] and impact testing[2.4,2.5] for polymer nanocomposites. These results did yield some useful data, however, when coupled with small-scale testing methods it allows for a comprehensive understanding of both the bulk properties as well as the localized behavior. It is important that the interpretation of the mechanical testing be observant of the relevant sizes and the overall structure of the systems being tested. This chapter will review the common test techniques that have been useful in the characterization of nanocomposite systems. These techniques include nanoindentation, scanning electron microscopy (SEM), x-ray diffraction (XRD), and surface profilometry. Other testing methods are available but nanoindentation, SEM and XRD are all specifically important for nano-scale composite systems because of their ability to locally observe properties of dissimilar systems.

2.2. Quasi-Static Nanoindentation

Nanoindentation, or depth-sensing indentation, was a technique developed in the 1970's to measure the hardness of small volumes[2.6,2.7]. In nanoindentation, a probe with a known geometry and area are used to apply force to a material, the resulting load and displacement are directly measured during indentation. This technique is similar to traditional indentation where an indenter applies a known load to a sample and measures the resulting plastic deformation. In nanoindentation however, the load and displacement measurements allow for the calculation of stiffness and elastic modulus, which is not possible through traditional hardness testing. Additionally, the length and force scales are considerably reduced. Typical nanoindentation tests utilize indentation depths that are less than one micrometer and peak loads that are often less than 10,000 micronewtons (0.01N).

Nanoindentation is of interest in nano-scale composite systems due to the precision of depth control that can be used. In multilayer systems, effects of the substrate need to be accounted for, which will be further discussed in Section 2.2.1. Similarly, in polymer nanocomposite systems the decreased testing volume allows specific regions to be accurately tested, which will be discussed in Chapter Four.

There are multiple types of nanoindentation systems, which use different methods for actuation such as electromagnetic and electrostatic forces[2.7]. The systems produced by Agilent Technologies™ Inc. utilize electromagnetic force and the systems produced by Hysitron™ Inc. utilize electrostatic force[2.7]. In this study a Hysitron™ Triboscope nanoindentation transducer was utilized, which features a triple plate capacitor/transducer design, seen in Figure 2.1. The Hysitron™ Triboscope system utilizes a Digital Instruments™ Multimode AFM piezoelectric base for sample motion.

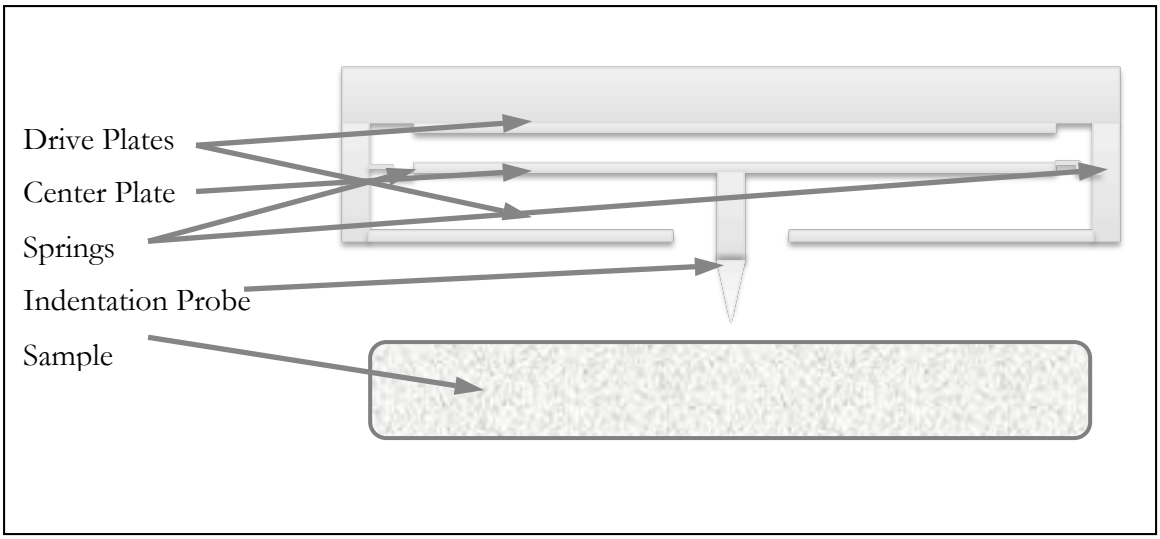

Figure 2.1: A schematic of a Hysitron™ nanoindentation transducer. The Hysitron™ system utilizes a triple plate capacitor design to actuate and measure simultaneously.

Through the course of a typical single, static loading nanoindentation test, the probe is loaded into the sample, held, and then retracted[2.7]. During that period, both load and displacement measurements are being simultaneously recorded. The system may either be load controlled, where a set maximum load is identified, or depth controlled, where a set displacement is applied. Load controlled indentations are most common, but displacement controlled indentation is useful in testing thin films to better observe motion of dislocations[2.7]. A representative load versus displacement plot from one nanoindentation test is shown in Figure 2.2 with A) loading, B) hold and C) initial unload[2.7]. With significant displacement, both elastic and plastic deformation occurs during the loading portion. However, on the initial unloading, only elastic deformation is recovered, thus the initial slope of the unloading curve is used to measure stiffness. The holding step at the maximum load allows for the compensation of creep or other time dependent processes.

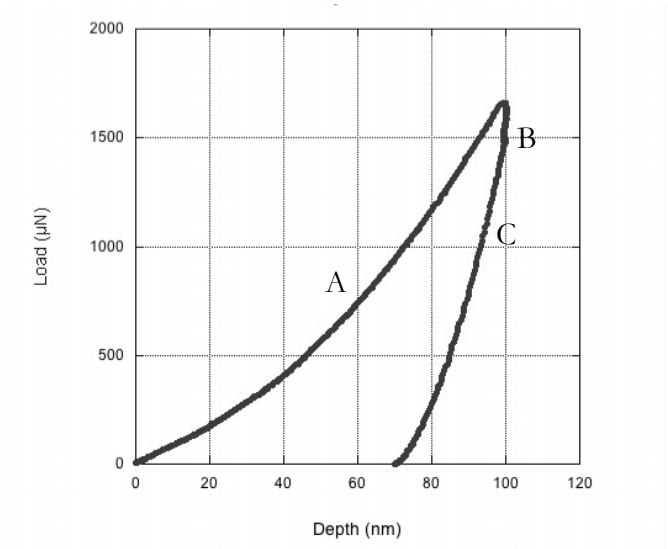

Figure 2.2: A typical plot of load versus displacement from a displacement controlled nanoindentation test. This indentation contains a loading portion (A), the short vertical segment at the top is creep (B), and an unloading portion (C). The amount of plastic deformation can be seen as the change in displacement between the loading and unloading portions at zero load.

The hardness and elastic moduli can be calculated from the initial unloading of a nanoindentation test. One of the most common methods was modeled by Oliver and Pharr[2.6]. Assuming a homogenous material, known geometry of the nanoindentation probe and purely elastic deformation upon initial unloading, the Hardness can be calculated by:

$$H = \frac{P_{\max}}{A} \tag{2.1}$$

where H is the hardness, $P_{\max}$ is the maximum load, and A is the contact area of the indentation probe[2.6,2.7]. In addition to the hardness, the Young's modulus (E) is calculated as well. The reduced modulus, takes into account the compliance of the indentation probe:

$$E_r = \frac{\sqrt{\pi} S}{2\beta\sqrt{A}} \tag{2.2}$$

where S is the measured contact stiffness, A is again the contact area, and β is a geometric constant dependent on the shape of the indenter[2.7]. A typical nanoindenter geometry is the Berkovich indenter, a 3-sided pyramid with a face angle of 65.27° [2.7] and which has a beta of 1.034. A table of beta factors for common indentation geometries is well-documented elsewhere[2.7]. The reduced modulus is calculated from the elastic modulus and Poisson's ratio of both the sample and indenter:

$$\frac{1}{E_r} = \frac{(1-\nu^2)}{E} + \frac{(1-\nu_i^2)}{E_i} \tag{2.3}$$

where E_r is the reduced modulus, E and ν are the modulus and Poisson's ratio of the sample respectively, and E_i and ν_i apply to the properties of the material from which the indenter is made[2.6.2.7]. Nanoindentation probes are primarily made from diamond (E: 1141 GPa, ν: 0.07)[2.7], so that the yield in the sample will be greater than the yield of the tip.

2.2.1.Calibration of Tip Shape

This analysis is dependent on precise calibration of the contact area of the nanoindentation probe with respect to indentation depth. Calibration is performed by indenting a range of depths and maximum loads on a standard calibration sample at similar depths to the depth to be used for nanoindentation testing. Following testing, the data is then fit with the hardness equation using the known values to determine a function of the contact area as a function of indentation depth.

For this study the chosen reference material was single crystal fused quartz, which is known to have an elastic modulus of 72.5 GPa and a reduced modulus of 69.6 GPa when measured with a diamond indentation probe, but other standards are available such as single

crystal aluminum and sapphire. Calibration results showing satisfactory calibration on fused quartz are included in Figure 2.3.

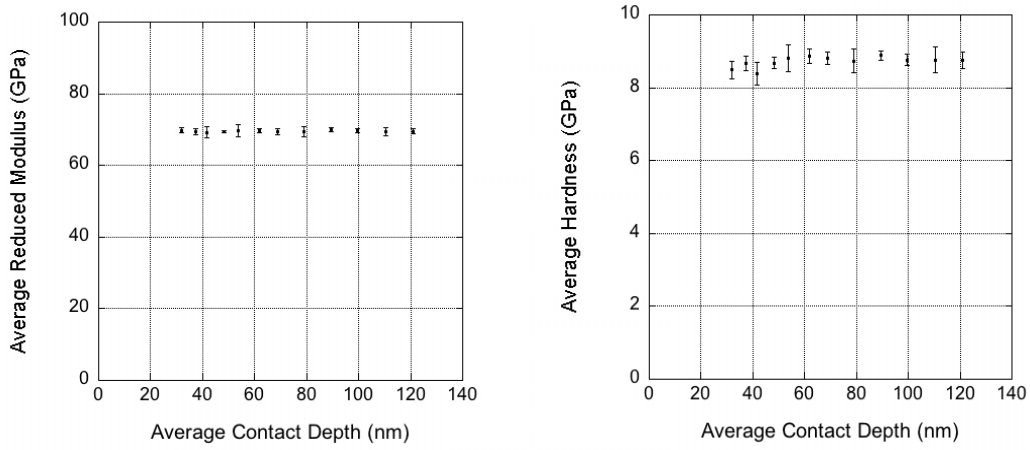

Figure 2.3: Reduced modulus (left) and hardness (right) of fused quartz calibration standard from nanoindentation testing showing ideal values. Data displayed has been averaged from multiple indentations.

2.2.2.Sensitivity of the Nanoindentation Testing Technique

Many groups have worked to improve the accuracy of the Oliver-Pharr analysis method[2.8,2.9]. This can be done by decreasing experimental error or making changes to the calculations suggested by Oliver and Pharr[2.9]. The Oliver-Pharr model is based on ideal, homogenous systems and thus can lead to errors when complex samples such as polymers or thin films on substrates are tested[2.7]. Oliver-Pharr assumed a homogenous system without considering the effects of boundaries, substrates, and other geometric considerations[2.8,2.9].

When film thickness decreases it is common to encounter measurement problems, primarily substrate effects[2.8,2.9]. It is generally accepted that to avoid substrate effects when testing a thin film using nanoindentation, the indents should not penetrate deeper than 10%

of the film's total thickness[2.7,2.8]. If this is not observed, the results from testing are likely to be strongly influenced by the mechanical properties of the substrate and not the film. This is due to the volume of material undergoing plastic deformation below the nanoindentation probe[2.7]. Plastic deformation is not limited to only the depths reached by the nanoindentation probe, but continues in the region below the indenter as well[2.7]. Thus, a nanoindentation test will yield results from depths that exceed the maximum indentation depth. The size of zone of plastic deformation can be estimated by a relation considering the contact depth and radius of the indentation probe[2.10]. For fully plastic indents the ratio of the size of plastic zone to the indent size (c/a) is equal to 2.5 for indents undergoing elastic deformation as well $c/a \approx 4$[2.10].

The literature on substrate effects in nanoindentation only studied single-component, single-phase films on substrates[2.8,2.9]. However, it is expected that any substrate effects seen in a single component film would be seen in multilayer films containing similar components. When testing multilayered thin films it thus becomes important to produce a sample with substantial thickness so that it is possible to indent deep enough into the film in order to test the entire laminate system. It is still necessary to not indent so deep as to encounter effects from the underlying substrate.

Also, sources of error in nanoindentation results, such as thermal drift and vibration, make it difficult to calibrate and measure shallow indents ($<\approx$30-40 nm). The issues of experimental error and substrate influence may overlap in thinner films. This makes the extraction of valid results unlikely from films thinner than 400nm using traditional Oliver-Pharr analysis.

2.3. Scanning Electron Microscopy

Scanning electron microscopy (SEM) is an imaging technique that utilizes a highly focused electron beam to create high-resolution image of a surface. This is done by bombarding the sample with a highly focused electron beam and monitoring the electrons emitted as a result. In the detector, the emitted electrons create an output signal, which is then converted to usable data by a computer. Images are composites of individual points as the beam is rastered across the surface. The maximum resolution of an optical microscope is limited by the wavelength of visible light, hundreds of nanometers. Electron microscopes can produce electron beams with wavelengths less than 0.1nm[2.11]. This resolution enables electron microscopes to appropriately observe the structure of nano-scale composite systems.

Typically, SEM images are created by monitoring secondary electron emission from a sample surface when bombarded with electrons generated by the microscope[2.11]. The electrons generated by the microscope are called the primary electron beam, which are finely focused and adjusted by electromagnetic lenses in the column of the microscope as shown in Figure 2.4. An image is created by scanning the surface of interest in a raster-like fashion to detect the secondary electrons emitted with respect to position along the sample.

Many different types of information can be obtained from a sample using SEM analysis. Most commonly SEMs are used to generate surface topography images based on secondary electron emission. However, they can also be used for compositional images by detecting electrons that have been backscattered from the primary electron beam, known as backscatter electrons. Backscattered electrons can also be used to show differences in grain orientation as well as diffraction patterns based on electron backscatter diffraction (EBSD).

For the purposes of this work, SEM techniques to generate topography will be the only techniques to be discussed at length.

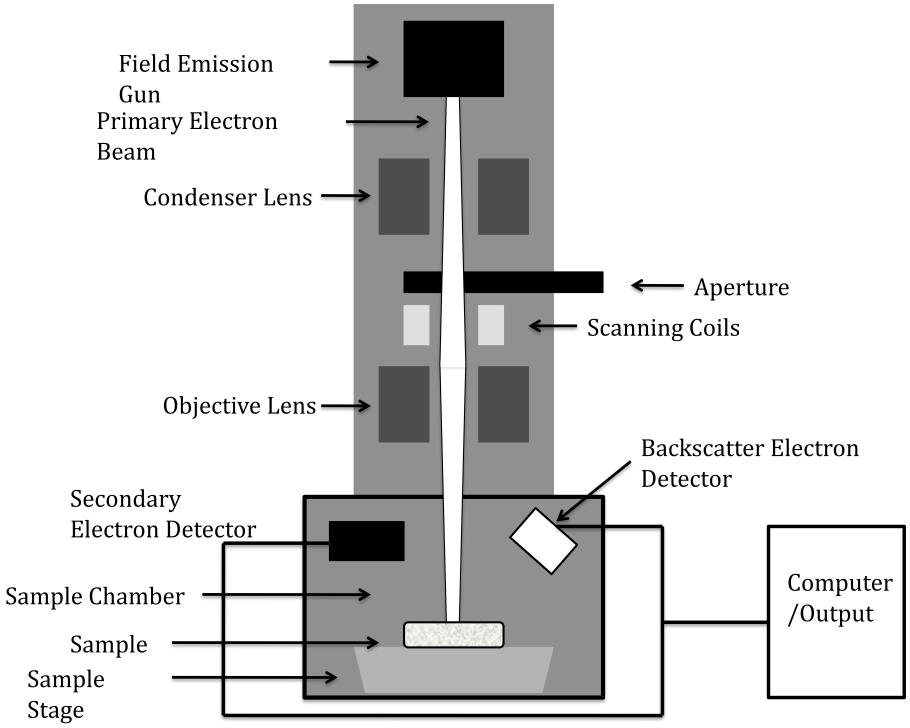

Figure 2.4: A schematic of the basic parts in a typical scanning electron microscope[2.11]. The electron beam is generated at the top of the column, which is then focused by multiple apertures. Scanning of the surface is accomplished by a set of electromagnets. Finally, interactions with the sample are primarily monitored by the secondary electron detector. Also, the backscattered electron detectors and other analysis equipment can provide further information about the sample being observed.

There are multiple types of SEMs, one of which is a field emission SEM (FESEM). The main difference between conventional SEM and FESEM is that a field emission gun produces the electron beam in FESEM. A field emission gun when compared with a conventional thermionic emission triode gun produces a much smaller, brighter, more coherent beam of electrons[2.11]. The stronger, smaller electron beam results in the ability to obtain higher resolution as seen in Figure 2.5 and the figures included in Chapter Three.

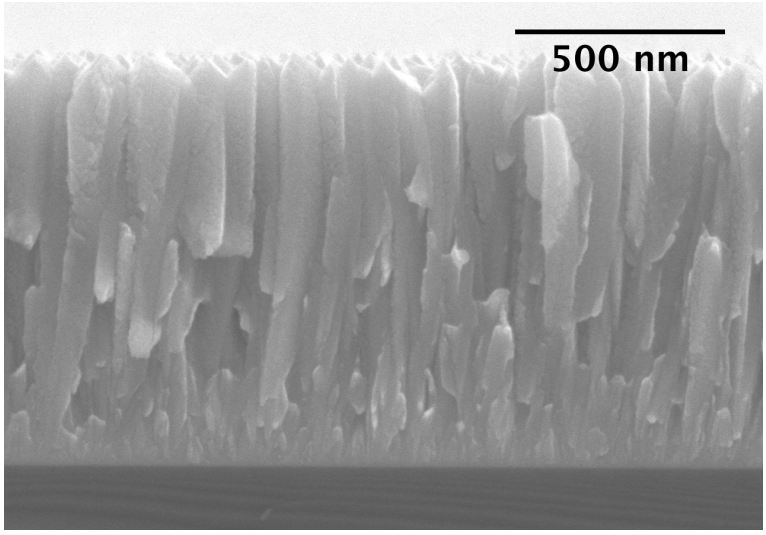

Figure 2.5: SEM image of 1000nm thick Nb film deposited on (100) Si showing cleavage surface. This type of cross-section view allows the layered profile of a nanolaminate sample to be observed.

2.3.1. Sample Preparation Concerns

When the primary electron beam encounters the sample, a significant charge builds up at the beam site. If the surface of the sample is non-conductive, excess charge can build up at the observation area, which is known as charging. That residual charge will cause the primarily electron beam to be repelled from the normal path[2.11]. As such, conductive samples are desired for electron conduction away from the observation area. The samples being studied under SEM are to be metallic films deposited onto silicon substrates. To avoid charging, the metal films were electronically grounded to the sample platen upon insertion into the microscope.

2.4. X-Ray Diffraction

X-Ray Diffraction (XRD) is a testing method that is used primarily to determine crystal structure and atomic spacing of crystalline materials based on interactions with x-rays. In addition to structure and atomic spacing of single crystals, XRD can be used for a variety of applications such as crystalline orientation, residual stress, and formation of intermediary phases[2.12]. Typically XRD is performed on crystalline powders but can also be applied to a range of materials such as glass, metal, and more importantly for this work, thin films[2.12]. XRD allows the analysis of individual diffraction peaks that may correspond to a singular component in a system, which is ideal for nano-composite systems.

Central to XRD, is a relation known as Bragg's law, which relates the atomic spacing of a crystal, d, and the angle of X-ray incidence, θ, to the wavelength of X-rays being generated, λ, as follows:

$$n\lambda = 2d\sin\theta \tag{2.4}$$

Bragg's law is important because it describes the relationship that is necessary for X-ray interference with atoms to be constructive as shown in Figure 2.6. That is, when X-rays encounter a material and are diffracted, they will either remain in phase, and interfere destructively with one another, or become out of phase, and destructively interfere with one another also shown in Figure 2.6.

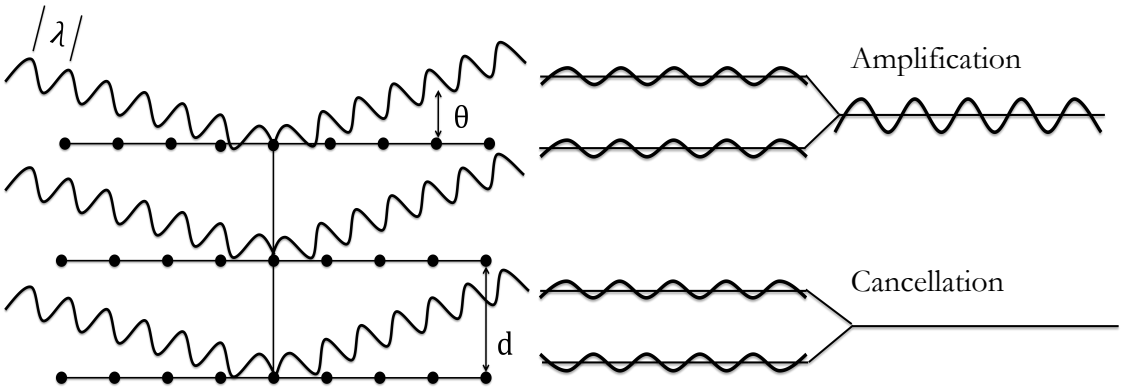

Figure 2.6: A schematic of X-ray interactions with atoms in a crystal lattice (Left). A schematic diagram showing in phase, constructive X-ray interference (Right top), and out of phase, destructive X-ray interference (Right bottom)[2.13].

XRD is performed by bombarding a sample with x-rays at a range of different θ values and measuring the resulting diffracted x-ray intensity. Large intensity peaks indicate that a crystal orientation exists with corresponding lattice spacing from Bragg's law. Typical systems utilize a copper Kα X-ray source, which has a characteristic wavelength of 1.54Å[2.12]. In addition to identifying materials and crystal orientation, XRD is useful in multilayer systems to identify overall grain texturing as well as showing disturbances in lattice spacing. This could include strain due to residual stress as well as strain due to interdiffusion and possible intermetallic phase formation. Disturbances in lattice spacing will manifest in XRD as a broadening of a diffraction peak, so the peak is no long a sharp peak at one θ value.

As mentioned earlier, XRD allows the analysis of individual peaks, this is important in multi-component systems which contain multiple peaks with each component corresponding to different peaks. Each crystal structure has an ideal diffraction pattern and by matching peaks in collected data to the ideal pattern allows for identification of phases and orientations.

2.5. Surface Profilometry

Surface profilometry measures the topography of a surface. Topography measurements allow for the direct measurement of specific surface features, calculation of surface roughness, and most importantly for their application to multilayer thin films, calculation of residual stress. This is done through assumptions about the film's substrate and changes in curvature before and after film deposition. Residual stress calculations are further described in Section 2.5.1.

There are two types of profilometers, which utilize either contact or non-contact measurement methods. For this study, a diamond-tipped stylus profilometer is used to make contact profile measurements. A diamond-tipped stylus profilometer such as the Veeco™ Dektak[3] functions by taking electromechanical measurements while moving the sample beneath a stationary tip. Any changes in vertical deflection of the sample surface are transferred to the stylus tip, which is mechanically coupled to a linear variable differential transformer (LVDT), which converts linear displacement into an electrical signal[2.14]. The output signal is amplified and converted by computer into a useable test result in the form of height displacement as a function position along the scanned length[2.14].

Profilometers generally allow specification of load applied to the stylus tip as well as scan length, measurement resolution and scan speed[2.14]. Following scanning, the software uses a curve-fit regression analysis to calculate radius of curvature which can be used to estimate residual stress of thin films using Stoney's equation, which will be further detailed in Section 2.5.1[2.15].

2.5.1. Substrate Curvature and Residual Stress Calculations for Thin Films

A common method that is used for calculating the residual stress of a thin film is known as the substrate curvature method[2.16,2.17]. This method uses changes in substrate curvature to estimate the residual stress of the deposited film. Substrate curvature is measured using a profilometer or another similar method both before and after film deposition to measure the overall change in curvature of the substrate. The residual stress in the film can then be calculated using Stoney's equation[2.14-19], which was first proposed in 1909[2.15]:

$$F/w = \sigma_f t_f = \frac{M_s t_s^2}{6}\left(\frac{1}{R_{final}} - \frac{1}{R_{ini}}\right) \tag{2.5}$$

Knowing the Young's modulus of the substrate, M_s, thickness of the substrate, t_s, the curvature change, Δk, and assuming that the thin film's contribution is negligible, the stress of the film can be thus calculated. Stoney's equation also relates the in-plane force (F/w) to the biaxial film stress, σ_f, and the film thickness, t_f. For this study, the biaxial modulus of (100) silicon is assumed to be 172 GPa[2.8]. Using Stoney's equation assumes that the thickness of the film and substrate is constant, linear elastic behavior, homogeneous and isotropic systems, with the stress localized in the film[2.15]. Due to these assumptions, Stoney's equation is only used as an approximation of the residual stress.

CHAPTER THREE

THE EFFECT OF ACCELERATED AGING ON STRUCTURE AND HARDNESS OF NANOLAMINATE FILM SYSTEMS

3.1. Introduction to Nanolaminates

Nanolaminate thin film systems are a type of composite where nano-scale films are deposited in an alternating laminar orientation to form a larger scale layered system (Figure 1.1). Interest in these systems has risen due to the mechanical strengthening observed as the individual layer thickness decreases[3.1-14]. A system made of two "soft" metals may yield a multilayer system with a yield strength not thought possible based on bulk yield strength values[3.1]. Nanolaminate systems have received attention in recent years for use in microelectromechanical systems (MEMS), freestanding high-strength foils, and wear-resistant coatings[3.1]. These applications make use of these structures' high strength and resistance to dislocation flow.

Hall-Petch type strengthening has been observed for nanolaminate systems with layer thicknesses on the order of one micrometer, which has been attributed to formation of dislocation pile-ups[3.12,3.18-20]. However, when layer thickness is decreased into the nano-scale, deviations from the model have been observed[3.1,3.3,3.19,3.21,3.22]. It has been proposed that when the layer thickness is reduced below ≈75nm, deformation of the system involves slip of single dislocations confined to individual layers as can be seen in Figure 3.1[3.3]. This behavior has been described by the confined layer slip model, first proposed by Misra et al.[3.22].

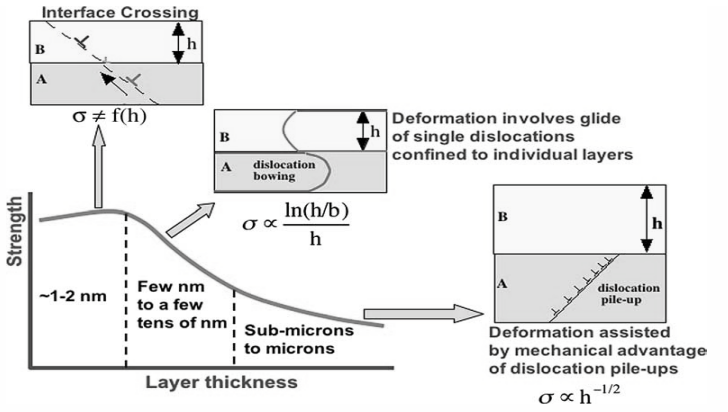

Figure 3.1: As individual layer thickness decreases in a multilayer system, strength increases to a critical point, above that, deformation is governed by the confinement of dislocations to individual layers[3.3].

3.1.1. Background

The hardness and strengthening mechanisms of FCC/FCC and FCC/BCC nanolaminate systems has been studied extensively[3.1-11]. To date, most published nanolaminate research has looked primarily at Cu/Ni systems due to the coherent interface that is seen between copper and nickel[3.2,3.23-28]. Similarly Cu/Nb systems have also been observed at length because of the incoherent interface between copper and niobium[3.3,3.4,3.17,3.24,3.28,3.29]. Other studies have also focused on Cu/Ag[3.5,3.14,3.26,3.28,3.30], as well as Cu/W[3.7-9], and Pt/Mo[3.16,3.21].

A coherent multilayer is one in which contains coherent interfaces, which is achieved by making an interface with materials that have the same crystal structure and no more than a minimal mismatch of lattice spacing. The low mismatch allows the amount of strain needed to accommodate continuous crystalline planes across the interface to be kept at a minimum. When either the lattice mismatch is either too great or different crystal structures

exist, then the interface will be incoherent and slip systems will be discontinuous across the interface.

Although the as-deposited properties of these nanolaminate systems have been well characterized, the effects of thermal cycling or accelerated aging on the mechanical behavior of multilayer systems have been largely overlooked and rarely studied in literature. To the author's knowledge, there are only two studies in which multilayer systems have been subjected to a heat treatment and subsequently mechanically tested[3.16,3.17]. Those studies have revealed that the effect of thermal treatment on hardness and structure of multilayer systems is significant, but the two studies identify different problems. The first study utilized a heat treatment process under ambient atmosphere and as a result significant oxidation and reductions in hardness were observed (Figure 3.2)[3.16]. The second study utilized a heat treatment process under ultra-high vacuum (UHV: $\leq 1\times10^{-7}$ Torr) on Cu/Nb multilayer samples that had been peeled from their substrates prior to the heat treatment. After microstructural characterization by TEM and hardness measurement by nanoindentation, the authors were able to show that aging significantly changed the systems observed. However, these changes only occurred at higher temperatures and longer times compared to the other study[3.16,3.17]. Further, the observed softening did not occur in

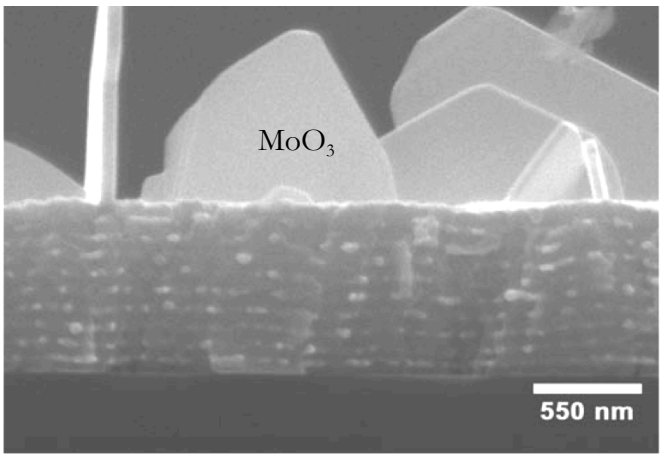

Figure 3.2: Significant MoO_3 formation on the surface of Pt/Mo multilayers after heat treatment under ambient atmosphere led to substantial decreases in hardness[3.16]. In this system the Mo layer was the base layer followed by Pt.

the thicker samples examined (Figure 3.3), it was proposed that the larger layer thickness allows stable geometry to form[3.17]. Studies have used a variety of methods to examine accelerated aging in thin film systems by methods of heating[3.16,3.17], as well as more non-traditional methods such as the application of alternating current to cause Joule heating[3.38].

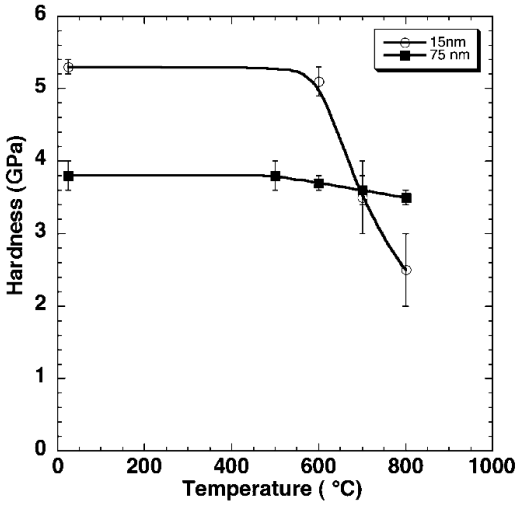

Figure 3.3: Influence of layer thickness on changes in hardness with respect to annealing temperature in UHV of Cu/Nb multilayers[3.17].

The multilayer systems used in this study were produced using magnetron sputter deposition. Sputter deposition is a physical vapor deposition (PVD) technique that utilizes ionized argon plasma to bombard the source material, which ejects source atoms that deposit onto other surfaces, like the substrate. Sputter deposition is a common technique used for thin film multilayer production due to the ability to precisely control microstructure and layer thickness of each individual layer[3.1].

3.1.2. Objective of the Study – Hypothesis

As previously discussed, two specific studies produced varying results on the effect of accelerated aging on multilayer systems[3.16,3.17]. It is the primary objective of this

investigation to examine the effect of oxygen in accelerated aging environments on the hardness of aged nanolaminate Cu/Nb films. This will be done by varying the atmosphere during the accelerated aging process. The three different atmospheres that have been chosen are: high purity argon, an argon/oxygen mixture, and ambient air. To observe effects of aging cross-sectional SEM and nanoindentation will be performed.

Additionally, literature containing hexagonal close packed (HCP) systems in metallic multilayers has not been found. The second objective of this study is to use Ti/W as a model HCP/BCC nanolaminate system. It will be produced and aged in a consistent manner with the Cu/Nb system. Following production it will examined similarly to the Cu/Nb samples and compared.

The previous studies have identified a higher hardness and susceptibility to softening of multilayer systems with individual layer thicknesses less than ≈75 nm[3.3,3.16]. For the purposes of this investigation, two individual layer thicknesses will be utilized, a thinner 20nm individual layer thickness sample set, and a thicker 100nm individual layer set. All samples will have a total film thickness of approximately 1000nm.

3.2. Experimental Methods

3.2.1. Sample Fabrication

Multilayer samples were fabricated using magnetron sputter deposition methods. The sputtering system used for this study is a system originally supplied by Kurt J. Lesker Co. that has been modified since its original installation. It now includes two separate magnetron power supplies for independent control of each of the sputtering sources, a radio

frequency (RF) Advanced Energy RFX-600 and a newly installed direct current (DC) Advanced Energy MDX-500.

Initial sputtering parameters for Cu and Nb were found in literature and adapted for use in this study[3.17]. The final sputtering parameters used for each film component are presented in Table 3.1. The Cu and Nb sputter targets were purchased from ACI Alloys Inc. The purities of each target are also shown in Table 3.1.

Table 3.1: Final sputtering parameters for Cu and Nb layers

	Cu (99.99%)	Nb (99.95%)
Base Pressure (Vac)	$\approx 7*10^{-7}$ Torr	$\approx 7*10^{-7}$ Torr
Process Pressure (Ar)	$9.9*10^{-3}$ Torr	$9.9*10^{-3}$ Torr
Power	100 Watts DC	200 Watts RF
Rate	4.9 nm/min	2.9 nm/min

Each multilayer sample was deposited on N-type (100) silicon wafers doped with phosphorus that had been purchased from Wafer World Inc. Before deposition each wafer was rinsed in acetone, isopropyl alcohol, deinonized water, acetone, and finally isopropyl alcohol in a stepwise manner. After rinsing, the substrates were then dried on a 100°C hot plate for five minutes. Once dry, the substrates were then plasma cleaned for five minutes at high power setting in a Harrick Plasma PDC-001, plasma cleaner. These cleaning procedures were seen elsewhere in literature to aid in film adhesion, specifically the rinsing[3.32], and plasma cleaning[3.33].

After thorough cleaning of each substrate, the silicon wafers were then placed into the sputter chamber and multilayer films were deposited. As identified in the objective, there are significant deviations in mechanical and aging behavior in multilayer systems below ≈75 nm. In order to examine this further, samples both above and below the transition were produced with either 20 nm or 100 nm layers for a total thickness of 1000 nm. In addition to the multilayer systems that were deposited, 1000 nm single component films were also produced using the same procedure. After deposition all samples were transferred to a glove box (Plas-Labs Inc.) containing ultra-carrier grade argon (99.9995% Ar, <0.5 PPM O_2) for storage.

3.2.2. Accelerated Aging Procedure

Following deposition each sample was subjected to a heat treatment procedure to simulate accelerated aging. Based on the different results seen in atmospheres of both ambient air[3.16] and UHV[3.17], additional heat treatment atmospheres were chosen. The three atmospheres chosen are first, a high purity ultra-carrier grade argon (99.9995% Ar, <0.5 PPM O_2), second, an argon/oxygen blend (97.9% Ar, 2.1% O_2), and finally ambient air (assumed ≈78% N_2, ≈21% O_2, ≈1% Ar). The argon/oxygen blend was chosen to represent an order of magnitude reduction in oxygen concentration when compared with ambient air.

The samples were placed into a glove box; the main compartment of the glove box was then filled with the desired gas. After filling, the chamber was then flushed and refilled with the process gas a minimum of three times to ensure proper gas content, per the manufacturer's suggestion. A hot plate located inside of the glove box was used for heating. The samples were placed onto the hotplate which was then heated to 400°C and held for 30

minutes. After 30 minutes, the hot plate was turned off and allowed to cool for five minutes. After that point the samples were removed from the hot plate and remained inside the glove box until fully cooled. A summary of the samples subjected to accelerated aging is shown in Table 3.2.

Table 3.2: Outline of different aged Cu/Nb samples

System	Cu/Nb (1000 nm total thickness)
Unaged	20 nm Cu/Nb & 100 nm Cu/Nb
Ar Atmosphere (99.9995% Ar, <0.5 PPM O_2)	20 nm Cu/Nb & 100 nm Cu/Nb
Ambient Atmosphere (Assumed ≈78% N_2, ≈21% O_2, ≈1% Ar)	20 nm Cu/Nb & 100 nm Cu/Nb
Ar/0 Atmosphere (97.9%/2.1%)	20 nm Cu/Nb & 100 nm Cu/Nb

3.2.3. Residual Stress Calculation

In this study, a Veeco™ Dektak^3 diamond stylus profilometer was used to measure substrate curvature. The technique of profilometry and residual stress calculation with Stoney's equation is discussed in greater detail in Section 2.5. Curvature measurements were taken in the center of each silicon wafer using a 30 mm scan length and analyzing the middle 20 mm of each scan. The reduced analysis region is per the manufacturers instructions. Measurements of each substrate were performed before and after deposition, as well as after aging. Each time a total of five measurements were collected for the same location on the wafer.

3.2.4. Observation of Structure

In order to measure individual layer thickness, total layer thickness, as well as observe approximate grain size and overall microstructure it was necessary to utilize SEM. Cross-sectional SEM views were obtained by cleaving the silicon substrate immediately prior to insertion into the microscope. SEM imaging of all multilayer samples were done using a Hitachi SU-6600 variable pressure field emission SEM. The imaging was done in high vacuum at an accelerating voltage of 10.0 kV. This technique is discussed in greater detail in Chapter Two.

3.2.5. Measurement of Mechanical Properties

Changes in mechanical properties of the multilayer systems were measured by nanoindentation. Nanoindentation was performed using a Hysitron™ Triboscope nanoindentation transducer with a Digital Instruments™ Multimode AFM piezoelectric base. The nanoindentation probe used was a diamond Berkovich tip. Each sample was cleaved into a smaller size (≈1 cm^2) then affixed to an AFM sample disc (Ted Pella Inc.) with Loctite™ cyanoacrylate glue before insertion on the AFM base. Samples were each subjected to a total of 22 indents, two each at 11 maximum depths ranging from 100 nm to 50 nm in five nanometer increments. The indents were performed using depth controlled loading with a five second loading portion to the maximum depth, a five second hold at the maximum depth, and a five second unloading portion. Each indent was taken a minimum of 10 μm away from any previous indentation sites in order to avoid any influence from existing plastic deformation zones. Oliver-Pharr analysis was used and the maximum indentation depth did not exceed 10% of the total film thickness.

3.2.6. Film Orientation and Texturing

X-Ray diffraction was used in this study to assess the crystal structure of the films produced. XRD was performed using a Rigaku Ultima IV multipurpose XRD system with a Cu Kα X-ray source. The unaged and Ar aged 100 nm Cu/Nb films were tested from 1° to 140° at a scan rate of 0.3°/minute and the single component Cu and Nb films were tested from 1 to 140° at a scan rate of 0.6°/minute. Further plans for additional XRD testing can be found in Chapter Five. For comparison, XRD simulations were generated using CaRIne Crystallography V.3.1., a software suite that can simulate XRD spectra based on crystallographic information. CaRIne was used to generate reference spectra for ideal Cu, Nb, and Si.

3.3. Results and Discussion

3.3.1. Properties of As-Deposited Multilayer Cu/Nb

The unaged films were examined with SEM to observe grain structure and multilayer geometry; the results are shown in Figure 3.4.

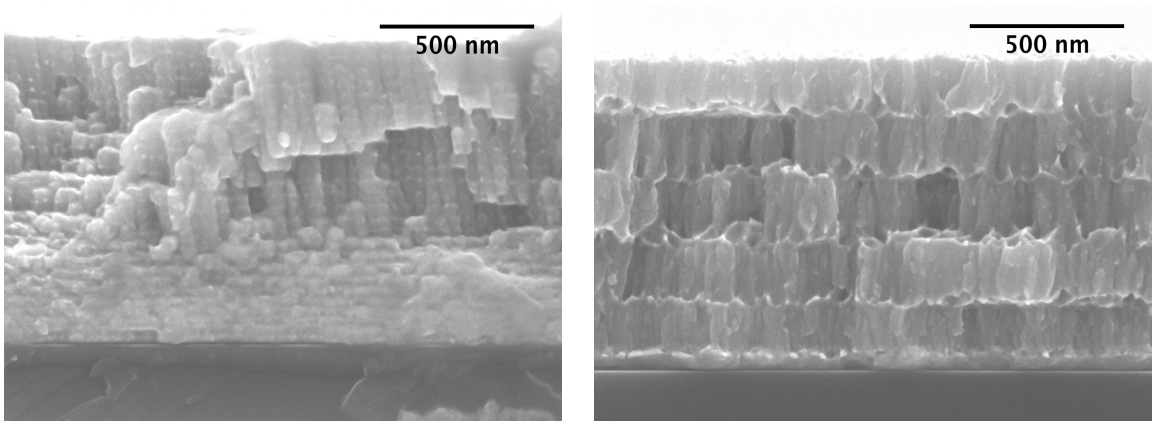

Figure 3.4: Cross-Sections of unaged Cu/Nb multilayers: 20 nm (left) and 100 nm (right) layer thicknesses. These systems used Cu as the base layer and Nb as the capping layer. Images include silicon substrate.

Initial SEM images show multilayer geometry as expected, they also verify intended length scales and show desired microstructures as can be seen in Figure 3.4.

The hardness of as-deposited Cu/Nb nanolaminates was measured to 5.5±0.3 GPa for the 20 nm individual layer thickness system and 4.3±0.3 GPa for the 100 nm system. These values are comparable to those seen elsewhere for similar Cu/Nb systems[3.3,3.17].

3.3.2. Structure and Direct Observation of Accelerated Aged Multilayer Cu/Nb

Following accelerated aging, samples were freshly cleaved and observed under SEM; examples are shown in Figure 3.5.

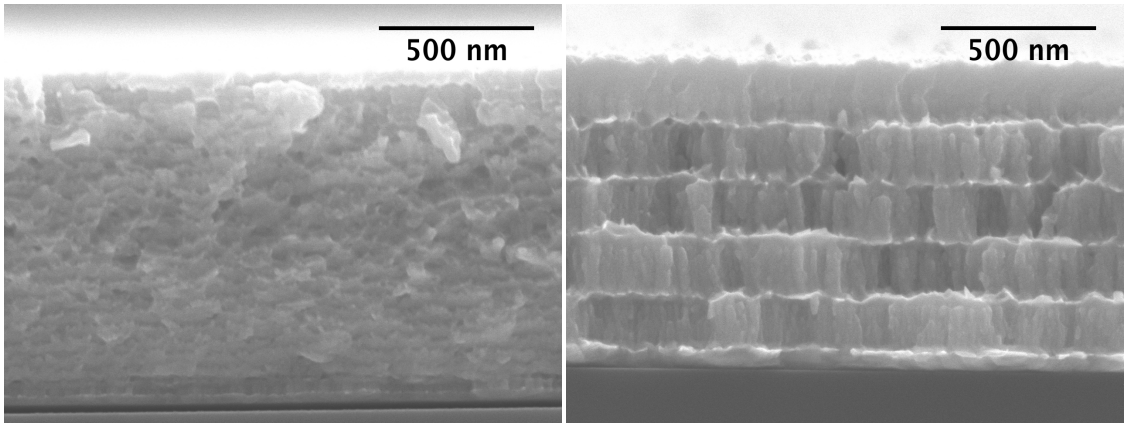

Figure 3.5: Cross-Sections of aged Cu/Nb multilayers: 20 nm (left) and 100 nm (right) layer thicknesses, aged in Ar. These systems used Cu as the base layer and Nb as the capping layer. Images include silicon substrate.

It can be seen that in Figure 3.5, there is a significant loss of overall multilayer geometry as is seen in Figure 3.4, for the 20 nm Cu/Nb system. However, no effect is seen in the 100 nm film in Figure 3.5. The high purity argon aged samples are shown above, but this trend is similar for all aging atmospheres. Additional images for other atmospheres are included in Appendix C.

3.3.3. Mechanical Properties of Accelerated Aged Multilayer Cu/Nb

The hardness of the accelerated aged samples as a function of treatment atmosphere was measured and is presented in Table 3.3 and Figure 3.6.

Table 3.3: Average hardness of Cu/Nb multilayers from nanoindentation testing

System	Cu/Nb 20 nm	Cu/Nb 100 nm
Unaged	5.5±0.3	4.3±0.3
Aged in Ar	1.3±0.5	4.8±0.4
Aged in Ambient	2.2±0.6	4.8±0.6
Aged in Ar/O	3.5±0.4	5.1±0.3
Hardness of Cu/Nb Multilayers (GPa)		

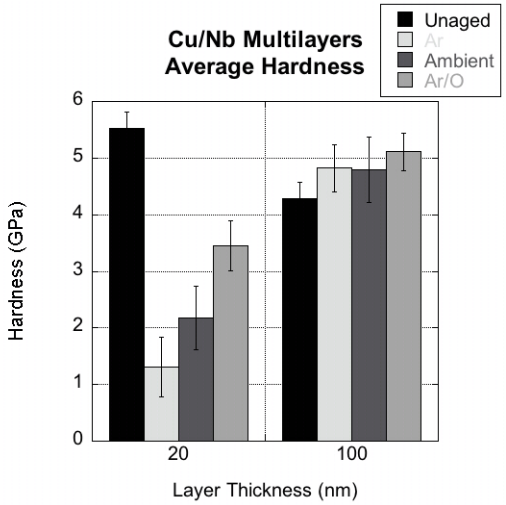

Figure 3.6: The observed changes in hardness upon accelerated aging of Cu/Nb multilayer films, 20 nm samples show significant drops in hardness after thermal treatment, but little to no change is seen in 100 nm samples. Exact effect of annealing atmosphere is not clear.

It was seen through nanoindentation that the heat treatment of the 20 nm Cu/Nb systems caused significant losses in hardness regardless of heat treatment atmosphere. However, this decrease did not occur in the 100 nm Cu/Nb systems, which remain

consistent in hardness regardless of atmosphere. These results show that, at the levels used, oxidation is not a major factor in hardness of multilayer Cu/Nb.

Taking into account the conclusions from Bellou, et al., on Pt/Mo multilayers the changes in hardness seen in Figure 3.6 are expected[3.16]. But, as shown in Figure 3.2, aging of the Pt/Mo films caused significant oxidation, which in turn drastically changed the hardness[3.16]. Significant oxidation was not observed in this study, which can be seen in the cross-sectional SEM images taken (Figure 3.5). However, Bellou, et al., is not the only study to use nanoindentation to quantify changes in hardness of nanolaminates. As previously discussed, Misra, et al., did not observe changes in hardness until higher temperatures and longer aging times for similar Cu/Nb systems[3.17]. As seen in Figure 3.7 the softening was observed in this study at significantly lower temperatures than seen elsewhere in literature[3.17]. It is hypothesized that the cause of the change in temperature needed to observe softening is due to the stresses imposed by the silicon substrate, which was not present in the other study[3.17].

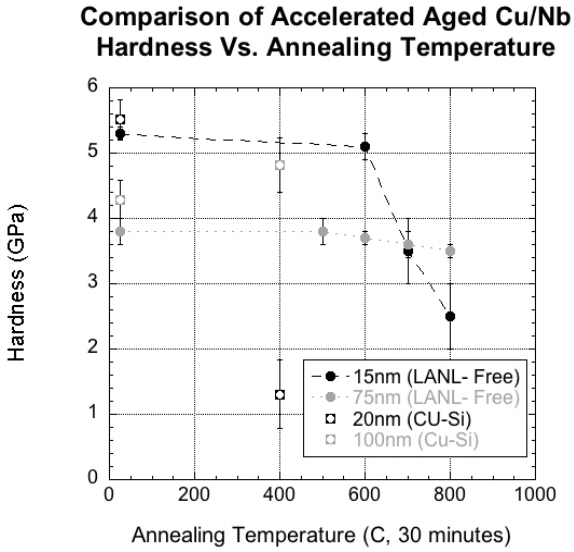

Figure 3.7: The changes in hardness with respect to annealing temperature of Cu/Nb multilayer films, values compared with those found in literature[3.17]. The LANL study peeled the multilayer films from their substrates prior to aging[3.17], which was not done in this study.

Overall, it was seen that the different atmospheric oxygen concentrations during heating did not cause a distinct or significant effect. From this, it is concluded that the major factor affecting accelerated aging in multilayer Cu/Nb systems cannot be controlled by reducing oxygen concentration to below 1 ppm.

3.3.4. Residual Stress of Cu/Nb Systems

As discussed in Section 3.2.3., changes in substrate curvature were measured using a diamond stylus profilometer. Following those measurements, Stoney's equation was used to calculate residual stress[3.36]. The results of these calculations are shown below in Table 3.4.

Table 3.4: The observed changes in residual stress estimations calculated from changes in silicon substrate curvature. Positive values denote tensile stress; negative values denote compressive stress. It can be seen that upon accelerated aging treatment, all films are left with higher tensile stress than before aging. These calculations represent an average stress over a wide (20 mm) area.

Aging Condition	Cu/Nb 20 nm	Cu/Nb 100 nm
Unaged	22.7±0.3 MPa	12.2±0.3 MPa
Ar	48.9±0.3 MPa	22.0±0.1 MPa
Ambient	63.4±0.2 MPa	15.4±1.7 MPa
Ar/O	66.7±0.2 MPa	25.5±0.1 MPa
Values reported are calculated from average curvature measurement		

The CTE mismatch between the silicon substrates and the metal films suggest that tensile stresses developed after heating should be expected. The CTE's for Cu and Nb are higher than Si as shown in Table 3.5[3.15], meaning the films will contract more than the silicon substrate upon cooling. Taking the greater thermal expansion in the film during heating into account, the multilayers should reach a point of zero stress during heating. This is due to the to the thermal expansion mismatch causing an overall compressive stress on heating to nullify the initial tensile stress. However this estimation is not sufficient to analyze the stress state during heating, a possible significant factor on diffusivity during heat treatment as well as mechanical behavior.

Table 3.5: Average CTE values for Cu, Nb and Si ≈200°C[3.15].

	Cu	Nb	Si
CTE	18.5 μm/m°C	7.38 μm/m°C	3.61 μm/m°C

3.3.5. Orientation and Texturing of Cu and Nb Films

Initial XRD results of the single component films show that they are highly textured, showing strong preference to certain crystal directions. Comparing Figure 3.8 with Table 3.6 shows that there is a strong preference for (111) Cu grains. However there is also a peak measured at 69.6° which is not attributed to anything in the Cu system, at this time this is an unknown peak.

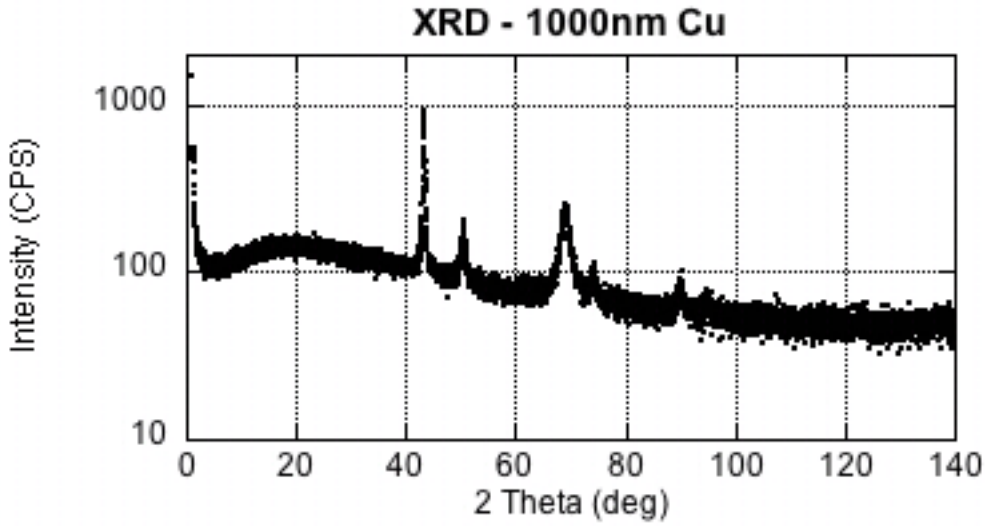

Figure 3.8: Measured XRD spectra of unaged 1000nm single component Cu film. Major peaks were measured at 43.3° and 69.6° 2Θ.

Table 3.6: Simulated XRD spectra of single crystal Cu. Major peak at 43.38° indicates Cu (111).

Crystal Direction	2 Theta	Relative Intensity
(111)	43.38°	100%
(200)	50.52°	45%
(220)	74.24°	22%
(311)	90.09°	23%
(222)	95.32°	7%
(400)	117.19°	4%

Similarly, the single component Nb system also shows strong orientation. Major peaks were measured in the Nb system at 69.0° and 38.3° which are thought to correspond to the (211) and (110) directions in Nb respectively, which can be seen in Figure 3.9 and Table 3.7. The shift from the predicted 2Θ value of 69.7° to 69.0° could possibly be caused by the stresses noted in Section 3.3.3.

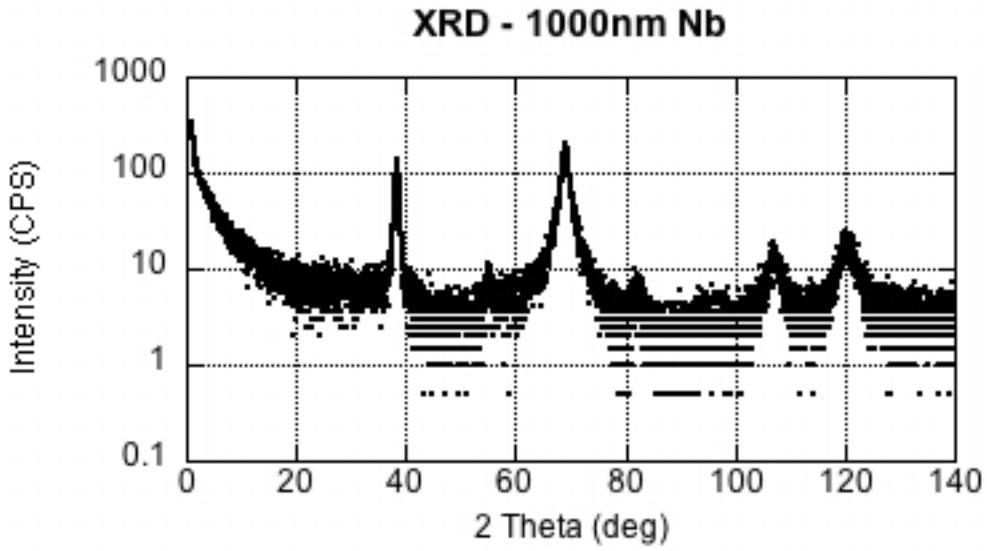

Figure 3.9: Measured XRD spectra of unaged 1000nm single component Nb film. Major peaks were measured at 69.0° and 38.3° 2Θ.

Table 3.7: Simulated XRD spectra of single crystal Nb. Major peak at 38.5° indicates Nb (110), minor peak at 69.7° indicates Nb (211).

Crystal Direction	2 Theta	Relative Intensity
(110)	38.55°	100%
(200)	55.66°	15%
(211)	69.75°	26%
(220)	82.63°	7%
(310)	95.15°	10%
(222)	107.92°	3%

It can be seen in Figures 3.10 and 3.11 that the aging procedure did not cause significant changes in the XRD measurements of the film systems. From both spectra major peaks

were measured near 69.1°, which are thought to correspond with the (211) peak also seen in Figure 3.10. Results of silicon XRD simulation are included in Table 3.8.

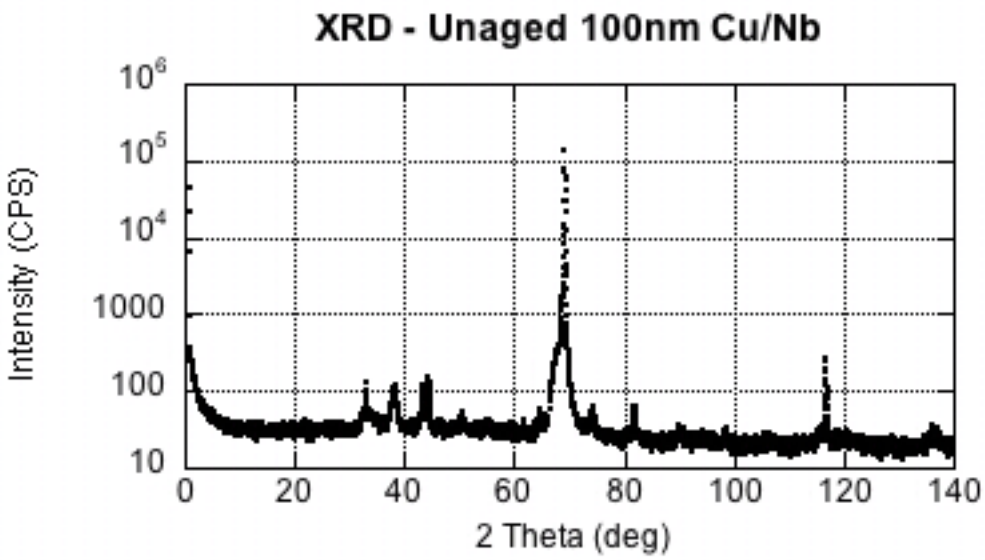

Figure 3.10: Measured XRD spectra of unaged 100nm Cu/Nb nanolaminate system. A major peak was measured at 69.1° 2Θ.

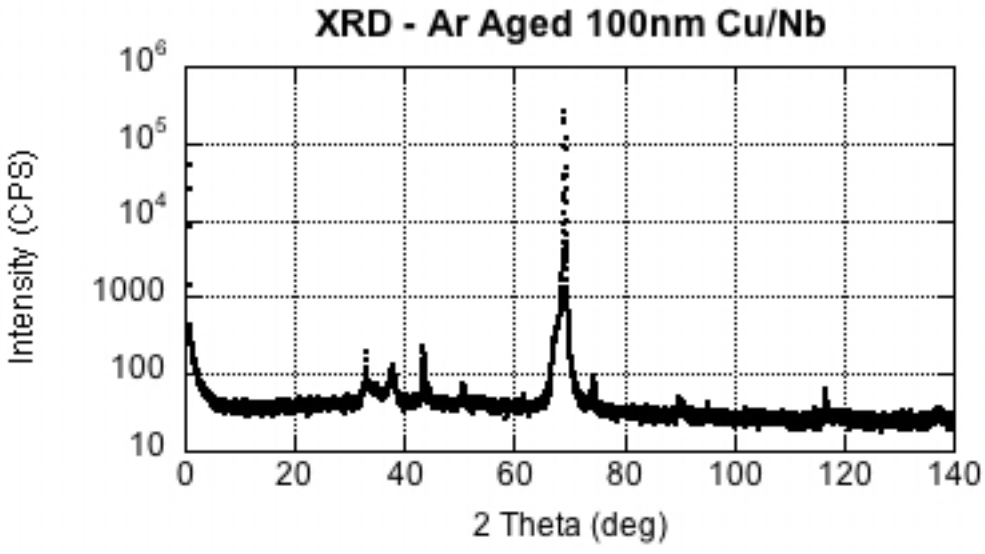

Figure 3.11: Measured XRD spectra of Ar aged 100nm Cu/Nb nanolaminate system. A major peak was measured at 69.2° 2Θ.

Table 3.8: Simulated XRD spectra of single crystal Si. Major peak at 28.5° indicates Si (111), minor peaks at 47.3° and 56.1° indicates Si (220) and (311) respectively.

Crystal Direction	2 Theta	Relative Intensity
(111)	28.5°	100%
(220)	47.3°	42%
(311)	56.1°	20%
(400)	69.1°	4%
(331)	76.4°	5.8%
(422)	88.0°	7.4%
(511)/(333)	95.0°	4%
(531)	114.0°	5%

Preliminary XRD analysis, Figures 3.10 and 3.11, showed that no significant intermetallic compounds were formed during the accelerated of 100nm Cu/Nb in Ar. All major peaks observed can be attributed to those from the Cu and Nb systems and not those from Si, as shown in Table 3.8.

The Rigaku system used is calibrated and primarily used for powder diffraction, not thin films. As is further described in Chapter Five, these preliminary results served to show the researchers that it is necessary to pursue other options for XRD analysis.

3.4. Expansion of Study to HCP Systems

As previously discussed, no literature has been found that includes nanolaminate film systems containing metals with HCP crystal structures. This investigation will utilize Ti/W as a multilayer system to broaden the study of model incoherent multilayer systems. The

second major objective of this particular nanolaminate investigation is to attempt to expand observations seen in FCC/BCC systems to include systems including HCP crystal structures.

3.4.1. Experimental Methods

The expansion of this study to hexagonal systems follows the same method that the Cu/Nb study used. First the samples were fabricated following the same procedures described in Section 3.2.1. The deposition parameters for titanium and tungsten can be found in Table 3.9. The Ti/W nanolaminates produced had 20 nm and 100 nm layer thickness for a total of 1000 nm. Following deposition they were aged as described in Section 3.2.2. under the conditions shown in Table 3.10.

Table 3.9: Final sputtering parameters for Ti and W layers

	Ti (99.995%)	**W (99.95%)**
Base Pressure (Vac)	≈$7*10^{-7}$ Torr	≈$7*10^{-7}$ Torr
Process Pressure (Ar)	$1.2*10^{-2}$ Torr	$1.2*10^{-2}$ Torr
Power	100 Watts DC	200 Watts RF
Rate	1 nm/min	2.5 nm/min

Table 3.10: Outline of different aged Ti/W Samples

System	Ti/W (1000 nm total thickness)
Unaged	20 nm Ti/W & 100 nm Ti/W
Ar Atmosphere (99.9995% Ar, <0.5 PPM O_2)	20 nm Ti/W & 100 nm Ti/W
Ambient Atmosphere (Assumed ≈78% N_2, ≈21% O_2, ≈1% Ar)	20 nm Ti/W & 100 nm Ti/W
Ar/0 Atmosphere (97.9%/2.1%)	20 nm Ti/W & 100 nm Ti/W

The Ti/W films were subjected to observation under TEM, nanoindentation, and estimation of residual stress by changes in substrate curvature. Testing procedures for Ti/W systems were consistent with those described for the Cu/Nb systems in Section 3.2.

3.4.2. Results and Discussion

Sputtering parameters used for Ti and W deposition were determined experimentally with the assistance of the structure zone model (SZM)[3.31]. Early Ti and W films showed substantial voiding and uneven grains (Figure 3.12); as a result, argon processing pressure was reduced to refine grain structure.

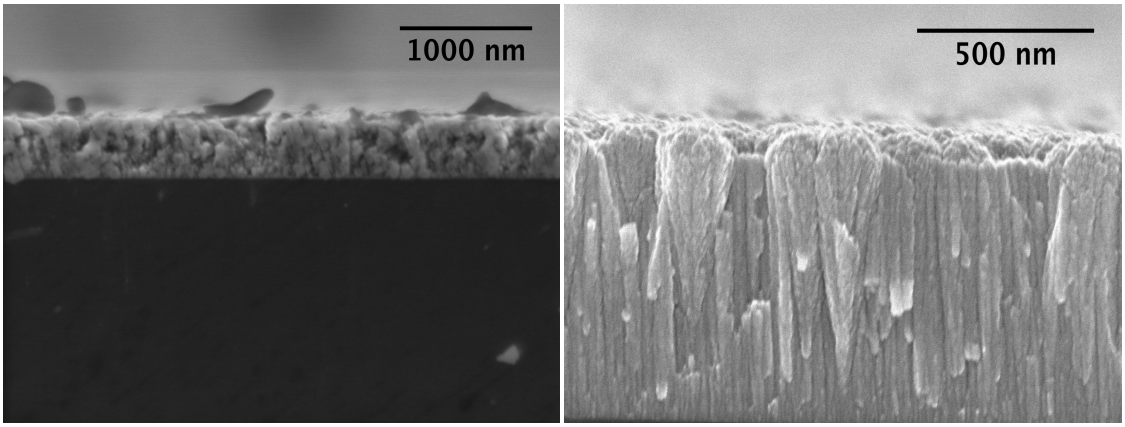

Figure 3.12: Initial Ti and W films as seen from cross-sectional SEM. Ti film shows substantial voiding (left); W film shows uneven grain structure (right). Following the structures seen here, sputtering parameters were further refined.

As expected and desired, initial SEM images show multilayer geometry, they also verify intended length scales and show microstructures as can be seen in Figure 3.13. Nanoindentation of as-deposited Ti-W multilayers measured hardnesses of 15.4±1.3 GPa and 11.6±0.3 GPa for the 20nm and 100nm layer thickness systems respectively. As discussed, comparable HCP/BCC systems have not been found in existing literature but these values are consistent with sputtered W films measured by nanoindentation[3.34,3.35]. When compared to the Cu/Nb systems, a similar length scale trend is seen in the Ti/W system. Further, the trends comply with the confined layer slip model[3.3].

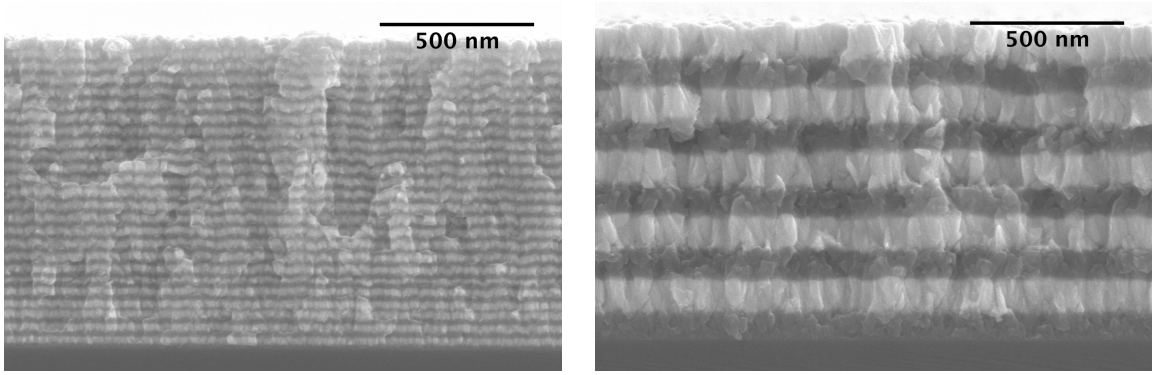

Figure 3.13: Cross-Sections of unaged Ti/W multilayers: 20 nm (left) and 100 nm (right) layer thicknesses. These systems used Ti as the base layer and W as the capping layer. Images include silicon substrate.

After accelerated aging, the nanolaminates were again examined using SEM; the results are shown in Figure 3.14. Similar to the Cu/Nb systems shown in Section 3.3.2, the 20 nm Ti/W system in Figure 3.14 shows a significant loss of contrast near the surface of the film as can be seen in Figure 3.5. As in Section 3.3.2., the Ar aged samples are shown in Figure 3.14; the other aging atmospheres showed similar results and have been included in Appendix C.

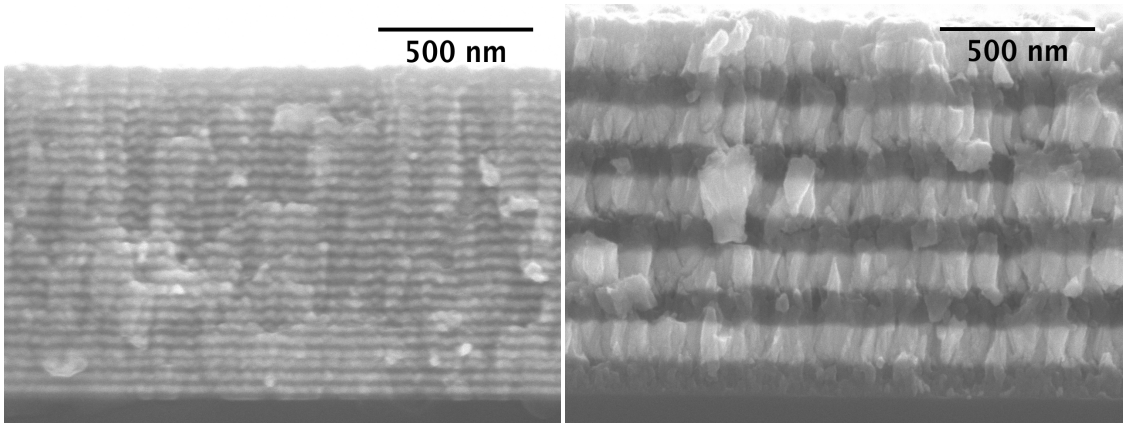

Figure 3.14: Cross-Sections of aged Ti/W multilayers: 20 nm (left) and 100 nm (right) layer thicknesses, aged in Ar. These systems used Ti as the base layer and W as the capping layer. Images include silicon substrate.

The hardnesses measured from Ti/W films after accelerated aging are shown in Table 3.11 and Figure 3.15.

Table 3.11: Average hardness of Ti/W multilayers from nanoindentation testing

System	Ti/W 20 nm	Ti/W 100 nm
Unaged	15.4±1.3	11.6±0.3
Aged in Ar	13.5±1.2	10.3±1.4
Aged in Ambient	13.0±1.0	11.3±2.1
Aged in Ar/O	10.0±0.7	9.1±0.7
Hardness of Ti/W Multilayers (GPa)		

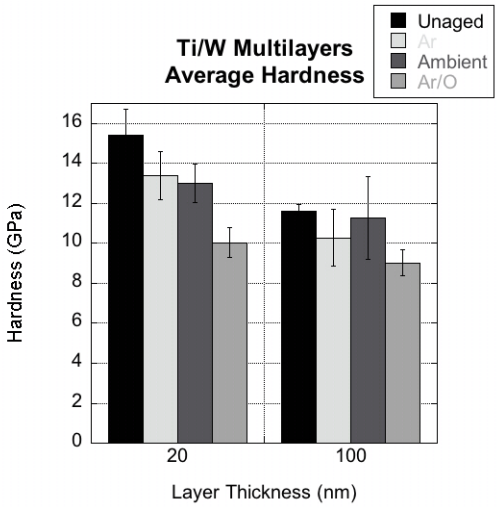

Figure 3.15: The observed changes in hardness upon accelerated aging of Ti/W multilayer films, 20 nm samples show significant drops in hardness after thermal treatment, but little to no change is seen in 100 nm samples. Exact effect of annealing atmosphere is not clear.

As seen in Figure 3.15 the hardness of accelerated aged Ti/W shows similar results to the Cu/Nb system. The 20 nm Ti/W shows significant softening but the 100 nm system does not. The magnitude of softening is less than that seen in the 20 nm Cu/Nb system but this is expected because of the melting temperatures of each component. Cu melts at 1083°C, whereas Ti melts at 1660°C, and Nb at 2468°C, compared with W melting at 3370°C[3.15]. Consistent with the results of the Cu/Nb system, there is no significant trend in the heating atmosphere.

The average residual stress of Ti/W nanolaminate films, calculated by Stoney's equation[3.36] and substrate curvature measurements are shown below in Table 3.12.

Table 3.12: The observed changes in residual stress estimations calculated from changes in silicon substrate curvature. Positive values denote tensile stress; negative values denote compressive stress. It can be seen that upon accelerated aging treatment, all films are left with higher tensile stress than before aging. The thick Ti/W systems show an initial compressive stress before aging. These calculations represent an average compressive stress over a wide (20 mm) area.

Aging Condition	Ti/W 20 nm	Ti/W 100 nm
Unaged	12.0±0.1 MPa	-10.2±0.4 MPa
Ar	93.6±0.3 MPa	70.4±0.2 MPa
Ambient	98.9±0.3 MPa	77.2±0.3 MPa
Ar/O	97.3±0.2 MPa	44.9±0.4 MPa
Values reported are calculated from average curvature measurement		

Considering the CTE mismatch between the silicon substrates and the metal films again, the tensile stresses developed after heating are expected. However the results are still not entirely consistent when compared with the Cu/Nb system, as the CTE's for Cu and Nb are higher than Ti and W as shown in Table 3.13[3.15]. Based purely on stresses induced on cooling by CTE mismatch, one would expect the Cu/Nb systems to show a higher compressive residual stress than comparable Ti/W systems. Therefore, there must be another cause for the deviations in post-annealing compressive residual stresses seen in both systems.

Table 3.13: Average CTE values for Ti, W, Cu, Nb and Si ≈200°C[3.15].

	Ti	W	Cu	Nb	Si
CTE	8.90 μm/m°C	4.4 μm/m°C	18.5 μm/m°C	7.38 μm/m°C	3.61 μm/m°C

3.5. Conclusion

Nanoscale multilayer films have been seen to exhibit hardness that are consistent with nanolaminate film systems produced elsewhere[3.3,3.17,3.34,3.35]. The stability of nanolaminate systems is limited due to the increased diffusion in the high degree of interfacial area as well as grain boundaries. As other literature has pointed out, the increased hardness seen in multilayer geometries is due to the constrictions on dislocation motion imposed by grain boundaries[3.3,3.24]. These two features contribute to systems that do not retain their properties even through short exposures to elevated temperatures. This was shown through decreases in hardness of 20 nm individual layer thickness Cu/Nb and Ti/W samples measured by nanoindentation. As a result, if metallic nanoscale multilayers are to be applied in elevated temperature environments, there is a compromise that must be made, decreased layer thickness yields higher hardness initially, but becomes sensitive to instability of multilayer geometry. Through this work, the effect of oxygen concentration in heat treatment atmosphere on Cu/Nb and Ti/W nanolaminates is not immediately clear. For the conditions shown in this study, oxidation was not the primary cause for the softening observed in Cu/Nb and Ti/W nanolaminate films.

The softening observed in this study, occurred at lower temperatures and shorter times than those previously reported in Cu/Nb systems[3.17]. It is hypothesized that this is due to the stresses imposed on the film systems by the silicon substrate. In the earlier study[3.17], films were peeled from their substrates prior to heat treatment, allowing relaxation in the films. Research has shown that the film constraint imposed by the substrate in copper thin films causes significant changes on the residual stress due to thermal cycling[3.37].

For the conditions shown in this study, HCP/BCC systems exhibit hardnesses consistent with FCC/FCC and FCC/BCC systems looked at elsewhere[3.1,3.3,3.16,3.17,3.22]. The hardness after accelerated aging measured in Ti/W is similar to the Cu/Nb systems also measured. The Ti/W exhibited more mechanical stability after accelerated aging for the conditions shown when compared to Cu/Nb systems. It is hypothesized that the increased stability is attributed to the higher melting temperatures of each of the components.

CHAPTER FOUR

NANOCOMPOSITE FILLER INFLUENCE ON THE MECHANICAL PROPERTIES AND SURFACE DEGRADATION OF POLYIMIDES FOR NASA APPLICATIONS

4.1. Introduction to Polyimide Nanocomposites

Polyimide nanocomposites are matrix-filler type composites, which utilize an polyimide matrix and contain nanoparticles as the filler material. Many research groups have incorporated nano-scaled filler materials into polymer matrices to alter the physical properties, mechanical behavior, and fracture toughness of the resulting composites[4.1-11]. The end result depends both on the polymer matrix, which can range from soft thermoplastics to stiff thermoset polymers, as well as the filler material, which can range in composition, shape, and scale. Articles have highlighted the importance of some filler properties on the nanocomposite mechanical response including filler size[4.8,4.9], surface area[4.1,4.2], surface interaction[4.6-8,11], and spacing of the particles[4.8-10]. Although basic composite rules, such as the rule of mixtures can guide the design of conventional composites[4.12], the impact of nano-scale fillers on overall mechanical properties of polymer composite systems is not well understood[4.6,4.7,4.9,4.11].

One class of polymer nanocomposites being developed at NASA utilize polyimide resin matrices. These polyimides show promise for use in aerospace applications, such as cryogenic propellant tanks and composite ductwork in jet engines[4.3,4.5]. The reduced weight and superior mechanical performance of the composite compared to the polymer matrix, suggest that composites are ideal for these applications. Groups such as the Structures and Materials Division at the NASA Glenn Research Center are interested the addition of nanoscale fillers as a way of improving the properties of various polymers. Their research

seeks to obtain discrete improvements in mechanical strength, high temperature stability, barrier properties (such as reduced gas absorption or diffusion), thermal conductivity, and electrical conductivity. By eliciting improvements in one or more of these properties, NASA has the ability to design better and more efficient (multifunctional) components for both aircraft and spacecraft. Such nanocomposites have applications as deployable structures, cryogenic propellant tanks, diffusion barrier films, or may be imparted with properties such as antimicrobial behavior by incorporating functional nanoparticles[4.5,4.13,4.14].

4.1.1. Background – General Polymer Nanocomposite Research

Recent polymer matrix nanocomposite research has shown that there are many more significant factors than conventional rules suggest. For example, there are conflicting views on the effect of particulate diameter on composite properties. As previously mentioned, classical composite strength theories do not account for filler size, only volume fraction, using a simple rule of mixtures[4.12]. However the importance of particle size was noted in a review published by Fu, et al.[4.8], in which multiple polymer nanocomposites studies indicate that there is a threshold size of nanoparticles. This group also concluded that above this threshold size, there was no size dependent improvement of elastic modulus. Similarly Wetzel, et al.[4.9,4.10], have authored multiple papers discussing the effects of particle size and dispersion on mechanical and tribological behavior of epoxy nanocomposites with alumina and other nanoparticles incorporated into the composite. Though the general assumption is that smaller particles yield stronger results, Ciprari, et al., found no such correlation[4.11]. In their study, no size effect was seen in dynamic mechanical analysis (DMA) or tensile testing of nano-composites. In addition, a negative influence was seen in nanoindentation data[4.11].

Also disputed is the effect of surface interaction on nanocomposite mechanical properties. It was reported by Fu, et al., that the effect of surface adhesion was minimal on Young's modulus[4.8]. However this is directly contradicted in Guo, et al., by particle surface-initiated polymerization (SIP) of polyurethane on iron oxide nanoparticles[4.6]. The composites formed by SIP were found to be much more flexible, withstanding 600% more strain than the nanocomposites formed by direct mixing. Thus far, the majority of the literature on nanocomposites has addressed the aspect of bulk properties of nanocomposite materials. In Ciprari, et al., they attempt to characterize the interphase region around the nanoparticles but were unsuccessful[4.11]. In that study the materials of interest were Al_2O_3 and Fe_3O_4 nanoparticles in PMMA and PS matrices. However, when the composites were examined through DMA, nanoindentation and tensile testing, as was stated earlier, no effect was seen in the DMA and tensile testing and a negative influence was observed via nanoindentation. In Wetzel, et al., their focus included tribological performance along with mechanical behavior[4.10]. It was seen that upon the initial addition of a low concentration of nanoparticles (<2 vol.%) the wear rate was reduced, however above that the rising concentration of hard alumina particles began to increase the wear rate. The improvements in mechanical properties are attributed to not only crack pinning but also other methods, which act by dissipating energy such as matrix shear yielding and particle pull out[4.10].

One of the few things not disagreed upon is the necessity for regular distribution of nanoparticles in the polymer matrix for strong nanocomposites. Particle agglomeration is seen as a detrimental property. In another Wetzel, et al., publication flexural testing, modulus of rupture, and fracture toughness were all performed on polymer nanocomposite systems[4.9]. It was found that the addition of nanoparticles dispersed in a polymer matrix via

high sheer mixing during production greatly increased the flexural strength and fracture toughness of a thermosetting polymer[4.9]. Also the SIP method investigated by Guo, et al., explored implications of distribution and agglomeration[4.7]. The SIP method decreases agglomeration, which was apparent when examined by SEM[4.7].

In addition to the different experimental variables studied, many of the publications use a variety of testing methods. As previously discussed the overall objective of this thesis is to use localized testing methods for nano-scaled composite systems. One such method for locally characterizing novel nanocomposites is nanoindentation. In his review article[4.15] Dasari discusses the use of nanoindentation on polymer nanocomposites. Because nanoindentation by nature is not a measure of bulk properties, it is subject to the effects of local crystallinity and cross-linking. Taking into consideration that a nanocomposite is a non-uniform material, nanoindentation holds a subjective position; one must ensure that objective results are obtained. This aspect was further noticed in Ciprari, et al., but was not explored in depth[4.11]. As for the validity of using nanoindentation to measure polymer systems, Jee and Lee examine a wide variety of polymers including multiple types of polyethylene. By comparing the results with those from direct optical observation and analysis of the indentation site, they validated the use of nanoindentation[4.16].

4.1.2. Background – Advances in Polyimide Composites by NASA

The Structures and Materials Division of NASA, located at the Glenn Research Center has studied polyimide resins and their composites for use in directed research and direct application for use in the aerospace industry[4.3-5,4.17,4.18]. In addition to mechanical properties, the addition of nanoparticles into polyimide resins has been of interest in

increasing their thermal oxidative stability (TOS)[4.3,4.4]. Previously, PMR-15, a polymer named for its synthesis from polymerization of monomeric reactants has been studied[4.3,4.17] and the oxidation behavior of PMR-15 is known[4.17]. But recently, research has been directed to find replacements for PMR-15 primarily due to the human toxicity of methylenedianiline (MDA). Miller[4.4] has previously studied other polyimides such as BAX-TAB resins and reported their superior thermal stability following nanoparticle addition.

Recently a series of polyimide resins with low-melt viscosities and high glass transition temperatures were developed by Chuang, et al.[4.18], which are suitable for resin transfer molding processes (RTM). These resins have the benefit of using no solvents. Their behavior when processed with nanoparticles into a nanocomposite has not been thoroughly explored, and their oxidative behavior has not been detailed to the extent of PMR-15[4.17]. The higher cure temperature needed for the RTM polymers however limits the use of the organically modified nanoparticles which have been utilized in PMR-15 nanocomposites.

4.1.3. Objective of the Study – Hypothesis

It is the objective of this study to examine the mechanical response of two polyimide resin nanocomposite systems that have been subjected to aging. The two different polyimide systems are PMR-15 and RTM-370, two polyimide resins that have potential uses in resin transfer molded fiber reinforced composites for aerospace applications. Previous research has shown that the relatively well-characterized PMR-15 suffers from oxidation damage during aging[4.17]; it is the goal of the study to show whether or not the presence of nanoparticles dispersed in the polyimide matrix will increase stability of PMR-15 against

surface oxidation. Similarly, RTM-370 is a polyimide that has similar applications and has been viewed as a potential replacement for PMR-15 in some aspects. RTM-370's susceptibility to thermo-oxidation damage as well as effects of nanoparticle incorporation will be examined. Effects of aging will be examined primarily mechanically by nanoindentation as well as optically.

4.2. Experimental Methods

The experimental procedure was carried out in two main phases: the sample production and aging phase, which was carried out at NASA's Glenn Research Center in Cleveland, Ohio, followed by the testing phase, which was carried out at Clemson University. Dr. S. Miller of NASA's Structures and Materials Division oversaw the production and aging phase of this study. Both of the polyimide resins utilized in this study were developed by the Structures and Materials division of NASA[4.3,4.18].

4.2.1. PMR-15 Production

Production of PMR-15 is done mainly in solution with methanol as the solvent. First, BTDE was prepared by refluxing BTDA in an amount of methanol calculated to yield a solution containing 50 wt% solids. The reflux was carried out for two hours after the solid BTDA had dissolved. After BTDE was prepared PMR-15 resins were further fabricated in several steps, as illustrated in Figure 4.1. The three monomers (NE, MDA, and BTDE) were dissolved in methanol (50 wt%) followed by solvent evaporation, on a hot plate, at 60° to 70°C. The mixture was b-staged in an air-circulating oven from 204°C to 232°C to yield a low molecular weight imide oligomer. The oligomer was then cured in a circular, 1" diameter, mold at 315°C under 2355 psi to produce the crosslinked polymer. The polymer

was post cured in an air-circulating oven for 16 hours at 315°C to further crosslinking. The average number of imide rings was kept constant by using a stoichiometry of 2NE/ (n+1) MDA/ nBTDE (n=2.087) corresponding to an average molecular weight of 1500. The overall structure of PMR-15 can be seen in Figure 4.1[4.3].

The procedure used to prepare PMR-15 nanocomposites was identical to that of the neat resin, except that 5wt% SAP-90, 5wt% PGV, or 0.5wt% CNF was added to the methanol solution of the monomers. The nanoparticles used are commercially available Pyrograf-III PR-19 XT-HHT carbon nanofiber (CNF) from Pyrograf Products Inc., PGV montmorillonite clay for Nanocor Inc. modified in a 50:50 ratio with MDA, and SAP-90 synthetic magnesiosilicate clay from Claytec Inc.

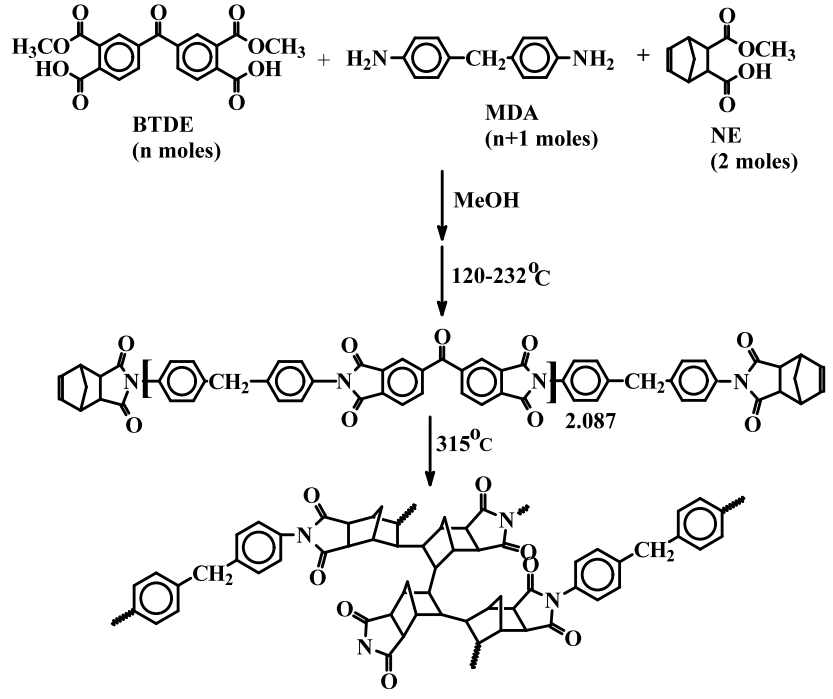

Figure 4.1: An illustration of the synthesis reactions and molecular structure of PMR-15 resin[4.3]

4.2.2. RTM-370 Production

Production of RTM-370 occurs in two main steps, first forming crosslinkable oligomer chains, and then second crosslinking those chains to form the polymer. In order to first form oligomer chains, the three constituents of RTM-370, asymmetrical biphenyldianhydride (a-BPDA), 3,4'-oxydianiline (3,4'-ODA), and 4-phenylethynylphthalic anhydride (PEPA) were melted together above 200°C for 1 hour to form the corresponding phenylethynyl endcapped polyimide oligomers. The endcapped oligomer was then sent to Georgia Tech for further preparation. Three batches were mixed in a Brabender mixer one at a time in 50g batches. The three batches prepared were neat RTM370, RTM370 with 5wt% SAP-90, and RTM370 with 0.5wt% PR-19. Prior to being added to the mixer, the composite batches were placed into a Nalgene container and shaken to initially disperse the particles into the matrix. Each 50g batch was placed into the Brabender mixer preheated to 186°C and mixed at 60RPM for 12 minutes. After mixing the samples were returned to NASA Glenn. The resulting solids were then ground in to a powder using a mortar and pestle. 1.25g of the oligomer powder was then weighed out and placed into a 1inch pellet die, which was lubricated with Mono-coat by ChemTrend. The die was then placed onto a hydraulic press preheated to 343°C (650°F) but no pressure was applied to the die. After 30 minutes the temperature of the press was raised to 380°C (680°F) and held for 5 minutes. After the five-minute hold, 120psig was applied to the die and the heat and load were held for 90 minutes. After 90 minutes, the die was removed from the press and allowed to cool before each sample was removed.

4.2.3. Aging and Other Preparation (Polishing)

Samples of each type were placed into an air-circulating oven for isothermal aging. The samples were placed into the middle area of each oven. The oven was heated to 288°C (550°F). The aging period for each sample was 1000 hours.

Following aging, the samples were cut to expose a cross-section of the sample and mounted in epoxy and polished to achieve optical smoothness. Excess epoxy mount was cut away to mount for nanoindentation using a DoAll MetalMaster band saw. Samples needing additional polishing were polished again with alumina slurry (Pace Technologies Inc.). Final washing was performed by sonication in denatured ethanol (VWR Inc.). The samples were then allowed to dry, then affixed to AFM sample discs (Ted Pella Inc.) using Loctite™ cyanoacrylate glue.

4.2.4. Measurement of Mechanical Properties

Changes in mechanical properties of the polyimide nanocomposite systems were assessed by nanoindentation. Nanoindentation has been used elsewhere for mechanical testing of polymer nanocomposites[4.11,4.16]. In this study, testing was performed using a Hysitron™ Triboscope nanoindentation transducer with a Digital Instruments™ Multimode AFM piezoelectric base. The nanoindentation probe used was a diamond Berkovich tip, which had been calibrated with fused quartz, in a manner as described in Section 2.2.

Each sample was indented using load controlled quasi-static indentations at each of two maximum loads, 5500 μN and 2750 μN. Ten indents were performed at each load, at two different zones on the sample for a total of 40 indentations per sample. The two indentation zones chosen were: the center of the sample and the edge of the sample that had

come into contact with the sample mold during the curing process. Layout of a typical sample is shown in Figure 4.2. The indents were performed using load controlled indentation with a five second loading portion to the maximum load, a five second hold at the maximum load, and a five second unloading portion. Each indent was taken a minimum of ten micrometers away from any previous indentation sites in order to avoid any influence from existing plastic deformation zones.

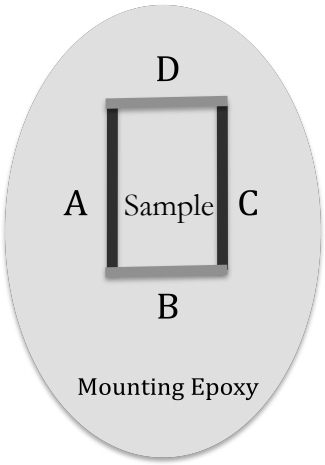

Figure 4.2: A diagram of typical sample mounting and condition. Edges A & C were in contact with the sample mold during curing and edges B & D were from cuts made after initial curing but before the aging procedure.

4.2.5. Optical Observation of Surface Degradation

In order to identify and observe the polish quality, as well as any sample nonuniformities, an optical microscope was used. Optical images of each sample were taken on an Olympus BX-60 Optical Microscope with a Scion VisiCapture digital image capture system. A polarizing filter was used on the microscope to isolate the difference between artifacts of polishing and sample irregularities. Any further image analysis and modification

was done using NIH's ImageJ, a public domain computer program for digital image modification and analysis.

4.3. Results and Discussion

4.3.1. Mechanical Properties of Unaged PMR-15 Nanocomposites

From nanoindentation of neat PMR-15 resin it can be seen that there is significant variation in the stiffness of the polyimide matrix. This can be seen in Figure 4.3 as the modulus of the neat sample measured at the sample center is 4.7±0.1 GPa and at the sample edge is 5.7±0.2 GPa. Through nanoindentation it was seen that the addition of nanoparticles to PMR-15, did not yield uniform results.

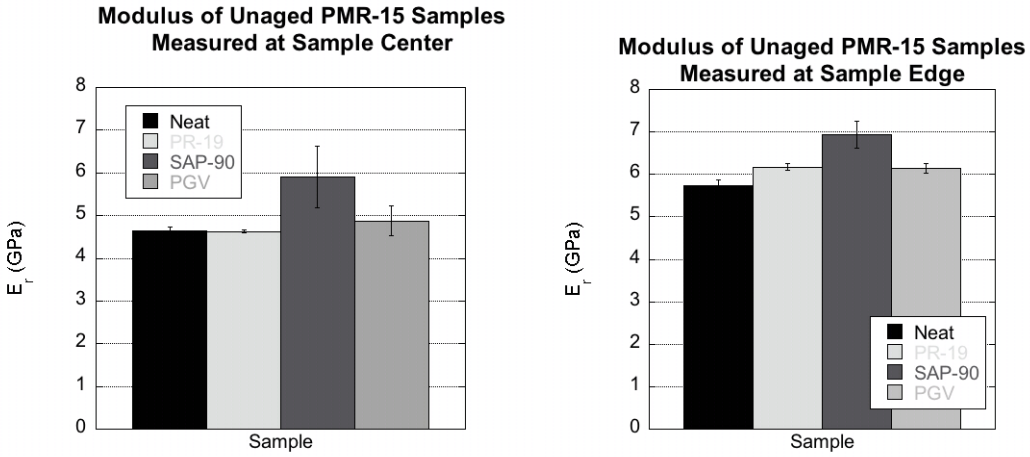

Figure 4.3: A comparison of the average reduced modulus of various unaged PMR-15 matrix nanocomposites with various nanoparticle filler materials. The synthetic SAP-90 magnesiosilicate clay nanoparticles show a distinct increase when compared with the other samples. Similar trends are seen at the sample center (left) as well as near the mold edge (right)

As can be seen in Figure 4.3 the addition of PR-19 carbon nanofibers did not yield significant changes in modulus from the neat resin. However, upon addition of SAP-90

synthetic clay a significant increase in stiffness was seen at both the sample center as well as along the mold edge. Along with the increase in average stiffness, the variance of the data also significantly increased. Thirdly, the PGV organically modified clay nanoparticles did not show a significant increase in stiffness when compared with the neat and PR-19 samples at either indentation location. However, a larger standard deviation was recorded in the PGV samples at the sample center.

4.3.2. Mechanical Properties of Aged PMR-15 Nanocomposites

Following the aging procedure, the neat, PR-19, and SAP-90 PMR-15 samples did not show a significant change is stiffness at the sample center. However, the PGV sample showed a significant increase in stiffness at the center, to 6.2±0.4 GPa, within the deviation of the SAP-90 sample, 5.9±0.2 GPa, as can be seen in Figure 4.4.

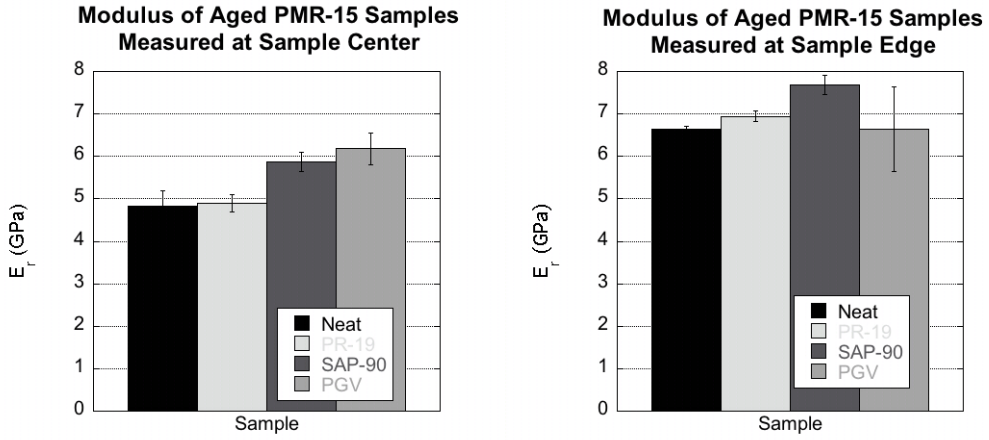

Figure 4.4: A comparison of the average reduced modulus of various PMR-15 matrix nanocomposites with various nanoparticle filler materials after 1000 hours of aging. The clay nanoparticles show a distinct increase when compared with the other samples. Trends observed at the sample center (left) are not consistent near the mold edge (right) for the PGV samples.

The edge region of the aged samples showed similar trends to those seen in the unaged PMR-15 in Figure 4.3. Upon aging, all samples show a significant increase in stiffness at the sample edge, consistent with earlier findings[4.17]. Also, the variance in stiffness of the PMR-15 sample with PGV measured at the edge region is significantly larger than variance in other samples.

4.3.3. Comparison of Different Edge Regions in PMR-15

After observing the variation of stiffness with respect to location in the PMR-15 samples shown above, additional indentations were taken. Most PMR-15 samples include two types of edges, the first are in contact with the sample die as reported on in Sections 4.3.1. and 4.3.2.; the second type of edge is along a cut during sample preparation with a diamond saw as shown in Figure 4.2. The additional indentations were taken along the cut edge as opposed to the mold edge. This was done to identify if proximity to the mold was the cause for the variation observed. In Figure 4.5 the results of the cut edge indentations can be seen.

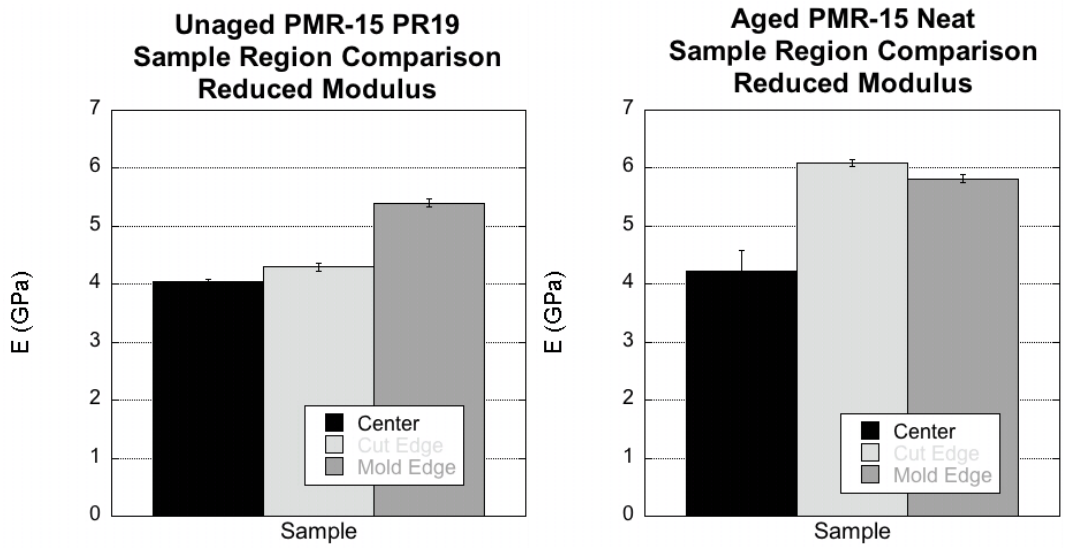

Figure 4.5: A comparison of the average reduced modulus of various locations on two different PMR-15 matrix samples. The unaged PR-19 sample (Left) shows that the cut edge is similar to the sample center. However, the aged neat (Right) sample shows that the cut edge is similar to the mold edge.

Figure 4.5 shows that the modulus of the cut edge in the unaged PR-19 sample is close to those of the sample center. Contrastingly, in the aged neat sample the modulus of the cut edge is similar to the mold edge. It is important to note that the aged samples were cut before aging so all edges would be exposed to the aging environment. Through comparing Figures 4.3, 4.4, and 4.5 it appears that initially there is an effect of the sample mold on the stiffness of the PMR-15 resin. However, the surface oxidation layer that forms during aging overcomes and surpasses the initial edge effect. The additional nanoindentation testing was only performed on the two samples shown in Figure 4.5 so to fully confirm this the other PMR-15 samples should be tested similarly.

4.3.4. Mechanical Properties of Unaged RTM-370 Nanocomposites

Unlike the PMR-15 resin, the unaged neat RTM-370 resin does not exhibit higher stiffness in the edge region, exhibiting average moduli of 4.9±0.1 and 5.0±0.0 GPa for the center and edge respectively. This relationship is also consistent in both filler materials as well. The average modulus measured for the unaged RTM-370 samples can be seen below in Figure 4.6.

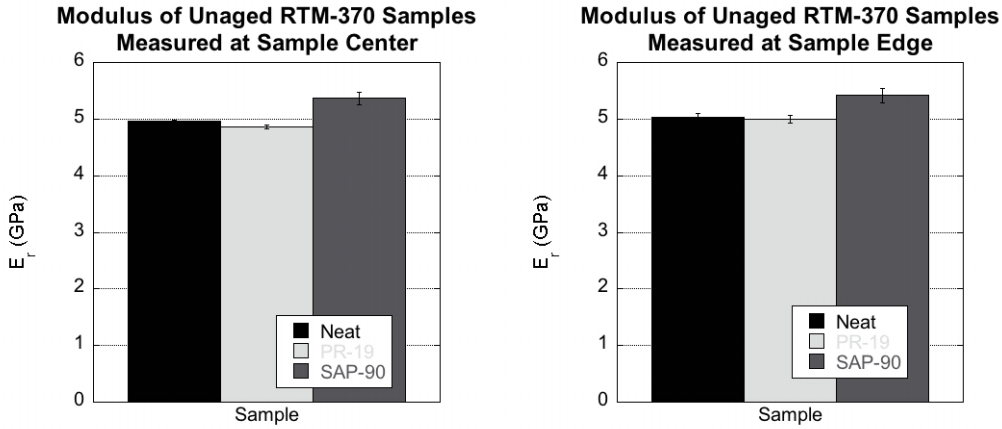

Figure 4.6: A comparison of the average reduced modulus of various unaged RTM-370 matrix nanocomposites with various nanoparticle filler materials. The synthetic SAP-90 magnesiosilicate clay nanoparticles show a distinct increase when compared with the other samples. Similar trends are seen at the sample center (left) as well as near the mold edge (right)

Akin to the PMR-15 sample, addition of 5wt% SAP-90 clay nanoparticles to the polyimide matrix yields an increase in stiffness when compared with neat resin. Similarly the addition of 0.5wt% of PR-19 carbon nanofibers does not result in a significant change in modulus of the RTM-370 matrix.

4.3.5. Mechanical Properties of Aged RTM-370 Nanocomposites

Nanoindentation results of the center and edge regions of aged RTM-370 are shown below Figure 4.7.

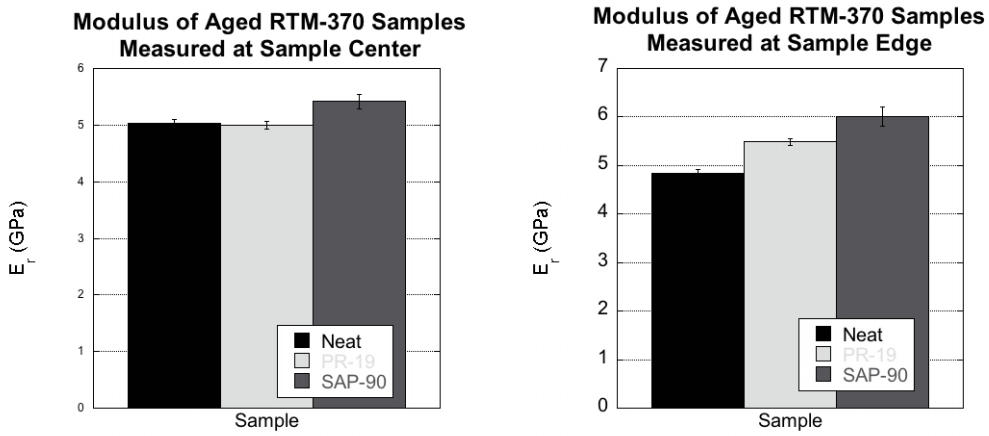

Figure 4.7: A comparison of the average reduced modulus of various RTM-370 matrix nanocomposites with various nanoparticle filler materials after 1000 hours of aging. The synthetic SAP-90 magnesiosilicate clay nanoparticles show a distinct increase when compared with the other samples. Also, the PR-19 RTM-370 sample shows a significant increase in stiffness at the edge region (Right) when compared with the center region (Left).

After the RTM-370 samples were subjected to the aging procedure, no effect was seen in the center of the sample, as seen in Figure 4.7. For example, the unaged modulus of neat RTM-370 is 4.93±0.10 GPa after aging it was measured to be 5.04±0.07 GPa. Aging of the PR-19 and SAP-90 RTM-370 samples resulted in higher stiffness at the edge regions of both samples. With respect to addition of nanoparticles to polyimide matrix elastic modulus, the RTM-370 results are consistent with those observed in PMR-15, with the exception of the pronounced mold effect seen in PMR-15.

4.3.6. Optical Observation of Surface Degradation

Representative optical images of neat PMR-15 and PMR-15 with SAP-90 clay nanoparticles can be found in Figures 4.8 and 4.9 respectively. Similarly, images of RTM-370 and RTM-370 with SAP-90 clay nanoparticles can be seen in Figures 4.10 and 4.11.

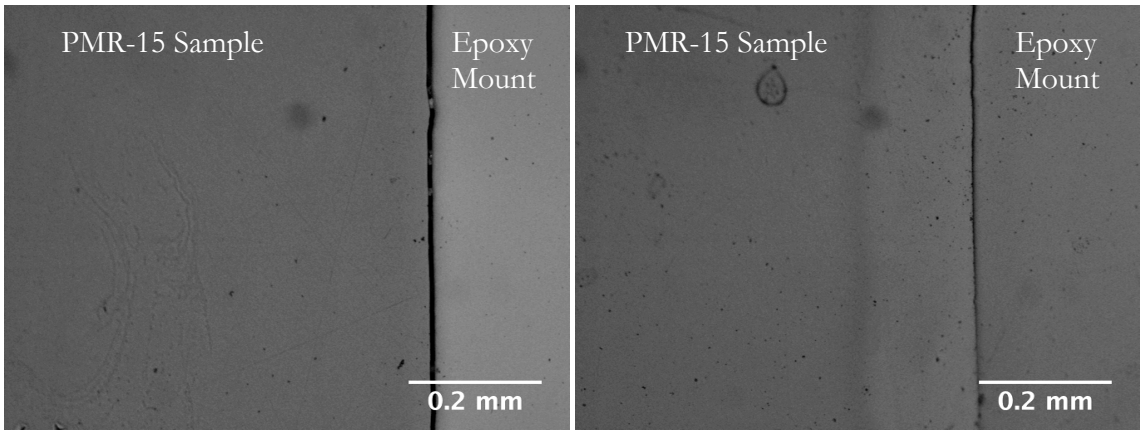

Figure 4.8: Optical images of the polished surfaces of unaged (Left) and aged (Right) neat PMR-15. The edge shown in both images was in contact with the sample mold during processing. Note the change in shade along the edge of the sample the significantly grows during aging.

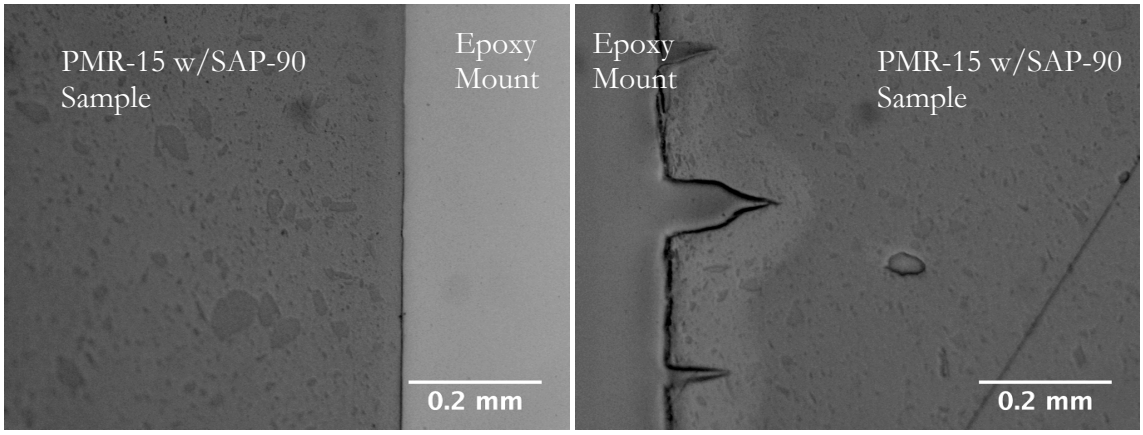

Figure 4.9: Optical images of the polished surfaces of unaged (Left) and aged (Right) PMR-15 with SAP-90 clay nanoparticles. The edge shown in both images was in contact with the sample mold during processing. Note the change in shade along the edge of the sample the significantly grows during aging. The oxidation region also follows the profile of the crack (Left).

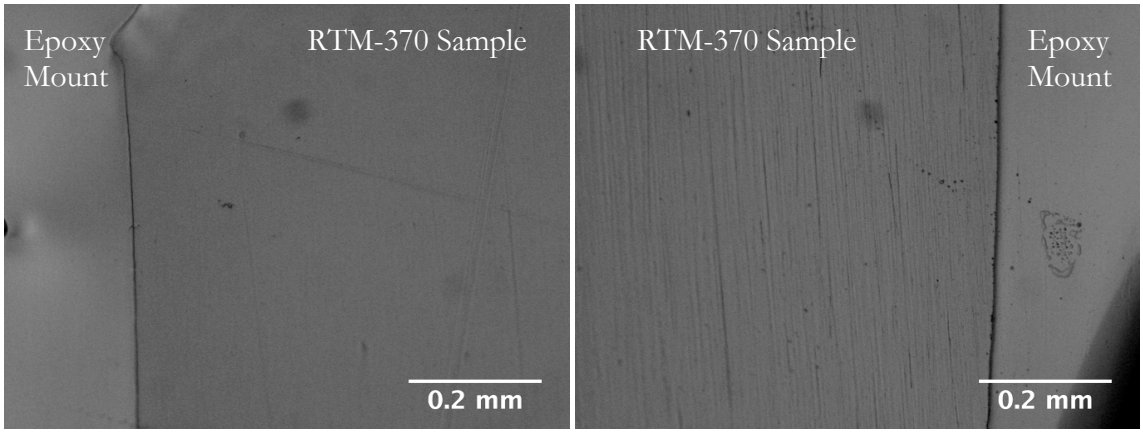

Figure 4.10: Optical images of the surfaces of unaged (Left) and aged (Right) neat RTM-370. The edge shown in both images was in contact with the sample mold during processing. Note the absence of significant change in shade along the edge of the sample.

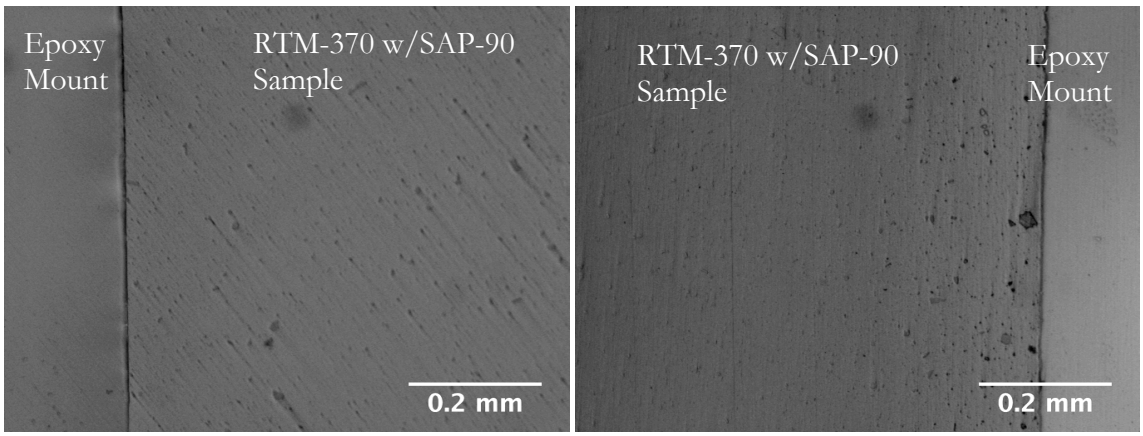

Figure 4.11: Optical images of the surfaces of unaged (Left) and aged (Right) RTM-370 with SAP-90 clay nanoparticles. The edge shown in both images was in contact with the sample mold during processing. Note the absence of significant change in shade along the edge of the sample. Also note, the development of voids along the surface in the aged sample

Observation of PMR-15 confirms the presence of a mold-related surface effect as can be seen in Figures 4.8 and 4.9. When compared with the mold surface of the RTM-370

samples, it is clear the surface oxidation of PMR-15 occurs much more readily than RTM-370 as can be seen in Figures 4.10 and 4.11. Some effects of aging can be seen along the edge of the RTM-370 with SAP-90 clay in Figure 4.11 but it is not as severe as the extensive surface cracking seen in Figure 4.9. Overall, the features observed under microscopy confirm the results and conclusions shown from nanoindentation. Additional optical images can be found in Appendix D.

4.3.7. Additional Discussion on Nanoparticle Filler Materials

Although both PGV and SAP-90 are by definition clay nanoparticles they are structurally dissimilar. Natural clay nanoparticles are typically plate-like and contain strong ionic charges with opposite charges on the face and edge respectively[4.19]. This ionic charge can lead to agglomeration due to ionic attraction. In order to avoid this attraction the SAP-90 nanoparticles, supplied by Claytec Inc., were synthesized with magnesium substituted in place of some of the silicate bonding sites on the surface of the particles[4.19]. This substitution yields clay nanoparticles that remain polar but are also electronically neutral[4.19]. This is done through a proprietary production method patented by Claytec[4.19].

Figure 4.12 shows SEM images of PR-19 nanofibers and distribution of PR-19 in aged PMR-15. A TEM image of SAP-90 clay nanoparticles and SEM image of distribution of SAP-90 in aged PMR-15 are included in Figure 4.13. The SEM image presented in Figure 4.14 shows distribution of PGV clay nanoparticles in the aged PMR-15 matrix.

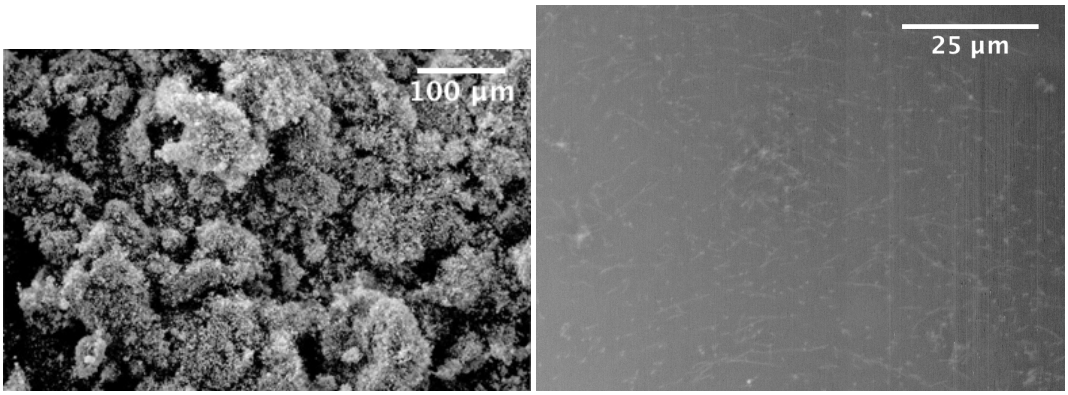

Figure 4.12: SEM Image of PR-19 CNF particles[4.20] (Left). SEM image showing distribution of PR-19 in aged PMR-15 (Right).

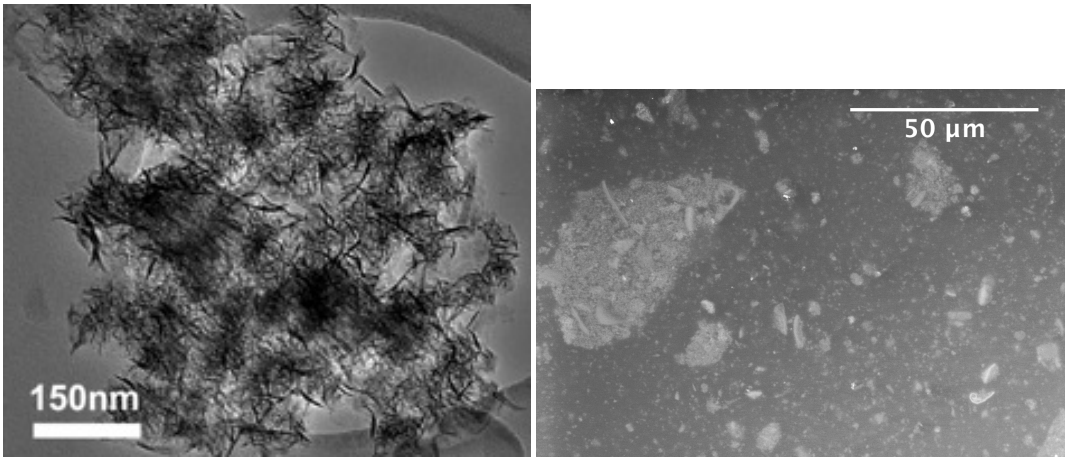

Figure 4.13: TEM image of SAP-90 clay particles[4.19] (Left). SEM image showing distribution of SAP-90 in aged PMR-15 (Right).

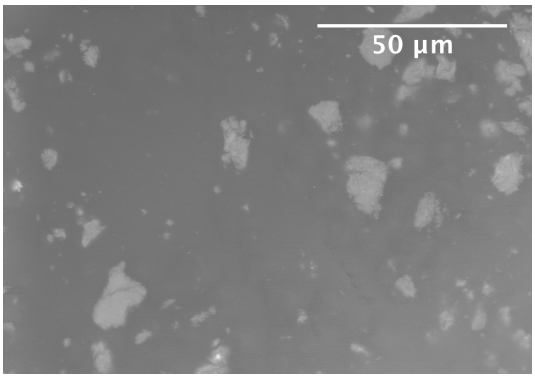

Figure 4.14: SEM image showing distribution of PGV clay particles in aged PMR-15.

Overall large agglomerate size in PGV and SAP-90 samples are similar but the PGV containing samples did not have smaller particles dispersed through the PMR-15 matrix. The larger variance of mechanical properties measured in PMR-15 samples with PGV and SAP-90 are believed to be caused by agglomeration observed in Figures 4.13 and 4.14.

4.3.8. Additional Testing at NASA Glenn Research Center

In addition to the nanoindentation testing and optical microscopy performed at Clemson, supplemental testing was performed on the polyimide nanocomposite systems by our collaborators at NASA Glenn Research Center. Dynamic mechanical analysis (DMA), Fourier transform infrared spectroscopy (FTIR), and weight loss measurements were collected at NASA Glenn research center. DMA testing revealed that the glass transition temperature of RTM370 was not affected through the incorporation of nanoparticles to the polyimide matrix. The FTIR testing showed similar behavior in all of the aged samples, showing that there is little structural difference of the RTM-370 with or without nanoparticle inclusion. Also, in both the RTM-370 and PMR-15 systems the SAP-90 particles caused a higher weight loss during aging than the NEAT samples, which is undesirable.

4.4. Conclusion

Through nanoindentation and optical microscopy it can be clearly seen that PMR-15 develops a surface layer upon aging, as reported elsewhere[4.17]. Contrastingly, RTM-370 is not susceptible to similar aging behavior for the same conditions. Even though the two resins are both polyimides they still have very different structures.

When nanoparticles are incorporated into the polyimide matrices two different results were seen. With the PR-19 carbon nanofiber, little to no effect in the mechanical properties was seen. However when SAP-90 clay nanoparticles were added, significant increases in the modulus were consistently measured. Due to the different densities of the particulate, differing weight percents were added to yield similar volume fractions of filler. The particles are dissimilar in chemistry, shape, and most importantly surface area. According to manufacturer's specifications the PR-19 fibers have a surface area of 15-25m^2/g and the SAP-90 clay has a surface area of 400-700m^2/g. Traditional composite theories do not include surface area in their calculations, but current research has shown surface area to be an important factor[4.1,4.2].

CHAPTER FIVE

SUMMARY AND FUTURE WORK

5.1. Summary

Both of the systems examined in this study (metallic nanolaminate films and polyimide matrix nanocomposites) have potential applications in high temperature environments. This study showed through the interpretation of accelerated aging tests that aging impacts the mechanical response of both systems. Nanoindentation of aged metallic nanolaminates revealed significant softening in the thinner, 20 nm, layers of both the Cu/Nb and the Ti/W systems. It is noted that this was seen irrespective of the heat treatment atmosphere. It has been proposed that the softening threshold is caused by a phase stability, which no longer occurs at reduced layer thicknesses[5.1]. It was observed in this study that softening occurred at lower temperatures than seen elsewhere[5.1]. Residual stress appears to be the largest factor that separates this study from the prominent literature[5.1,5.2].

The elastic modulus of aged polyimide matrix nanocomposites was measured using nanoindentation. It was observed that the PMR-15 resin showed the developed a significant oxidation region along the exposed surfaces during aging. However, the RTM-370 did not develop similar surface regions on aging. The addition of different nanoparticle filler materials in similar volume fractions did not yield similar results. It is hypothesized that this is due to the difference in surface area for different nanoparticle filler materials.

5.2. Future Work

It was seen in Chapter Three that for 20 nm layer thickness Cu/Nb and Ti/W multilayers, significant decreases in hardness were observed after heating to 400°C for 30

minutes. The softening seen in this study was observed at lower temperatures than seen elsewhere[5.1]. It has been hypothesized that the cause for this lower softening temperature is due to the stress constraints imposed on the nanolaminate during heat treatment, as the film was subjected to heating while still attached to the substrate. Whereas, the conflicting study had peeled the films away from the substrate prior to heating[5.1]. Research has shown that changing the nature of physical constraint on a film during heat treatment greatly affects the residual stress development[5.2]. Methods to further explore this and future directions for nanolaminate research are discussed below.

5.2.1. Influence of Stress

XRD has been used to show orientations of films and to ensure that no intermetallic phases have been formed; XRD can also be used to locally measure residual stress using the $\sin^2\psi$ method[5.3-5]. Incorporating this testing technique allows for a direct measurement of stress as opposed to the estimation made from substrate curvature measurements and Stoney's equation. Also, an XRD system with a heated sample stage could be utilized to measure residual stress while at elevated temperature. Direct analysis of stress is essential to validate the hypothesis of the lower softening temperatures observed.

5.2.2. Other In-Situ Techniques

In addition to heated stage XRD, other analysis techniques exist with environmental controls as well. Two such techniques that have been considered are nanoindentation and TEM at elevated temperatures. Elevated temperature nanoindentation could allow for measurement of nanolaminate hardness during accelerated aging to further examine the time and temperature effects of softening. Similarly, elevated temperature TEM would allow for

the observation of interfaces during the accelerated aging process with the possibility to observe diffusion and interfacial stability.

5.2.3. Examining Interfacial Spreading

The strength of nanolaminates is dependent on the ability of interfaces to restrict dislocation motion through the system. When these layer interfaces are geometrically unstable then diffusion promotes interdiffusion and interfacial spreading[5.1]. Methods such as Auger Electron Spectroscopy (AES) could be used to measure the degree of spreading that has occurred by measuring elemental composition as a function of depth through the nanolaminate. Also TEM has been used elsewhere for direct observation of interfaces and has the resolution necessary for observing the size scale of nanolaminates[5.1,5.6]. Observing microstructures, interfaces, and grain size is possible with the SEM techniques shown, but it is not ideal. For the length scales of interest, higher resolution is necessary, which is possible through TEM and FIB. In addition, XRD could also be used to measuring deviations in lattice spacing that could be caused by interdiffusion of the layers into one another.

5.2.4. Installation of Additional Instrumentation to the Sputter Deposition System

Not only are additional analysis techniques being considered; it has been determined that additional monitoring equipment could prove useful for the sputtering system. Substrate temperature during deposition is known to affect the resulting film microstructure[5.7]. In order to better understand the initial films being produced, direct measurement and control of substrate temperature has been suggested. This may be accomplished through the installation of a sample platen that contains heaters and thermocouples. Similarly, direct measurement of the remaining gases present inside the chamber during deposition through the installation of a residual gas analyzer is desired. A

residual gas analyzer measures the atmosphere content of light elements inside the sputter chamber during deposition. Also, a crystal growth monitor is being considered to measure the deposition rate in-situ for more precise control of layer thickness during sample fabrication. These additions to the sputtering system could add additional insight and control of the initial conditions of the film systems.

APPENDICES

APPENDIX A

EXPANDED INSTRUCTIONS FOR OPERATION OF CLEMSON COMSET KURT J. LESKER SPUTTER DEPOSITION SYSTEM IN AMRL LAB 16

A.1. Components of the Kurt J. Lesker Sputtering System in AMRL Lab 16

The sputtering system at AMRL was refurbished through a grant from COMSET. This unit was retrofitted to sputter with a custom wafer platen that accommodates four 3" silicon wafers and a second power source for deposition was added. The system has two magnetrons, each with a separate power supply to provide the ability to individually sputter two distinct materials or co-sputter a multi-component film. The vacuum consists of two pumps, a mechanical roughing pump for initial pumping and a Cryo-Torr Cryo-Pump for high vacuum pumping. Vacuum measurement is performed by a Granville-Phillips vacuum gauge and ion gauge calibrated to N_2 and an MKS Baratron calibrated to Ar. The original power supply is an Advanced Energy RFX-600 RF power supply with an ATX-600 tuner. The newly installed power supply is an Advanced Energy MDX-500 DC power supply.

A.2. Layout of Sputtering System

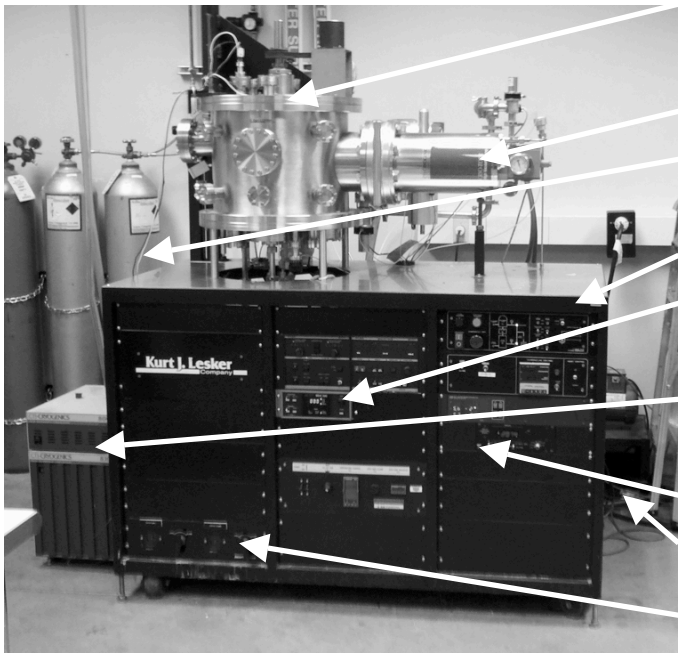

A. Sputter Chamber

B. Cryo-Pump

C. Argon Tanks

D. Control Panel

E. Power Supplies

F. Cryo-Pump Compressor & Controller

G. Vacuum Gauges

H. Mechanical Pump

I. Water Indicators

Figure A.1: Overall Layout of Sputter Deposition System. Mechanical roughing pump is located behind the right side of the machine. Process gas valves are located behind the right side of the machine

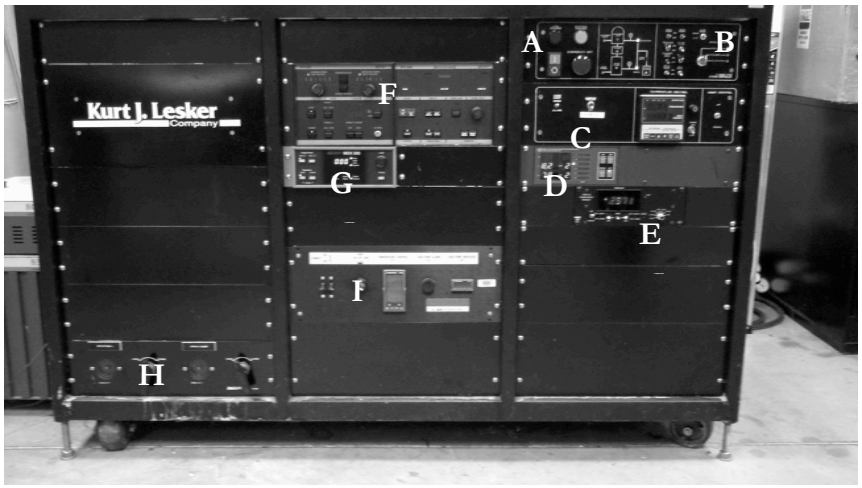

Figure A.2: Layout of Sputter Deposition Contol Panel. A) Main Power Control, B) Process Gas Valve Controls, C) Conductance Controller Valve and Stepper Motor, D) Vacuum Gauge, E) Baratron, F) RF Power Supply, G) DC Power Supply, H) Coolant Water Flow Indicators, I) Substrate Heater Controller (Not Used)

A.3. Sputtering Procedure

I. Shut-down / Start-up valve and switch position

Check if:

1. All valves on panel should be in OFF position (all valves should be closed), except the conductance controller "COND CONT" should be on OPEN
2. All rack power switches in OFF position
    a. Power supply of Baratron (MKS) *(E in Figure A.2)*
    b. Vacuum gauge controller (Granville Phillips) *(D in Figure A.2)*
    c. ATX-600, RFX-600 (Advanced Energy) *(F in Figure A.2)*
    d. MDX-500 (Advanced Energy) *(G in Figure A.2)*
    e. Substrate Heater Controller (AJA International) *(I in Figure A.2)*
3. Process gas valves (Needle and Toggle valves) under chamber should be closed
4. Water turned off
5. Nitrogen supply turned off
6. All gas bottle valves closed

II. Initial Start-Up

1. Verify valve and switch position as indicated in Section I
2. Check oil level of mechanical pump
3. Check gas bottle pressure (UHP Ar, UHP O_2, UHP = Ultra High Purity grade = 99.999%, O_2 is typically not used and absent)
4. Open compressed air for solenoid valves and set regulator to 80 psi (never turn off during operation of the unit because all valves are pneumatic type valves)
5. Turn key to MANUAL position
6. Press GREEN power button (red (cryo fail) and orange (manual) lights should illuminate)
7. Turn on the mechanical pump (found behind the sputtering unit itself)
8. Turn on the Vacuum Gauge controller (Granville-Phillips)
9. Turn on system water (system water is used for cooling Cryo-pump as well as magnetron guns)
10. Check if both cooling water valves are open and spinning (bottom left of unit)
11. Set ROUGHING VALVE to on
12. Leave system under roughing and let equalize for a long time

III. Start-up of CRYO-PUMP

1. Open gas valve of N_2 and set the regulator to <5 psi
2. Ensure compressed air is still on and set at 80 psi
3. Make sure the compressor and Cryo pump controller are on
4. Set MECH PUMP switch to ON

5. Open CRYO PURGE VALVE (ON) Cryo-pump will be purged with nitrogen (Nitrogen should be flowing out of valve on bottom of Cryo-pump)
6. Purge pump for 5 minutes
7. Close CRYO PURGE VALVE (OFF)
8. Open REGEN VALVE (ON)
9. Pump Cryo-pump chamber down to 100 mtorr (1.0×10^{-1} torr) (Gauge B of Granville-Phillips)
10. Close REGEN VALVE (OFF)
11. Repeat 5 or so times (~1 hr)
12. Wait 5 minutes then reopen REGEN VALVE. If the pressure rises above 150 mtorr, repeat step 11 again.
13. Close REGEN VALVE
14. Start Cryo-Pump (Turn CRYO-PUMP switch on)
15. Let Cryo-Pump operate for a few hours (Cryo-pump will operate at/below 15K when fully cooled)

IV. Sample Loading

1. Turn on MKS power supply (unit takes a couple hours to warm up before proper readings)
2. Wash substrates with acetone, isopropyl alcohol, DI water, acetone, isopropyl alcohol, and DI water in a stepwise manner
3. Dry substrates using hot plate @100°C for 5 minutes
4. Let substrates cool
5. Place substrates into plasma cleaner and clean for 5 minutes
6. Make sure ALL valves are closed (OFF) except the conductance controller "COND CONT" should be OPEN
7. Ensure Nitrogen (<5psi) is turned on
8. Ensure compressed air (80psi) and water are on
9. Turn off ROUGHING VALVE
10. Turn off MECH PUMP
11. Set CHAMBER VENT VALVE to ON
12. Vent chamber (may take up to a few minutes)
13. Upon reaching ATM pressure green CHAMBER ATM light will illuminate
14. Set CHAMBER VENT VALVE to OFF
15. Turn off Nitrogen
16. Raise chamber lid with HOIST CONTROL in UP position
17. Attach sample to sample holder (use latex gloves to avoid chamber contamination)
18. Carefully lower lid with HOIST CONTROL in DOWN position. Assist chamber alignment as lid comes down
19. Set MECH PUMP to ON
20. Set ROUGHING VALVE to ON
21. Pump down chamber to 50 mtorr (5.0×10^{-2} torr) (Gauge A of Granville-Phillips) *May take upwards of a half hour*
22. After reaching below 50 mtorr, set ROUGHING VALVE to OFF
23. Monitor pressure for 5 minutes

i. If pressure rise is greater than 10 mtorr/minute then search for the problem and pump down to 50 mtorr again and monitor for another 5 minutes
ii. If pressure rise is less than 10 mtorr/minute, pump down to below 50 mtorr and proceed

V. Sputtering

1. Ensure baratron (MKS) has been turned on, takes a while to warm up
2. Make sure ROUGHING VALVE is set to OFF
3. Set HI-VAC VALVE to ON (A loud pressure relief sound will be heard)
4. Wait until gauge A on Granville-Phillips reads "O"
5. Press the IG1 button on the Granville-Phillips controller to turn on the Ion gauge
    i. Do not turn Ion gauge on at pressure values above 10^{-4} torr
    ii. Make sure Ion gauge is illuminated (glass apparatus on left hand side of vacuum chamber) If not, Ion gauge must be replaced
6. Ramp down to desired pressure (minimum required pressure for starting plasma ~ 1 x 10^{-6} torr)
7. When desired pressure is reached, press IG1 to turn off the ion gauge
8. Set Cond Cont to close
9. Turn on argon supply tanks and set regulator to a reasonable value (10-15psi)
10. Open toggle valve for process gas (argon)
11. Open needle valve until desired process pressure is shown on Baratron (MKS)
12. Once process pressure has been set, turn on power supply (either RF or DC) and set wattage to desired value, switch power supplies to ON/START ensure plasma, interlock, and all other lights remain illuminated after power supply has been activated (RF power supply requires RF tuner to be on as well)
13. Ensure plasma has been ignited by visual inspection
14. After plasma has been ignited, clean target by pre-sputtering with cover closed for a couple minutes
15. Open shutter and turn on stepper motor to rotate sample platen
16. Verify settings have not drifted and parameters have been copied to log book
17. Sputter for desired time
18. Close shutter, stop power supply
19. If multilayer samples are being sputtered, deposit remaining layers in similar manner
20. Turn off RF power supply, Stop DC power supply, ensure power level of both are set to 0
21. Close needle and toggle valves for argon
22. Set Cond Cont to open
23. Close HI-VAC Valve
24. Vent chamber
25. Open chamber and remove samples, if sputtering is finished remove targets from magnetrons

26. Close chamber
27. Turn on roughing pump
28. If sputtering again: Repeat pump down and leak test procedure (Part IV steps 18-22) and then all of Part V
29. If not, begin shut down procedure

VI. Shut down of system

1. Turn off both DC and RF power supplies
    i. Ensure both are set to off/stop and that power level is set to 0
    ii. Physically turn off both RF power supply and tuner
2. Turn off Baratron (MKS)
3. Turn off cryopump
4. Turn off water
5. Shut off both argon tanks
6. Ensure chamber is pumped down to 50mtorr via roughing pump
7. Shut all valves
8. Turn off nitrogen
9. Turn off mechanical pump
10. Turn off system by pressing red power button
11. Turn key to standby

APPENDIX B

CALIBRATION AND TROUBLESHOOTING OF QUASI-STATIC AND DYNAMIC HYSITRON TRIBOSCOPE NANOINDENTATION

B.1. Comparision of Quasi-Static and Dynamic Nanoindentation

There are two main types of nanoindentation methods: quasi-static and dynamic. Up to this point quasi-static has been the only method to be discussed. By definition quasi-static indentation is a loading technique that uses a constant loading rate. Dynamic indentation however uses a dynamic loading pattern to obtain additional information from testing. Different nanoindenter manufacturers have different trade names for their dynamic systems. For example the continuous stiffness method (CSM) is available on Agilent systems and nanoDMA is available on Hysitron systems.

For dynamic indentation, a sine wave is overlaid on a static loading function, as shown in Figure B.1. The sinusoidal load allows for stiffness to be measured at each of the incremental unloading portions of the test. In addition to testing viscoeleastic materials, dynamic nanoindentation can extract results from a series of depths at one location in a short period of time.

Viscoeleastic materials show both elastic and viscous response to external loading, meaning that their strain response is time dependant. This means that unlike elastic materials, which instantaneously respond, these materials will have both a storage and loss modulus with the loss modulus representing the viscous nature of the material. Research has shown that there is considerable time dependence in nanoindentation of viscoelastic materials[B.1].

Both indentation test techniques should yield the same mechanical properties. However, some reports show that these values are not entirely consistent; values obtained from dynamic loading depend on the frequency and amplitude of the sinusoidal portion of the loading function[B.2]. Deviations seen in dynamic indentation results are especially pronounced at reduced depths and in softer materials[B.2].

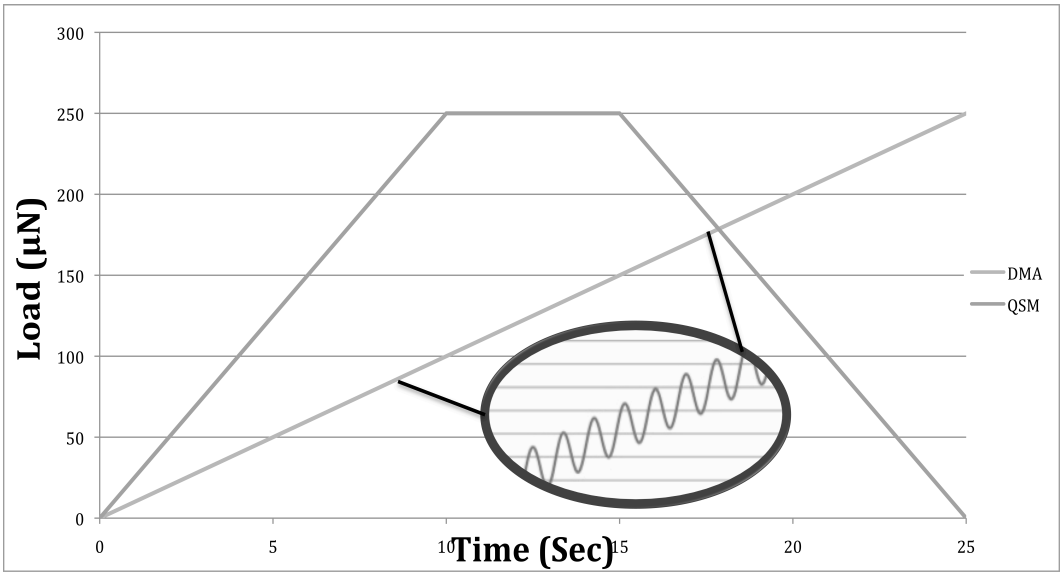

Figure B.1: A diagram showing the difference between traditional quasi-static loading and sinusoidal nanoDMA loading during typical nanoindentation testing.

B.2. Nanoindentation System at Clemson University

The system used in this work is a Hysitron™ Triboscope nanoDMA nanoindentation transducer with a Digital Instruments™ Multimode AFM piezoelectric base for sample motion. The nanoDMA option adds a Stanford Research Systems™ digital signal processor along with additional National Instruments data acquisition hardware and a nanoDMA module provided by Hysitron™. The system allows the user to control amplitude and frequency in the sinusoidal load function, as well as traditional parameters such as maximum load and duration. Overall setup for the entire nanoDMA system is

shown in Figure B.2. This system has two transducers an older quasi-static transducer (QSM) that is for quasi-static indentation only and a newer dynamic transducer (DMA) that is capable of both quasi-static and dynamic indentation modes.

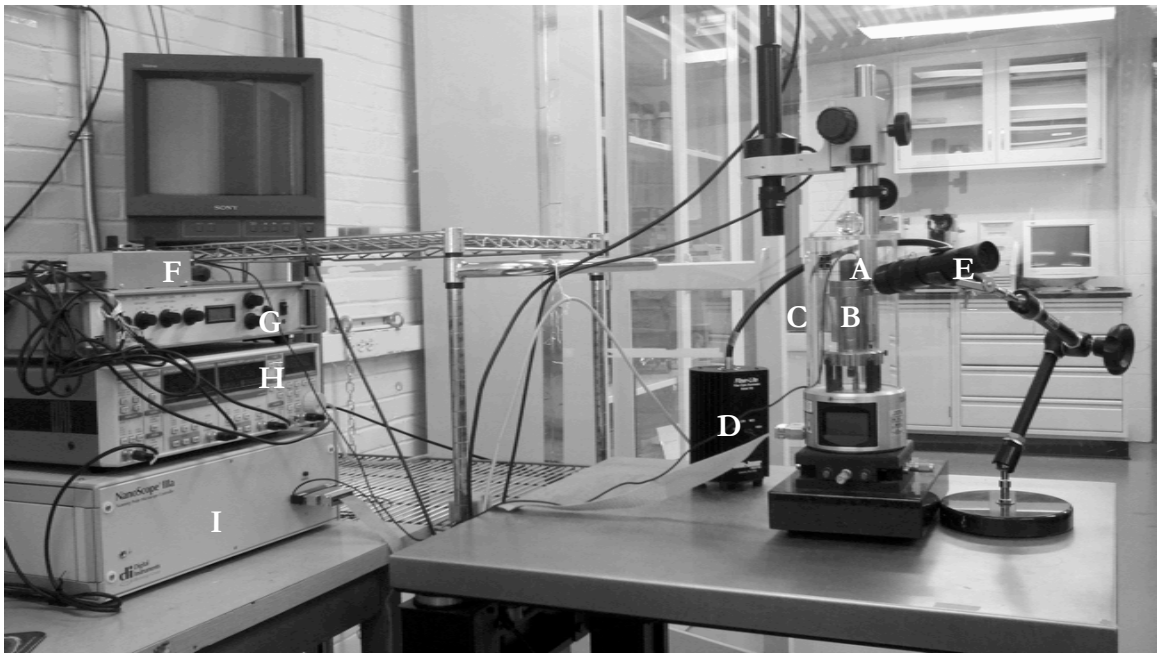

Figure B.2: Layout of Hysitron™ Triboscope nanoDMA system. A) Hysitron Nanoindentation Transducer, B) Digital Instruments™ AFM Piezoelectric Base, C) Anti-Vibration Cover, D) Light Source, E) Magnifying Lens, F) Hysitron™ nanoDMA module, G) Hysitron™ Nanoindentation Controller, H) Stanford Research Systems™ Lock-In Amplifier, I) Digital Instruments™ AFM Controller

B.3. Calibration of Dynamic Nanoindentation Transducer for Quasi-Static and Dynamic Indentation

Calibration of nanoindentation systems is of extreme importance. Section 3.3. outlined some of the steps necessary for tip area calibration using quasi-static indentations. In addition to tip area, it is essential to account for physical compliance of the indentation system itself. Machine compliance is a calibration value that the Hysitron™ software uses to accommodate for deformation of the system and not the sample being tested. Machine compliance calibration is further described in the following section.

B.3.1. Initial Testing – Determining Compliance of DMA and QSM Systems

Two separate nanoindentation transducers were calibrated- a quasi-static (QSM) transducer and the dynamic (DSM) transducer. Each transducer was used in the quasi-static mode and indentations were performed on a fused quartz standard (E=69.6 GPa), which was provided with the system. All indents performed were made using load controlled indentation mode over a range of maximum loads in a three-step load function similar to what is seen in Figure B.1. These indentations included a five second loading segment to the maximum load, three second hold at the maximum load, followed by a five second unloading segment to no load.

As a result of this, a calibration of the machine compliance was performed. In order to calibrate for machine compliance ten to fifteen indents should be taken at loads close to the maximum load of the transducer. Following analysis a line is then fit through the data when compliance (stiffness^{-1}) is plotted as a function of $\text{maximum load}^{-1/2}$. Exact instructions for this and other calibrations can be found in the Hysitron User's Manual[B.3]. Upon changing this value from 2.0 nm/mN to 0.4 nm/mN for the nanoDMA transducer, the results in Figure B.3 were obtained. The QSM transducer's machine compliance value remained constant at 1.0nm/mN.

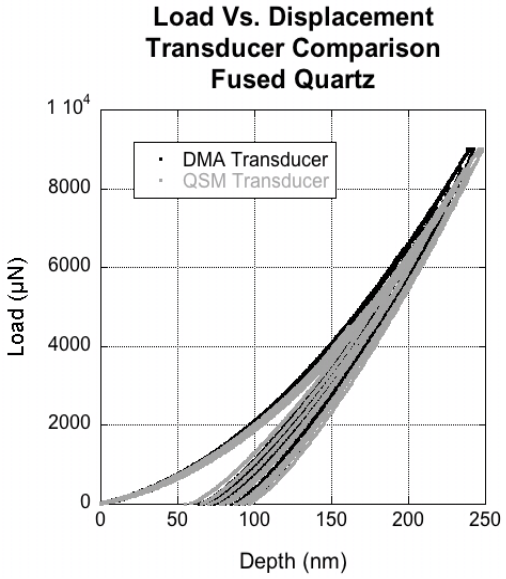

Figure B.3: Comparison of load vs. displacement plots of the two different nanoindentation transducers following modification of the machine compliance value of the nanoDMA transducer. Sample used is fused quartz standard.

Up to this point only quasi-static indents were performed. As is seen in Figure B.4 the nanoDMA transducer yielded superior results when compared to the older QSM transducer. Following the values seen in Figure B.3 and B.4 it was determined that the transducers were in agreement for quasi-static measurement.

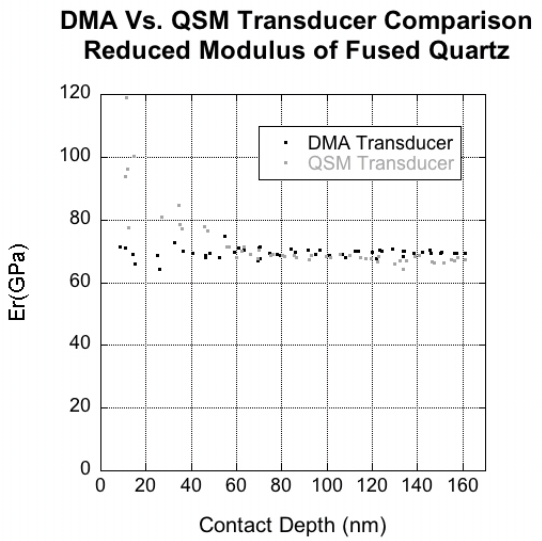

Figure B.4: Comparison of reduced modulus of the two different nanoindentation transducers following modification of the machine compliance value of the nanoDMA transducer. Sample used is fused quartz standard

B.3.2. Effect of Load Amplitude on nanoDMA Results

Initial nanoDMA indents performed were made using variable dynamic load indentation mode similar to what is seen in Figure B.1. The parameters used for the DMA indentations were beginning quasi-static load: 500 μN, ending quasi-static load: 5100 μN, frequency: 45 Hz, 80 cycles, 15 steps, with a loading rate of 100 μN/sec. The total test time for this load function is one minute and 20 seconds. Also, two different load amplitudes were used 10 and 20 μN. The results are shown in Figure B.5.

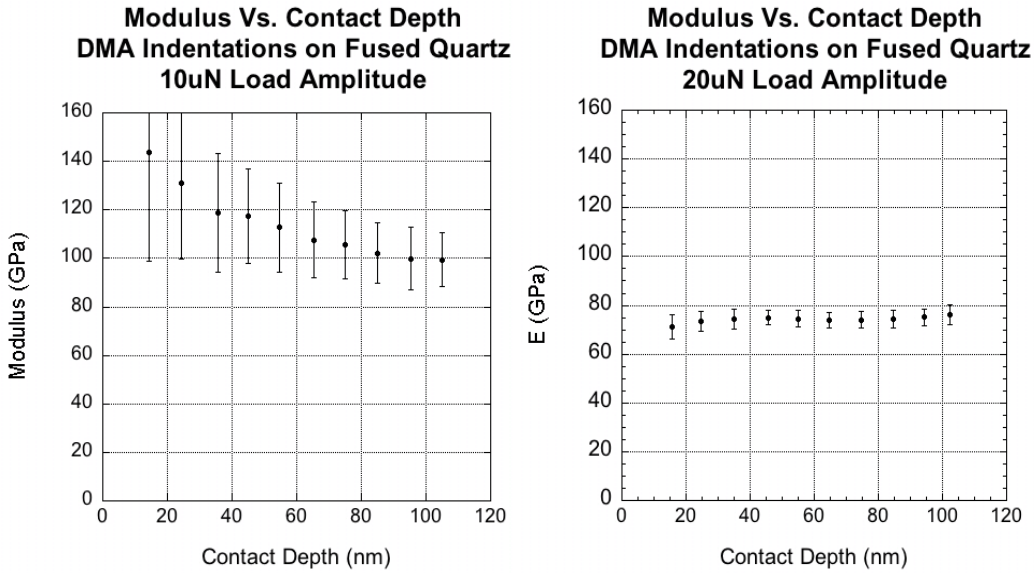

Figure B.5: Initial nanoDMA indentation results, modulus as a function of contact depth for 10 μN (left) and 20 (right) μN load amplitude. Indents taken on fused quartz calibration standard.

The results seen in Figure B.5 show an undesirable trend, large deviation and incorrect values for a homogeneous fused quartz sample when tested with a load amplitude of 10 μN. During both tests a displacement amplitude of between one to two nanometers was maintained as the operation manual suggests[B.3]. Based on conclusions found in Cordill et al. this can be somewhat expected, although the deviations seen in Figure B.5 are much larger than those identified elsewhere[B.2]. More testing to further clarify the effect of load amplitude on nanoDMA results is desired.

B.3.3. Effect of Frequency on nanoDMA Results

Similar to load amplitude, the effects of load function frequency and amplitude must be understood in order to obtain valid data from unknown samples. In order to monitor the effect of frequency on dynamic test results, a specialized loading function was supplied by Hysitron™ to perform random frequency sweeps at prescribed loads. Figure B.7 shows the

variable frequency loading function and Figure B.8 shows results of the variable frequency indentations.

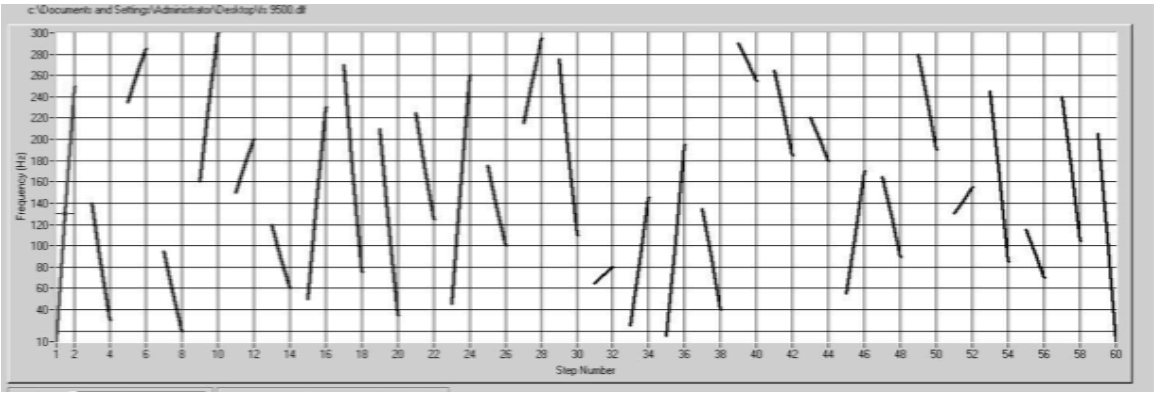

Figure B.6: Diagnostic variable frequency nanoDMA load function supplied by Hysitron. Chart shows frequency as a function of step number. Indents were performed at 6000, and 9500 μN each, all on a fused quartz calibration standard. Image taken as screenshot of Hysitron Triboscope software.

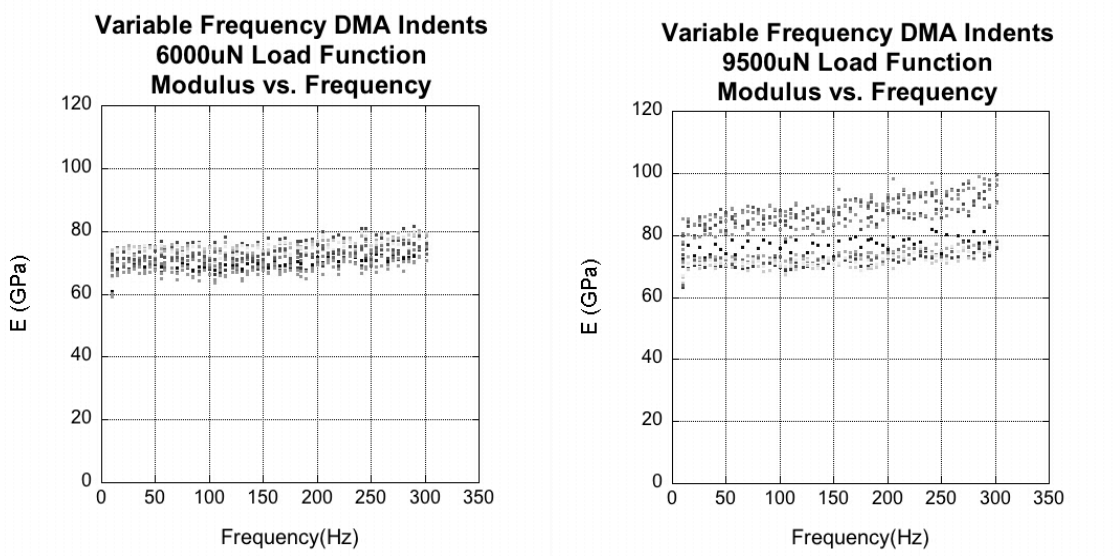

Figure B.7: Variable frequency nanoDMA indentation results showing elastic modulus as a function of frequency. Indents were performed at 6000 μN (left), and 9500 μN (right) all on a fused quartz calibration standard.

As a result of the variable frequency testing, no trends could be seen. It was determined that there was no effect of frequency when using the nanoDMA mode on a rigid sample such as fused quartz. It is possible that the frequency sweep loading function shown in Figure B.6 could be used on viscoelastic materials in order to identify resonant frequencies.

B.3.4. Proper Cleaning Procedures

Alongside the testing described above, procedures for more rigorous tip and sample cleaning were discussed and verified. The more rigorous cleaning procedures should account for higher precision in nanoindentation results. Previously, the nanoindentation probe was cleaned using a polystyrene "packing peanut" but it was discovered that this might cause static charging of the tip, which is undesirable. Currently the method used for tip cleaning is to "fluff" a cotton swab using tweezers and using acetone to swab the tip in a vertical motion from the base to the tip of the probe. Also, swabbing of the sample is helpful; however, the solvent used depends on the material being cleaned. As samples are generally affixed to AFM pucks using cyanoacrylate glue, acetone should be avoided; ethanol is a good choice for most samples.

APPENDIX C

ADDITIONAL SEM IMAGES OF AGED NANOLAMINATE SAMPLES

Only selected cross-section SEM images captured of the nanolaminate samples were included in the body of this thesis. This was done to help the reader focus on the main points of this research. However, the remaining images of the aged nanolaminates have been collected into this appendix for the readers. For these images to be taken the silicon substrate was cleaved and the fracture surface was viewed. A specialized thin film cross-section sample holder from Ted Pella Inc. made additional sample preparation unnecessary.

All of the images presented in this appendix were obtained in accordance with the methods described earlier in Section 3.2.4.

C.2. Additional Images

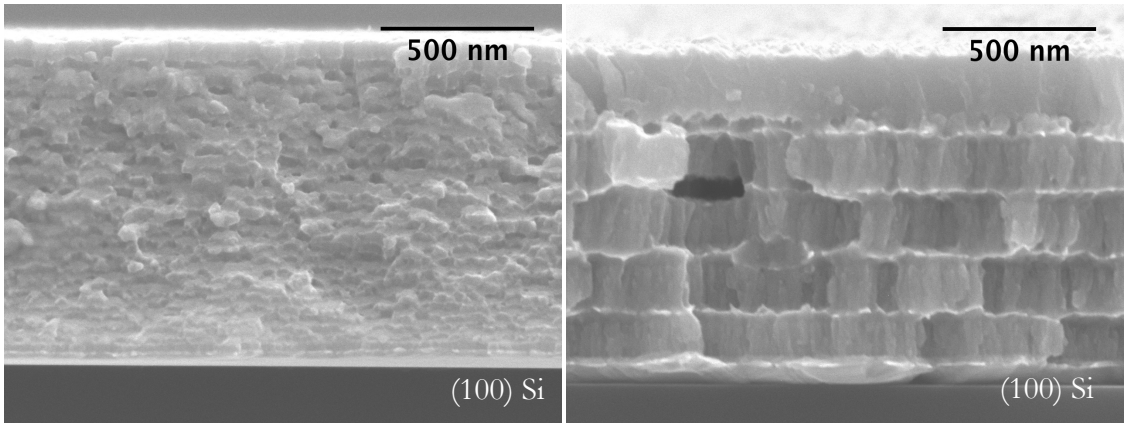

Figure C.1: Cross-Sections of aged Cu/Nb multilayers: 20 nm (left) and 100 nm (right) layer thicknesses, aged in ambient air. These systems used Cu as the base layer and Nb as the capping. Images include silicon substrate.

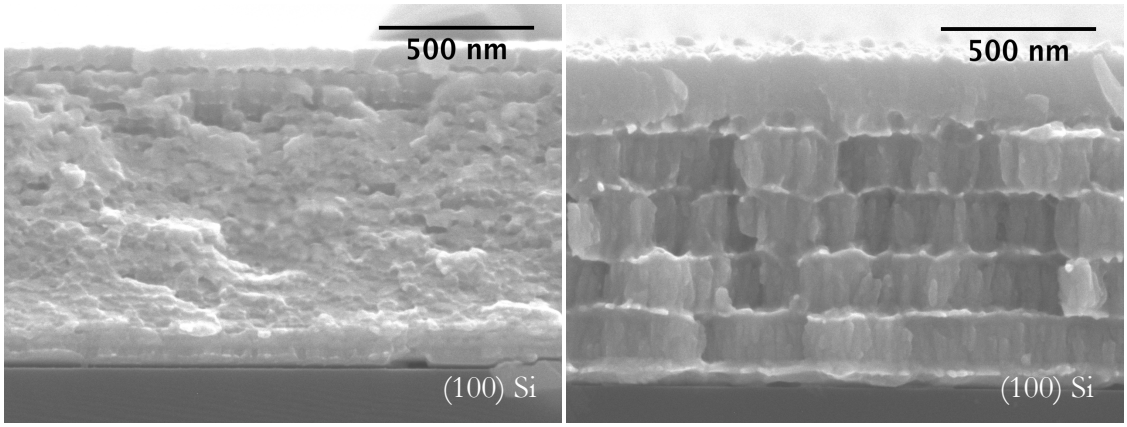

Figure C.3: Cross-Sections of aged Cu/Nb multilayers: 20 nm (left) and 100 nm (right) layer thicknesses, aged in Ar/O. These systems used Cu as the base layer and Nb as the capping. Images include silicon substrate.

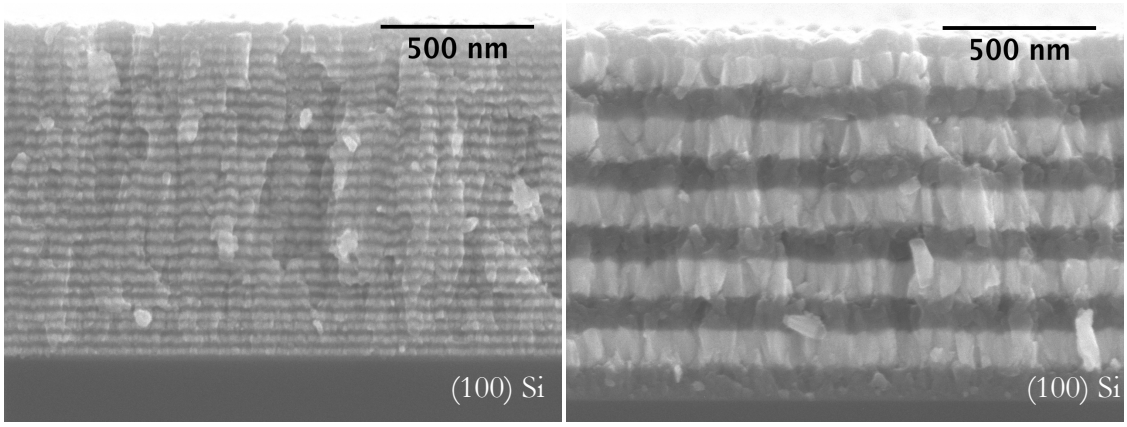

Figure C.2: Cross-Sections of aged Ti/W multilayers: 20 nm (left) and 100 nm (right) layer thicknesses, aged in ambient air. These systems used Ti as the base layer and W as the capping. Images include silicon substrate.

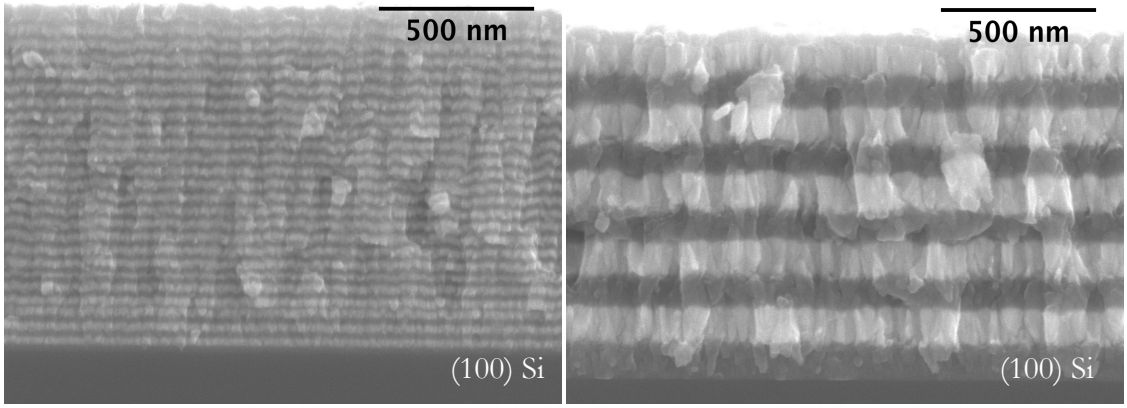

Figure C.4: Cross-Sections of aged Ti/W multilayers: 20 nm (left) and 100 nm (right) layer thicknesses, aged in Ar/O. These systems used Ti as the base layer and W as the capping. Images include silicon substrate.

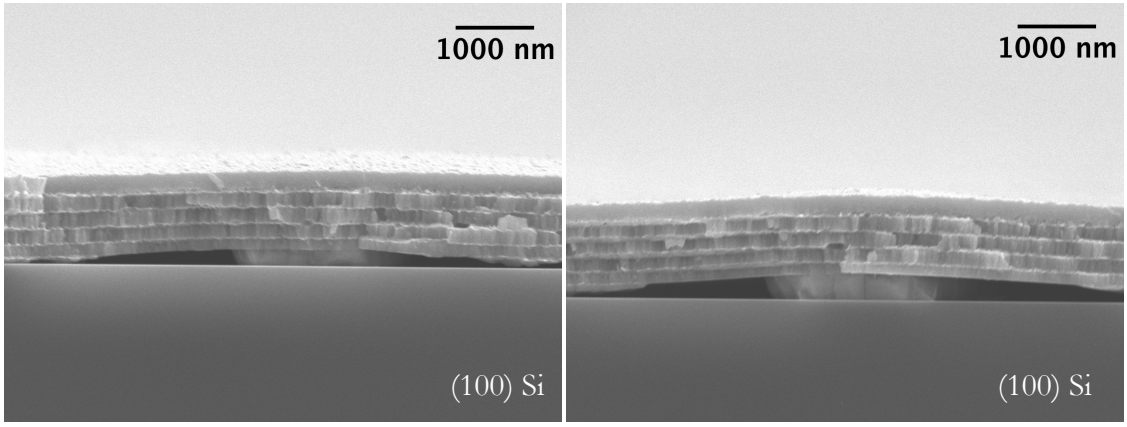

Figure C.5: Cross-Sections of aged Cu/Nb multilayers aged in ambient air, showing two different regions of the film where a defect can be seen at the interface between the silicon substrate and the film. These systems used Cu as the base layer and Nb as the capping. Images include silicon substrate.

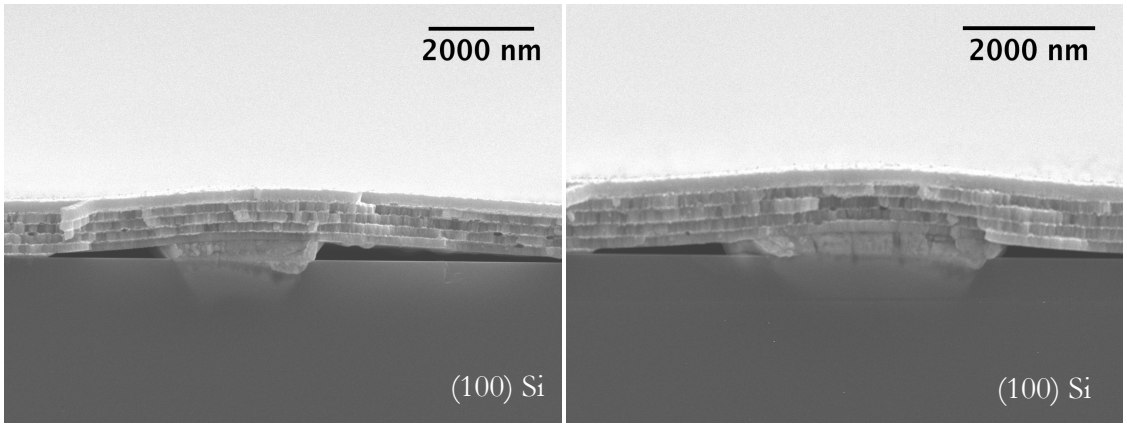

Figure C.6: Cross-Sections of aged Cu/Nb multilayers aged in Ar/O, showing two different regions of the film where a defect can be seen at the interface between the silicon substrate and the film. These systems used Cu as the base layer and Nb as the capping. Images include silicon substrate.

C.3. Notes on Additional Observations

In Figures C.5 and C.6 it can be seen that there are regions of the film that have been pushed vertically by the presence of a defect at the film-substrate interface. Based on the appearance of the regions in Figure C.6 it is the opinion of the author that this observation is the formation of a silicide, most likely copper silicide (Cu_5Si). It has been reported elsewhere that in Cu/Nb systems on Si formed Cu_3Si and other silicides after heating, which was confirmed using XRD, AES, and Rutherford backscatter spectroscopy (RBS)[C.1]. In this study however, no additional analysis has been performed to objectively identify these regions. These defects did not cause a significant change in the hardness measured by nanoindentation. This observation was only noted in the 100nm layer thickness Cu/Nb system when heated in either ambient air or the argon/oxygen blend.

APPENDIX D

ADDITIONAL OPTICAL MICROSCOPE IMAGES OF POLYIMIDE NANOCOMPOSITES

D.1. Introduction

The optical images presented in Chapter Four were limited to those showing representative results for the polyimide nanocomposites. As a consequence some were omitted in the body of this thesis that present similar views to those included. These images were obtained in accordance to the methods described in Section 4.2.5.

D.2. Additional Images

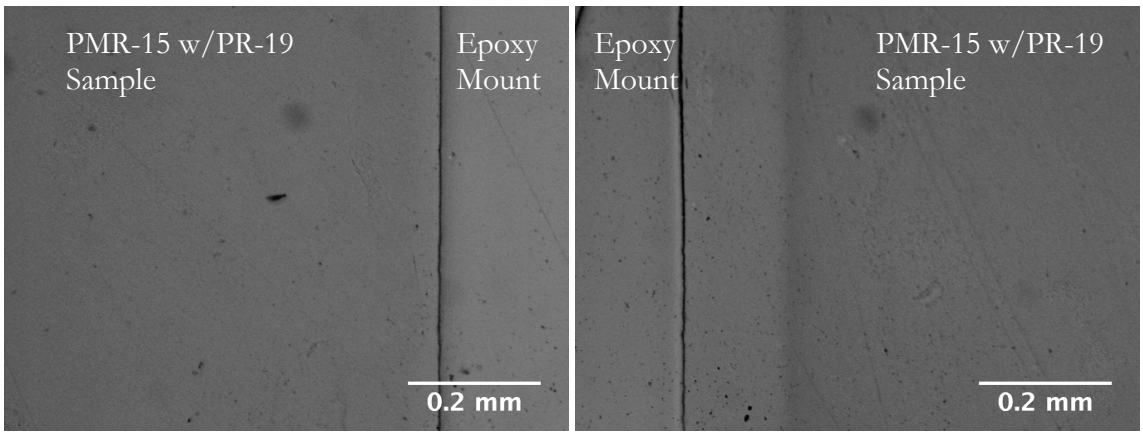

Figure D.1: Optical images of the polished surfaces of unaged (Left) and aged (Right) PMR-15 with PR-19 carbon nanofibers. The edge shown in both images was in contact with the sample mold during processing. Note the change in shade along the edge of the sample the significantly grows during aging.

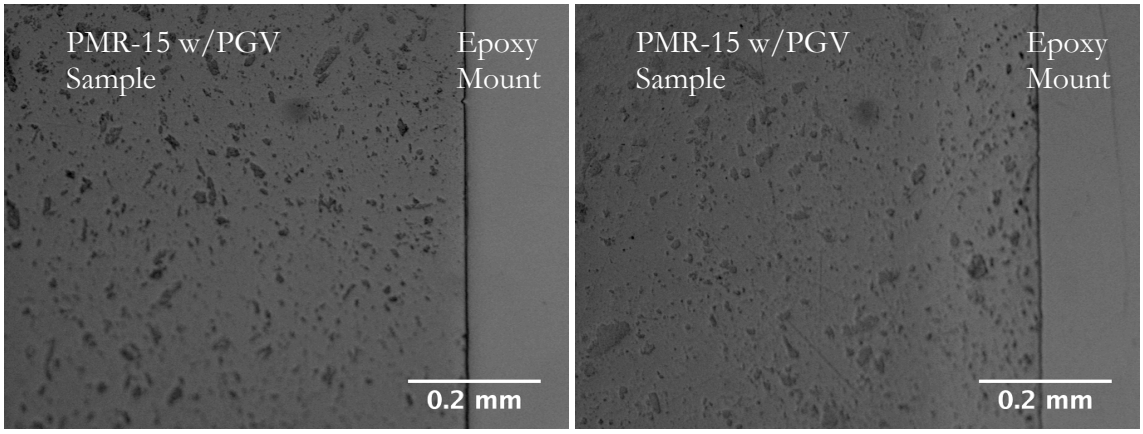

Figure D.2: Optical images of the polished surfaces of unaged (Left) and aged (Right) PMR-15 with PGV clay nanoparticles. The edge shown in both images was in contact with the sample mold during processing. Note the change in shade along the edge of the sample the significantly grows during aging.

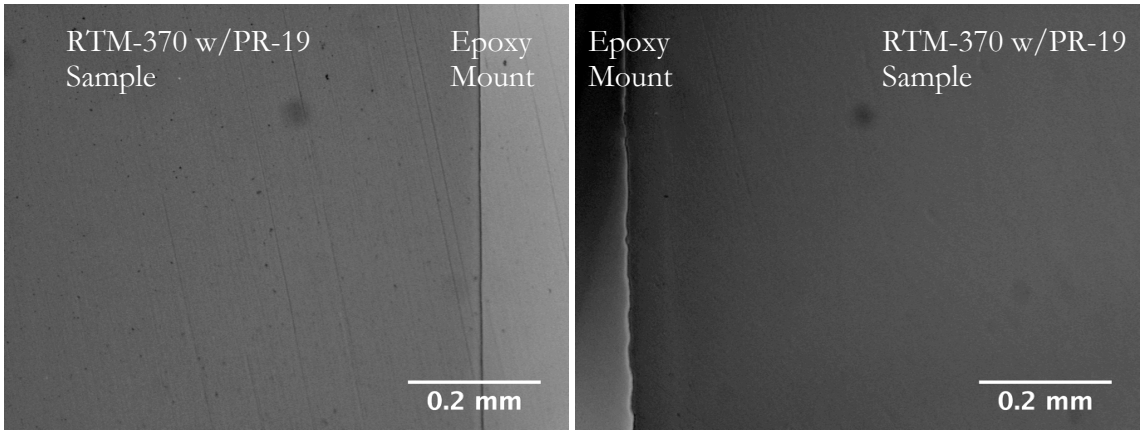

Figure D.3: Optical images of the polished surfaces of unaged (Left) and aged (Right) RTM-370 with PR-19 carbon nanofibers. The edge shown in both images was in contact with the sample mold during processing. Note the appearance of a change in shade along the edge of the sample after aging.

REFERENCES

CHAPTER ONE

1.1 Misra, A. in *Nanostructure Control of Materials* (ed R. H. J. Hannick, Hill, A. J.) Ch. 7, 146-176 (Woodhead Publishing, 2006).

1.2 Miller, S. G. & Meador, M. A. in *48th AIAA/ASME/ASCE/AHS/ASC Structures, Structural Dynamics, and Materials Conference, April 23, 2007 - April 26, 2007*. 7530-7538 (American Institute of Aeronautics and Astronautics Inc.).

1.3 Miller, S. G. *Effects of Nanoparticle and Matrix Interface on Nanocomposite Properties* PhD thesis, University of Akron, (2008).

1.4 Miller, S. G. in *39th International SAMPE Technical Conference - From Art to Science: Advancing Materials and Process Engineering, October 29, 2007 - November 1, 2007*. Midwest Chapter of SAMPE (Soc. for the Advancement of Material and Process Engineering).

1.5 ASTM Standard D883, 2011 "Standard Terminology Relating to Plastics" ASTM International, West Conshohocken, PA, 2003.

1.6 Zhao, S., Schadler, L. S., Hillborg, H. & Auletta, T. Improvements and mechanisms of fracture and fatigue properties of well-dispersed alumina/epoxy nanocomposites. *Composites Science and Technology* **68**, 2976-2982 (2008).

1.7 Zhao, S., Schadler, L. S., Duncan, R., Hillborg, H. & Auletta, T. Mechanisms leading to improved mechanical performance in nanoscale alumina filled epoxy. *Composites Science and Technology* **68**, 2965-2975 (2008).

1.8 Misra, A. & Hoagland, R. G. Effects of elevated temperature annealing on the structure and hardness of copper/niobium nanolayered films. *Journal of Materials Research* **20**, 2046-2054 (2005).

1.9 Misra, A., Hirth, J. P., Kung, H., Hoagland, R. G. & Embury, J. D. in *Structure and Mechanical Properties of Nanophase Materials - Theory and Computer Simulation vs. Experiment. Symposium, 28-30 Nov. 2000.* 4-2 (Mater. Res. Soc).

1.10 Misra, A., Hirth, J. P. & Hoagland, R. G. Length-scale-dependent deformation mechanisms in incoherent metallic multilayered composites. *Acta Materialia* **53**, 4817-4824 (2005).

1.11 Misra, A., Kung, H. & Embury, J. D. Preface to the viewpoint set on: deformation and stability of nanoscale metallic multilayers. *Scripta Materialia* **50**, 707-710 (2004).

1.12 Bellou, A., Scudiero, L. & Bahr, D. F. Thermal stability and strength of Mo/Pt multilayered films. *Journal of Materials Science* **45**, 354-362 (2010).

1.13 Lewis, A. C., Josell, D. & Weihs, T. P. Stability in thin film multilayers and microlaminates: The role of free energy, structure, and orientation at interfaces and grain boundaries. *Scripta Materialia* **48**, 1079-1085 (2003).

1.14 Josell, D., Carter, W. C. & Bonevich, J. E. Stability of multilayer structures: Capillary effects. *Nanostructured Materials* **12**, 387-390 (1999).

1.15 Josell, D. & Spaepen, F. Surfaces, interfaces, and changing shapes in multilayered films. *MRS Bulletin* **24**, 39-43 (1999).

1.16 Guo, Z. *et al.* Flexible high-loading particle-reinforced polyurethane magnetic nanocomposite fabrication through particle-surface-initiated polymerization. *Nanotechnology* **18**, 335704 (2007).

1.17 Guo, Z. *et al.* Strengthening and thermal stabilization of polyurethane nanocomposites with silicon carbide nanoparticles by a surface-initiated-polymerization approach. *Composites Science and Technology* **68**, 164-170 (2008).

1.18 Fu, S.-Y., Feng, X.-Q., Lauke, B. & Mai, Y.-W. Effects of particle size, particle/matrix interface adhesion and particle loading on mechanical properties of particulate-polymer composites. *Composites Part B: Engineering* **39**, 933-961 (2008).

1.19 Wetzel, B., Rosso, P., Haupert, F. & Friedrich, K. Epoxy nanocomposites - fracture and toughening mechanisms. *Engineering Fracture Mechanics* **73**, 2375-2398 (2006).

1.20 Wetzel, B., Haupert, F. & Qiu Zhang, M. Epoxy nanocomposites with high mechanical and tribological performance. *Composites Science and Technology* **63**, 2055-2067 (2003).

1.21 Ciprari, D., Jacob, K. & Tannenbaum, R. Characterization of Polymer Nanocomposite Interphase and Its Impact on Mechanical Properties. *Macromolecules* **39**, 6565-6573, (2006).

1.22 Johnson, L. L., Eby, R. K. & Meador, M. A. B. Investigation of oxidation profile in PMR-15 polyimide using atomic force microscope (AFM). *Polymer* **44**, 187-197 (2003).

1.23 Chuang, K. C. *et al.* in *SAMPE '07: M and P - From Coast to Coast and Around the World, June 3, 2007 - June 7, 2007*. SAMPE Baltimore/Washington Chapter (Soc. for the Advancement of Material and Process Engineering).

1.24 Castelnau, O., Geandier, G., Renault, P. O., Goudeau, P. & Le Bourhis, E. Characterization and modelling of the elastic properties of nano-structured W/Cu multilayers. *Thin Solid Films* **516**, 320-324 (2007).

1.25 Bellou, A. & Bahr, D. F. Strength and aging behavior of Mo/Pt multilayers. 1-9 (2010).

1.26 Shao, S. & Medyanik, S. N. Dislocation-interface interaction in nanoscale fcc metallic bilayers. *Mechanics Research Communications* **37**, 315-319 (2010).

1.27 Shao, S. & Medyanik, S. N. Interaction of dislocations with incoherent interfaces in nanoscale FCC-BCC metallic bi-layers. *Modelling and Simulation in Materials Science and Engineering* **18**, 055010 (2010).

REFERENCES

CHAPTER TWO

2.1 Callister, W. D. *Materials science and engineering: an introduction*. 7th ed., (John Wiley & Sons, 2007).

2.2 Guo, Z. *et al.* Flexible high-loading particle-reinforced polyurethane magnetic nanocomposite fabrication through particle-surface-initiated polymerization. *Nanotechnology* **18**, 335704 (2007).

2.3 Guo, Z. *et al.* Strengthening and thermal stabilization of polyurethane nanocomposites with silicon carbide nanoparticles by a surface-initiated-polymerization approach. *Composites Science and Technology* **68**, 164-170 (2008).

2.4 Wetzel, B., Rosso, P., Haupert, F. & Friedrich, K. Epoxy nanocomposites - fracture and toughening mechanisms. *Engineering Fracture Mechanics* **73**, 2375-2398 (2006).

2.5 Wetzel, B., Haupert, F. & Qiu Zhang, M. Epoxy nanocomposites with high mechanical and tribological performance. *Composites Science and Technology* **63**, 2055-2067 (2003).

2.6 Oliver, W. C. & Pharr, G. M. An improved technique for determining hardness and elastic modulus using load and displacement sensing indentation experiments. *Journal of Materials Research* **7**, 1564-1583 (1992).

2.7 Fischer-Cripps, A. C. *Nanoindentation / Anthony C. Fischer-Cripps*. (Springer, 2002).

2.8 Saha, R. & Nix, W. D. Effects of the substrate on the determination of thin film mechanical properties by nanoindentation. **50**, 23-38 (2002).

2.9 Han, S. M., Saha, R. & Nix, W. D. Determining hardness of thin films in elastically mismatched film-on-substrate systems using nanoindentation. *Acta Materialia* **54**, 1571-1581 (2006).

2.10 Woodcock, C. L., Bahr, D. F. & Moody, N. R. in *Fundamentals of Nanoindentation and Nanotribology II, November 28, 2000 - November 30, 2000*. Q7.14.11-Q17.14.16 (Materials Research Society).

2.11 Goodhew, P. J. H., J.; Beanland, R. *Electron Microsopy and Analysis*. 3rd edition, (Taylor & Francis, 2001).

2.12 Cullity, B. D. *Elements of X-ray diffraction, 2nd edition*. (Addison-Wesley, 1978).

2.13 Schlotz, R. U., S. *Introduction to X-Ray Fluorescence (XRF)*, <http://www.bruker-axs.de/fileadmin/user_upload/xrfintro/sec1_8.html> (2006).

2.14 Veeco Instruments Inc. *Dektak3 – Surface Profile Measuring System – Operation Manual.* Revision 1.05 (Veeco Inc., 1994).

2.15 Stoney, G. G. The Tension of Metallic Films Deposited by Electrolysis. *Proceedings of the Royal Society of London. Series A, Containing Papers of a Mathematical and Physical Character* **82**, 172-175 (1909).

2.16 Townsend, P. H., Barnett, D. M. & Brunner, T. A. Elastic relationships in layered composite media with approximation for the case of thin films on a thick substrate. *Journal of Applied Physics* **62**, 4438-4444 (1987).

2.17 Labat, S., Bocquet, F., Gilles, B. & Thomas, O. Stresses and interfacial structure in Au-Ni and Ag-Cu metallic multilayers. *Scripta Materialia* **50**, 717-721 (2004).

2.18 Ramaswamy, V., Nix, W. D. & Clemens, B. M. Coherency and surface stress effects in metal multilayers. *Scripta Materialia* **50**, 711-715 (2004).

2.19 Floro, J. A., Chason, E. & Lee, S. R. in *Proceedings of the 1995 MRS Fall Symposium, November 27, 1995 - November 30, 1995.* 491-496 (Materials Research Society).

REFERENCES

CHAPTER THREE

3.1 Misra, A. in *Nanostructure Control of Materials* (ed R. H. J. Hannick, Hill, A. J.) Ch. 7, 146-176 (Woodhead Publishing, 2006).

3.2 Misra, A., Verdier, M., Kung, H., Embury, J. D. & Hirth, J. P. Deformation mechanism maps for polycrystalline metallic multiplayers. *Scripta Materialia* **41**, 973-979 (1999).

3.3 Misra, A., Hirth, J. P. & Hoagland, R. G. Length-scale-dependent deformation mechanisms in incoherent metallic multilayered composites. *Acta Materialia* **53**, 4817-4824 (2005).

3.4 Mara, N., Sergueeva, A., Misra, A. & Mukherjee, A. K. Structure and high-temperature mechanical behavior relationship in nano-scaled multilayered materials. *Scripta Materialia* **50**, 803-806 (2004).

3.5 Verdier, M., Huang, H., Spaepen, F., Embury, J. D. & Kung, H. Microstructure, indentation and work hardening of Cu/Ag multilayers. *Philosophical Magazine* **86**, 5009 - 5016 (2006).

3.6 Verdier, M. Plasticity in fine scale semi-coherent metallic films and multilayers. *Scripta Materialia* **50**, 769-773 (2004).

3.7 Castelnau, O., Geandier, G., Renault, P. O., Goudeau, P. & Le Bourhis, E. Characterization and modelling of the elastic properties of nano-structured W/Cu multilayers. *Thin Solid Films* **516**, 320-324 (2007).

3.8 Goudeau, P., Villain, P., Girardeau, T., Renault, P. O. & Badawi, K. F. Elastic constants investigation by X-ray diffraction of in situ deformed metallic multi-layers. *Scripta Materialia* **50**, 723-727 (2004).

3.9 Girault, B., Villain, P., Le Bourhis, E., Goudeau, P. & Renault, P. O. X-ray diffraction analysis of the structure and residual stresses of W/Cu multilayers. *Surface and Coatings Technology* **201**, 4372-4376 (2006).

3.10 Cammarata, R. C. Dynamic aspects regarding the mechanical behavior of multilayered thin films and their measurements. *Scripta Materialia* **50**, 751-755 (2004).

3.11 Lamm, A. V. & Anderson, P. M. Yield maps for nanoscale metallic multilayers. *Scripta Materialia* **50**, 757-761 (2004).

3.12 Kramer, D. E., Savage, M. F., Lin, A. & Foecke, T. Novel method for TEM characterization of deformation under nanoindents in nanolayered materials. *Scripta Materialia* **50**, 745-749 (2004).

3.13 Was, G. S. & Foecke, T. Deformation and fracture in microlaminates. *Thin Solid Films* **286**, 1-31 (1996).

3.14 Labat, S., Bocquet, F., Gilles, B. & Thomas, O. Stresses and interfacial structure in Au-Ni and Ag-Cu metallic multilayers. *Scripta Materialia* **50**, 717-721 (2004).

3.15 Matweb. *Matweb - Online Materials Information Resource*, <www.matweb.com> (1996-2011).

3.16 Bellou, A., Scudiero, L. & Bahr, D. F. Thermal stability and strength of Mo/Pt multilayered films. *Journal of Materials Science* **45**, 354-362 (2010).

3.17 Misra, A. & Hoagland, R. G. Effects of elevated temperature annealing on the structure and hardness of copper/niobium nanolayered films. *Journal of Materials Research* **20**, 2046-2054 (2005).

3.18 Friedman, L. H. Towards a full analytic treatment of the Hall-Petch behavior in multilayers: putting the pieces together. *Scripta Materialia* **50**, 763-767 (2004).

3.19 Spaepen, F. & Yu, D. Y. W. A comparison of the strength of multilayers, thin films and nanocrystalline compacts. *Scripta Materialia* **50**, 729-732 (2004).

3.20 Misra, A., Kung, H. & Embury, J. D. Preface to the viewpoint set on: deformation and stability of nanoscale metallic multilayers. *Scripta Materialia* **50**, 707-710 (2004).

3.21 Bellou, A. & Bahr, D. F. Strength and aging behavior of Mo/Pt multilayers. 1-9 (2010).

3.22 Misra, A., Hirth, J. P. & Kung, H. Single-dislocation-based strengthening mechanisms in nanoscale metallic multilayers. *Philosophical Magazine A (Physics of Condensed Matter: Structure, Defects and Mechanical Properties)* **82**, 2935-2951 (2002).

3.23 Rao, S. I. & Hazzledine, P. M. Atomistic simulations of dislocation-interface interactions in the Cu-Ni multilayer system. *Philosophical Magazine A* **80**, 2011-2040 (2000).

3.24 Misra, A., Hirth, J. P., Kung, H., Hoagland, R. G. & Embury, J. D. in *Structure and Mechanical Properties of Nanophase Materials - Theory and Computer Simulation vs. Experiment. Symposium, 28-30 Nov. 2000.* 4-2 (Mater. Res. Soc).

3.25 Mitlin, D. *et al.* Formation of misfit dislocations in nanoscale Ni-Cu bilayer films. *Philosophical Magazine* **84**, 719-736 (2004).

3.26 Hoagland, R. G., Mitchell, T. E., Hirth, J. P. & Kung, H. On the strengthening effects of interfaces in multilayer fcc metallic composites. *Philosophical Magazine A (Physics of Condensed Matter: Structure, Defects and Mechanical Properties)* **82**, 643-664 (2002).

3.27 Shao, S. & Medyanik, S. N. Dislocation-interface interaction in nanoscale fcc metallic bilayers. *Mechanics Research Communications* **37**, 315-319 (2010).

3.28 Hoagland, R. G., Kurtz, R. J. & Henager, C. H. Slip resistance of interfaces and the strength of metallic multilayer composites. *Scripta Materialia* **50**, 775-779 (2004).

3.29 Shao, S. & Medyanik, S. N. Interaction of dislocations with incoherent interfaces in nanoscale FCC-BCC metallic bi-layers. *Modelling and Simulation in Materials Science and Engineering* **18**, 055010 (2010).

3.30 Schmidt, T. K., Balk, T. J., Dehm, G. & Arzt, E. Influence of tantalum and silver interlayers on thermal stress evolution in copper thin films on silicon substrates. *Scripta Materialia* **50**, 733-737 (2004).

3.31 Thornton, J. A. Influence of apparatus geometry and deposition conditions on the structure and topography of thick sputtered coatings. *Journal of Vacuum Science and Technology* **11**, 666-670 (1974).

3.32 Kennedy, M., Moody, N. & Bahr, D. The aging of metallic thin films: Delamination, strain relaxation, and diffusion. *JOM Journal of the Minerals, Metals and Materials Society* **59**, 50-53, (2007).

3.33 Petasch, W., Kegel, B., Schmid, H., Lendenmann, K. & Keller, H. U. Low-pressure plasma cleaning: a process for precision cleaning applications. *Surface and Coatings Technology* **97**, 176-181 (1997).

3.34 Saha, R. & Nix, W. D. Effects of the substrate on the determination of thin film mechanical properties by nanoindentation. **50**, 23-38 (2002).

3.35 Maille, L., Sant, C., Aubert, P. & Garnier, P. in *Mechanical Properties Derived from Nanostructuring Materials. Symposium, 22-25 April 2003.* 239-244 (Mater. Res. Soc).

3.36 Stoney, G. G. The Tension of Metallic Films Deposited by Electrolysis. *Proceedings of the Royal Society of London. Series A, Containing Papers of a Mathematical and Physical Character* **82**, 172-175 (1909).

3.37 Vinci, R. P., Zielinski, E. M. & Bravman, J. C. Thermal strain and stress in copper thin films. *Thin Solid Films* **262**, 142-153 (1995).

3.38 Monig, R., Keller, R. R. & Volkert, C. A. Thermal fatigue testing of thin metal films. *Review of Scientific Instruments*. Vol. 75 (AIP, 2004).

REFERENCES

CHAPTER FOUR

4.1 Zhao, S., Schadler, L. S., Hillborg, H. & Auletta, T. Improvements and mechanisms of fracture and fatigue properties of well-dispersed alumina/epoxy nanocomposites. *Composites Science and Technology* **68**, 2976-2982 (2008).

4.2 Zhao, S., Schadler, L. S., Duncan, R., Hillborg, H. & Auletta, T. Mechanisms leading to improved mechanical performance in nanoscale alumina filled epoxy. *Composites Science and Technology* **68**, 2965-2975 (2008).

4.3 Miller, S. G. *Effects of Nanoparticle and Matrix Interface on Nanocomposite Properties* PhD thesis, University of Akron, (2008).

4.4 Miller, S. G. in *39th International SAMPE Technical Conference - From Art to Science: Advancing Materials and Process Engineering, October 29, 2007 - November 1, 2007*. Midwest Chapter of SAMPE (Soc. for the Advancement of Material and Process Engineering).

4.5 Miller, S. G. & Meador, M. A. in *48th AIAA/ASME/ASCE/AHS/ASC Structures, Structural Dynamics, and Materials Conference, April 23, 2007 - April 26, 2007*. 7530-7538 (American Institute of Aeronautics and Astronautics Inc.).

4.6 Guo, Z. *et al.* Flexible high-loading particle-reinforced polyurethane magnetic nanocomposite fabrication through particle-surface-initiated polymerization. *Nanotechnology* **18**, 335704 (2007).

4.7 Guo, Z. *et al.* Strengthening and thermal stabilization of polyurethane nanocomposites with silicon carbide nanoparticles by a surface-initiated-polymerization approach. *Composites Science and Technology* **68**, 164-170 (2008).

4.8 Fu, S.-Y., Feng, X.-Q., Lauke, B. & Mai, Y.-W. Effects of particle size, particle/matrix interface adhesion and particle loading on mechanical properties of particulate-polymer composites. *Composites Part B: Engineering* **39**, 933-961 (2008).

4.9 Wetzel, B., Rosso, P., Haupert, F. & Friedrich, K. Epoxy nanocomposites - fracture and toughening mechanisms. *Engineering Fracture Mechanics* **73**, 2375-2398 (2006).

4.10 Wetzel, B., Haupert, F. & Qiu Zhang, M. Epoxy nanocomposites with high mechanical and tribological performance. *Composites Science and Technology* **63**, 2055-2067 (2003).

4.11 Ciprari, D., Jacob, K. & Tannenbaum, R. Characterization of Polymer Nanocomposite Interphase and Its Impact on Mechanical Properties. *Macromolecules* **39**, 6565-6573, (2006).

4.12 Callister, W. D. *Materials science and engineering: an introduction*. 7th ed., (John Wiley & Sons, 2007).

4.13 Ounaies, Z., Park, C., Harrison, J. & Lillehei, P. Evidence of Piezoelectricity in SWNT-Polyimide and SWNT-PZT-Polyimide Composites. *Journal of Thermoplastic Composite Materials* **21**, 393-409, (2008).

4.14 Damm, C., Münstedt, H. & Rösch, A. Long-term antimicrobial polyamide 6/silver-nanocomposites. *Journal of Materials Science* **42**, 6067-6073 (2007).

4.15 Dasari, A., Yu, Z.-Z. & Mai, Y.-W. Fundamental aspects and recent progress on wear/scratch damage in polymer nanocomposites. *Materials Science and Engineering: R: Reports* **63**, 31-80 (2009).

4.16 Jee, A.-Y. & Lee, M. Comparative analysis on the nanoindentation of polymers using atomic force microscopy. *Polymer Testing* **29**, 95-99 (2010).

4.17 Johnson, L. L., Eby, R. K. & Meador, M. A. B. Investigation of oxidation profile in PMR-15 polyimide using atomic force microscope (AFM). *Polymer* **44**, 187-197 (2003).

4.18 Chuang, K. C. *et al.* in *SAMPE '07: M and P - From Coast to Coast and Around the World, June 3, 2007 - June 7, 2007*. SAMPE Baltimore/Washington Chapter (Soc. for the Advancement of Material and Process Engineering).

4.19 Pinnavaia, T. J., 2011. *Discussion on SAP-90 structure and synthesis.* [phone conversation] (Personal communication, 20 July 2011).

4.20 Pyrograf Products, Inc. *Pyrograf-III PR-19 HHT Carbon Nanofibers*, <www.pyrografproducts.com> (1996-2011).

REFERENCES

CHAPTER FIVE

5.1 Misra, A. & Hoagland, R. G. Effects of elevated temperature annealing on the structure and hardness of copper/niobium nanolayered films. *Journal of Materials Research* **20**, 2046-2054 (2005).

5.2 Vinci, R. P., Zielinski, E. M. & Bravman, J. C. Thermal strain and stress in copper thin films. *Thin Solid Films* **262**, 142-153 (1995).

5.3 Castelnau, O., Geandier, G., Renault, P. O., Goudeau, P. & Le Bourhis, E. Characterization and modelling of the elastic properties of nano-structured W/Cu multilayers. *Thin Solid Films* **516**, 320-324 (2007).

5.4 Goudeau, P., Villain, P., Girardeau, T., Renault, P. O. & Badawi, K. F. Elastic constants investigation by X-ray diffraction of in situ deformed metallic multi-layers. *Scripta Materialia* **50**, 723-727 (2004).

5.5 Girault, B., Villain, P., Le Bourhis, E., Goudeau, P. & Renault, P. O. X-ray diffraction analysis of the structure and residual stresses of W/Cu multilayers. *Surface and Coatings Technology* **201**, 4372-4376 (2006).

5.6 Misra, A., Hirth, J. P. & Hoagland, R. G. Length-scale-dependent deformation mechanisms in incoherent metallic multilayered composites. *Acta Materialia* **53**, 4817-4824 (2005).

5.7 Thornton, J. A. Influence of apparatus geometry and deposition conditions on the structure and topography of thick sputtered coatings. *Journal of Vacuum Science and Technology* **11**, 666-670 (1974).

REFERENCES

APPENDIX B

B. 1 Oyen, M. L. Sensitivity of polymer nanoindentation creep measurements to experimental variables. *Acta Materialia* **55**, 3633-3639 (2007).

B.2 Cordill, M. J., Moody, N. R. & Gerberich, W. W. Effects of dynamic indentation on the mechanical response of materials. *Journal of Materials Research* **23**, 1604-1613 (2008).

B.3 Hysitron Inc. *Triboscope – Operation Manual*. Software Version 8.1 (Hysitron Inc., 2007).

REFERENCES

APPENDIX C

C. 1 Mattoso Filho, N., Achete, C. & Freire Jr, F. L. Silicide formation and phase separation from Cu/Nb and Nb/Cu bilayers on silicon. *Thin Solid Films* **220**, 184-190 (1992).